Preparation, Characterization and Modification of Oil loaded Protein Microcapsules and Composite Protein-Mineral Microcapsules

Ulrike Doering

Dissertation
zur Erlangung des akademischen Grades
„doctor rerum naturalium“
(Dr. rer. nat.)
in der Wissenschaftsdisziplin „Kolloidchemie“

eingereicht an der
Mathematisch-Naturwissenschaftlichen Fakultät
Institut für Chemie
der Universität Potsdam

Potsdam, März 2022

Ort und Tag der Disputation: Universität Potsdam am 15.08.2022

Unless otherwise indicated, this work is licensed under a Creative Commons License
Attribution 4.0 International.
This does not apply to quoted content and works based on other permissions.
To view a copy of this licence visit:
https://creativecommons.org/licenses/by/4.0

Hauptbetreuer/in: Prof. Dr. Alexander Böker
2. Gutachter/in: Prof. Dr. Ilko Bald
3. Gutachter/in: Prof. Dr. Michael Gradzielski

Published online on the
Publication Server of the University of Potsdam:
https://doi.org/10.25932/publishup-55958
https://nbn-resolving.org/urn:nbn:de:kobv:517-opus4-559589

Diese Forschungsarbeit wurde in der Zeit von Januar 2018 bis August 2021 an der Universität Potsdam und dem Fraunhofer Institut für Angewandte Polymerforschung IAP in Potsdam durchgeführt. Die Betreuung erfolgte durch Prof. Dr. Alexander Böker.

Amtierender Dekan: Prof. habil. Helmut Elsenbeer, PhD

“All truths are easy to understand once they are discovered;

the point is to discover them.”

Galileo Galilei

Danksagung

Ohne die Unterstützung vieler Menschen wäre diese Arbeit nicht möglich gewesen. Deshalb möchte ich mich hiermit bei diesen Menschen bedanken.

Bei Prof. Dr. Alexander Böker bedanke ich mich für die Möglichkeit, meine Doktorarbeit in seiner Arbeitsgruppe zu schreiben und die produktiven Diskussionen.

Natürlich möchte ich mich auch bei den weiteren Gutachtern dieser Arbeit bedanken, Prof. Ilko Bald und Prof. Michael Gradzielski.

Mein besonderer Dank gilt Dr. Dmitry Grigoriev für die Idee zu diesem interessanten und herausfordernden Thema und seine stetige Unterstützung bei den verschiedensten Problemstellungen und Fragen. Darüber hinaus bedanke ich mich für die umfassenden Diskussionen und Anregungen und seinen Ideenreichtum. Ohne seinen Einsatz wäre diese Arbeit nicht zu dem geworden, was sie ist.

Des Weiteren möchte ich mich bei allen Mitgliedern unserer Arbeitsgruppe für die tolle Arbeitsatmosphäre bedanken. Ich danke Dr. Oksana Travkova, die die Organisation unserer kleinen Uni-Gruppe übernommen hat und mir dadurch immer eine große Hilfe war. Ein besonderer Dank geht an meine Büro-Kollegen Marc Zimmermann, Maria Mathieu und vor allem Falko Rottke, die mir mit Rat und Tat zur Seite standen. Außerdem bedanke ich mich bei Dr. Ruben Rosencrantz für sein kritisches Hinterfragen und die wissenschaftlichen Diskussionen und Dr. Ulrich Glebe, für sein offenes Ohr für Fragen und die MALDI-Messungen, die er für mich gemacht hat. Dr. Sophia Rosencrantz danke ich für ihre tatkräftige Unterstützung bei der Durchführung der SDS-PAGE Versuche.

Bei Matthes Förster und Mario Hoffmann bedanke ich mich dafür, dass sie immer meine Probleme im IT-Bereich lösen konnten. Weiterhin danke ich Jadwiga Galties für die Erstellung der schönen Grafiken. Ein weiteres Dankeschön geht an Kathrin Geßner, die meine Proben mit Hilfe von TGA untersucht hat.

Für die tollen REM meiner Mikrokapseln bedanke ich mich bei Dr. Brigitte Tiersch und Sibylle Rüstig und bei Heike Runge bedanke ich mich zusätzlich für die EDX Messungen. Enrico Ribacki danke ich für das Analysieren meiner Hydroxylapatit- Nanopartikel mit XRD.

Außerdem möchte ich Dr. Kosti Tapio für die vielen Raman Messungen und die anschließende Diskussion der Ergebnisse zusammen mit Prof. Dr. Ilko Bald danken. Zusätzlich danke ich ihnen für ihre Unterstützung beim Schreiben von Manuskripten.

Ein großer Dank geht auch an Tino Riske, der die SFM Kompressionsmessungen der Mikrokapseln für mich durchgeführt und dabei sehr viel Geduld und Engagement gezeigt hat bei dieser nicht ganz einfachen Aufgabe.

Zu guter Letzt möchte ich meinen Eltern danken, die mich immer in jeder Lebenslage unterstützt haben.

Contents

List of Abbreviations

µg Microgram (1 x 10^{-6} g)
µl Microliter (1 x 10^{-6} l)
µm Micrometer (1 x 10^{-6} m)
3D three-dimensional
A Interface
Å Ångström
APTES (3-Aminoproply)triethoxysilane
atm Atmosphere
BisTris Bis(2-hydroxyethyl)amino-tris(hydroxymethyl)methan
BSA Bovine Serum Albumin
c Concentration; Velocity of the sound
D Diffusion coefficient
DCDMS Dichlorodimethylsilane
DLS Dynamic light scattering
DMSO Dimethylsulfoxid
DTT Dithiothreitol
E Young's modulus
EDX Energy dispersive x-ray spectroscopy
e.g. exempli gratia (lat.) – for example
et al. et alii (lat.) – and others
f Frequency
F Force
FITC Fluorescein isothiocyanate
FTIR Fourier-transform infrared spectroscopy
G Gibbs energy
GA Glutaraldehyde
h Shell thickness
HAP Hydroxyapatite
I Intensity
IEP Isoelectric point
IFT Interfacial tension
k Kinetic constanst of reorientation
K Polytropic index of the gas mixture
K Kelvin
kDa Kilodalton (1 x 10^3 Dalton)
kHz Kilohertz (1 x 10^3 Hz)
mg Milligram (1 x 10^{-3} g)
mL Milliliter (1 x 10^{-3} l)
mM Millimolar (1 x 10^{-3} M)
mN Millinewton (1 x 10^{-3} N)
MPa Megapascal (1 x 10^6 Pa)

mV Millivolt (1 x 10^{-3} V)
M_W Molecular weight
NP Nanoparticle
nm Nanometer
p Pressure
P_a Acoustic pressure
P_A Maximum pressure amplitude
P_h Hydrostatic pressure
pH Negative common logarithm of the hydrogen ion activity
Q Ratio of the resonance amplitude to the static amplitude of vibration of the bubble
R Radius of microcapsule
RITC Rhodamine B isothiocyanate
rpm Revolutions per minute
s Second
s Slope f the initial linear part of the force deformation-curve
SDS-PAGE Sodium dodecyl sulphate – polyacrylamide gel electrophoresis
SEM Scanning electron microscope
SFM Scanning force microscope
Si71 Silica particles partially modified with DCDMS
T Temperature
TGA Thermogravimetric analysis
W Watt
W Work
wt% Weight percentage
XRD X-ray diffraction
ZP Zeta potential
γ Interfacial tension
γ_0 Surface tension of the solvent
γ_{eq} Interfacial tension in equilibrium
γ_{ow} Interfacial tension at oil-water interface
γ_{so} Interfacial tension at solid-oil interface
γ_{sw} Interfacial tension at solid-water interface
Γ Surface excess
δ Indentation
θ Three phase contact angle
μ_J Potential of adsorbing substances
ν Poisson ratio
ρ Density
σ Interface per area
τ Relaxation time

List of Figures

List of Tables

1. Introduction

Over the course of the last two decades, several methods for the synthesis of microcapsules with shells of various materials were presented. The capsules have been prepared from self-assembled biomolecules[1, 2] through layer-layer (lbl)-assembly,[3-5] or by using an emulsion drop as template.[6-8] These drops can be stabilized by proteins[9] or nanoparticles (NPs) forming so-called Pickering emulsions.[8, 10, 11] An emulsion has the advantages of a one-pot synthesis and of the possibility to control the size of the droplets and therefore of the resulting capsules. Those capsules are used for the encapsulation of various compounds, such as nutrients,[12] fragrances,[13] pharmaceuticals[14] and catalysts.[15]

The choice of the wall material is an important aspect of the capsules. Inorganic materials can endure higher temperatures and exhibit higher rigidity. The novel physical features created by the formation of a densely packed spherical shell from colloidal building blocks have attracted increasing interest. Most commonly used materials in the scientific fields of biomedicine are calcium carbonate,[16] calcium phosphate[6, 8] and silica.[7, 10] The choice of colloids can control the physical characteristics of the microcapsules, including biocompatibility, permeability and mechanical strength. Then again, biopolymers as wall material have the benefit that their properties can be adjusted with the possibility to make them stimuli-responsive enabling a controlled release of loaded substances.[1, 17, 18] Further benefits are their biodegradability, natural abundance and low costs.

Proteins have also been thoroughly examined as biological building blocks for capsule shells. They offer various advantages with their structural and chemical versatility, amphiphilic character and emulsifying properties.[19] Suslick and Grinstaff developed a technique for the synthesis of protein microcapsules using ultrasound.[20] Gedanken and coworkers demonstrated the effectiveness of the sonochemical method for the synthesis of protein microcapsules, which does not utilize any toxic ingredients and is fast and economical.[21, 22] It is widely accepted that the capsule formation is a result of two very fast subsequently occurring phenomena: protein adsorption and shell cross-linking.[20, 23-25] First, the ultrasonic treatment of a two-phase liquid system takes place resulting in an oil-in-water (O/W) emulsion stabilized by protein molecules adsorbed at the interface of the emulsion droplets. Additionally, the propagation of the ultrasound wave through a liquid medium produces acoustic cavitations, i.e. the formation, growth and collapse of bubbles. The collapse is a very fast adiabatic process and yields highly

reactive radicals[23, 26, 27] like superoxide. Suslick et al. proposed that the superoxide radicals cause the reaction between thiol groups in cysteines, which are present in various proteins (e.g. in BSA) and that the protein capsule shells are held together by cross-linking through interprotein disulfide linkages arising from this oxidation of cysteine. With this technique microcapsules with various proteins and controllable sizes can be synthesized.[25, 28-31] However, the BSA structure possesses only one thiol group enabling solely the formation of dimers but not a cross-linked network. Moreover, Gedanken et al. demonstrated in addition to the findings of Suslick et al. the possibility of ultrasonically driven formation of microcapsules made of streptavidin, which does not contain any cysteine.[32] The authors hypothesize that hydrophobic interactions or thermal denaturation of the protein after the initial ultrasonic emulsification support the microcapsule formation. Further development of these ideas continued more recently in the works of Cavaco-Paulo and collaborators,[33, 34] where the cysteine-free mechanism of ultrasonically driven protein capsule formation was clearly demonstrated. At the same time, these publications do not contain any evidences refuting unambiguously the mechanism suggesting the formation of intermolecular disulfide bridges upon high-intensity ultrasound treatment, proposed earlier by Suslick et al.[20, 23, 35, 36] Until now there are no scientific studies, which either present an unequivocal substantiation or demonstrate a clear rebuttal of this mechanism. In particular chemical processes behind it remain elusive. In the first part of this work, several experimental proofs will be presented pointing towards the formation of intermolecular S–S bonds in the capsule shell and corresponding structural changes of the protein during this process.

The combination of inorganic nanoparticles and proteins will enable the synthesis of new hybrid materials.[6, 37, 38] In the second part of this work, a fast and economic method for the formation of composite protein-mineral microcapsules in an one-pot-process will be presented. Using high-intensity ultrasound protein- and nanoparticle-stabilized microcapsules loaded with different oils were prepared. Silica, calcium carbonate and hydroxyapatite (HAP) nanoparticles were used for the formation of the composite microcapsules.

The surface of the shell is responsible for the dispersability of the capsules, their responses to environmental changes and their adhesion to surfaces. To meet the requirements of different applications it is desirable to be able to modify the surface chemistry. The capsule shell composed of BSA and nanoparticles provides two sites for modification. It was shown that the shell of the composite microcapsules can be easily modified by different materials including dyes (such as rhodamine B isothiocyanate (RITC) and fluorescein isothiocyanate (FITC)) and

the alkoxysilane 3-aminopropyltriethoxysilane (APTES). Through its terminal amines, the coupling agent APTES allows further chemical/ biochemical modifications.

The mechanical characteristics of the shell are very important for many applications as well since they determine the integrity, sensitivity and stability of the microcapsules. Therefore, the mechanical properties of both types of capsules were compared by nanocompression measurements in aqueous conditions. The measurements were performed using a scanning force microscope (SFM) and the Young's moduli were obtained from the measured force-deformation curves within the small-deformation regime.

2. Theoretical Background

The theoretical background of this thesis will be introduced within this chapter. Only theoretical aspects important for this work will be explained, since it is beyond the scope of this thesis to give a complete overview over each topic. In the given literature, deeper information can be found.

2.1. Interfacial Tension, Proteins as Surfactants and their influence on the emulsion stability

A molecule has the same attractive interactions into all directions inside a phase, meaning that it feels no force in any direction. This is different for molecules in a two phase system. At the interface, the molecule has attractive interactions with the molecules of its own phase and the interactions with the molecules of the other phase are less attractive or even repulsive. Therefore, the molecule feels a force into its own phase, which gives rise to the phenomenon of interfacial tension (IFT).[39-41]

Molecules at the interface have a higher energy level than molecules in the interior of the phase and this additional energy is called interfacial energy. Work or energy is needed to overcome this energy difference or to increase the interface. The interface between oil and aqueous phase should be increased in the creation of an oil-in-water (O/W) emulsion. Emulsions are dispersions, which consist of two immiscible liquid phases: an outer continuous phase and an inner dispersed phase. In our everyday life, emulsions are omnipresent including foods (such as mayonnaise and milk), paints and coatings or personal care products (e.g. body lotion). There are different types of emulsions: oil-in-water (O/W), water-in-oil (W/O) as well as double emulsions, namely water-in-oil-in-water (W/O/W) and oil-in-water-in-oil (O/W/O). Because of an increase of the interface, the preparation of an emulsion requires energy. By stirring, shaking, mixing, vortexing or ultrasonication the required energy can be mechanically introduced into the system. However, emulsions tend to phase separation since they are thermodynamically unstable. The system favors minimal surface at maximal volume and therefore two droplets will coalesce, if they hit each other. This process is called Ostwald ripening. The characteristics of emulsions are dependent on emulsification technique and on the stabilization of the interface.[41-43]

To increase the interface *A*, energy or work *W* is needed, which is proportional to the change of the interface *dA*. The interfacial tension is the proportionality factor γ, which is expressed as force per area (N/m²).

$$dW = \gamma dA \tag{2.1}$$

The IFT is interpreted as the increase in the Helmholtz or Gibbs energy of the system, from a thermodynamic point of view, under the assumption that the interface *A* is increased reversibly by an infinitesimal amount *dA* at constant pressure *p* and temperature *T*.

$$dG = \gamma dA \tag{2.2}$$

$$\gamma = \left(\frac{\partial G}{\partial A}\right)_{p,T} \tag{2.3}$$

The oil droplets will coalesce without a surfactant present in the emulsion. The minimization of the interface, which is energetically favored, is the driving force for this coalescence. On the contrary, creating new interfaces is energetically unfavored. This is also the reason why water forms droplets on hydrophobic surfaces to minimize the interface.[39-41]

Surface active agents (surfactants) can be added to the two phase system to avoid coalescence. The adsorption of these surfactants at the O/W interfaces reduces the IFT and stabilizes for example oil droplets in aqueous solutions. Due to the amphiphilic properties, proteins and tensides are surface active. When they adsorb at the interface, their hydrophilic parts are oriented towards the polar phase and the hydrophobic parts towards the apolar phase.[42, 44] Proteins and tensides are the most common examples for substances with amphiphilic characteristics.[41-44] Nevertheless, the energy is not the only possibility for the stabilization. Steric and electrostatic repulsion can also prevent oil droplets that are covered with surfactant from approaching each other near enough and consequently prevent coalescence.[41, 43]

The amount n^{σ} of molecules *J* at the interface per area σ is defined as surface excess Γ.

$$\Gamma_J = \frac{n_J^{\sigma}}{\sigma} \tag{2.4}$$

With the surface excess, the change of the IFT $d\gamma$ can be linked to the change of the potential of the adsorbing substances $d\mu_J$. Gibbs derived the relation between the change in surface tension and the composition of a surface expressed by the surface excess and the Gibbs isotherm is described as follows:

$$d\gamma = \sum_J \Gamma_J d\mu_J \tag{2.5}$$

The model with the best founded theoretical background that describes the dependence of the IFT on the surfactant concentration *c* at a constant temperature *T* is the Gibbs isotherm equation.

$$\left(\frac{\partial_\gamma}{\partial_c}\right)_T = -\frac{RT\Gamma}{c} \tag{2.6}$$

However, this model is only valid for low molecular weight substances.[41, 45] The adsorption model of proteins is more complicated due to structural changes during the adsorption. Globular proteins like bovine serum albumin (BSA) have mainly polar amino acid residues at the surface and keep the majority of their apolar amino acid residues in the core. For the adsorption at hydrophilic/hydrophobic interfaces, this amphiphilic characteristic is essential. To interact with hydrophobic interfaces, these proteins have to expose their apolar residues, which requires the protein to unfold. Proteins with an α-helix or random structure in their native conformation tend to unfold to β-sheet structures during this process. In contrast, proteins that contain β-sheet structures in the native state will lose this structure motif. Moreover, electrostatic attraction, hydrogen bonding and van der Waals forces are as well involved in the protein adsorption. The following steps are involved in the protein adsorption at fluid interfaces:

- Bulk diffusion
- Barrier overcoming
- Adsorption at the interface
- Protein unfolding
- Diffusion of additional proteins
- Protein-protein rearrangements of the protein adsorption layer
- Phase transition
- Ageing of the protein adsorption layer

The result is a stabilized interface with the extent and morphology of protein denaturation depending on the protein stability and structure.[46, 47]

By measuring the IFT using pendant drop surface tension measurements, the protein adsorption at liquid/gas or liquid/liquid interfaces can be observed.[48] This process of adsorption was divided into three regimes by Beverung and coworkers: (I) induction period, (II) monolayer saturation and (III) interfacial gelation.[49]

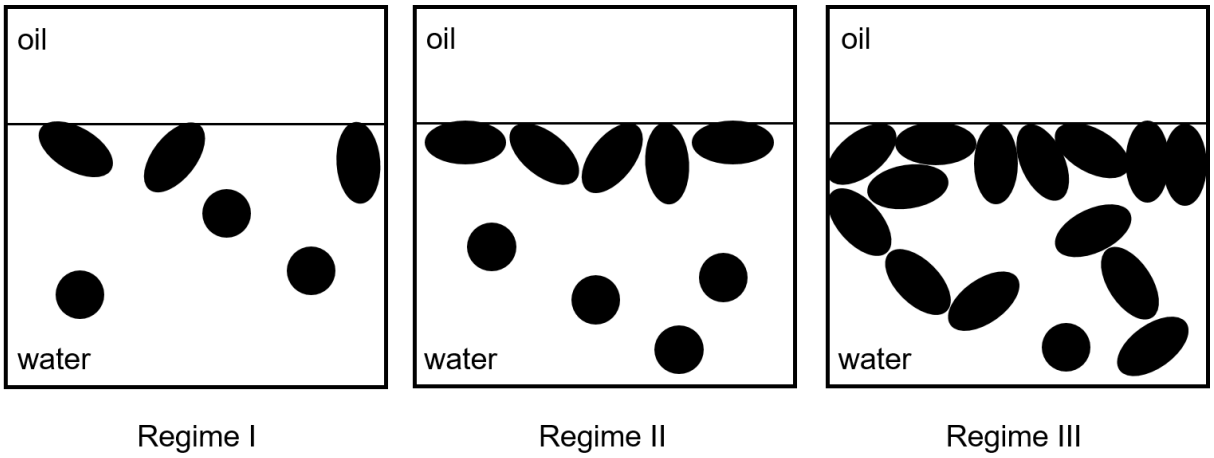

Figure 2.1 Three regimes with corresponding protein assembly present at the O/W interface. Circles represent proteins with native conformation and ellipses represent proteins with changed conformation.

In the first regime, the diffusion of proteins to the interface begins and first conformational changes of adsorbed proteins take place to expose their apolar residues. Only a minimal influence on the IFT can be observed since the amount of adsorbed protein is still small. As a result, the IFT values are close to the pure solvent. This regime can only be observed for very low protein concentrations. Subsequently, more proteins diffuse to the interface, where the self-assemble while changing their conformation to increase the contacts between apolar amino acid residues and the hydrophobic surface. This leads to an increase in the interfacial protein concentration and a saturation of the protein monolayer at the O/W interface. In this second regime, the time-dependent IFT has a sharp decline. In the third and last regime, a connected network of proteins is formed at the interface. The IFT is decreasing with a slower rate and after leveling out it reaches a minimum and the equilibrium state.[46, 47, 49]

Furthermore, protein adsorption is dependent on external conditions such as pH, ionic strength, protein concentration, additives and temperature.[46, 47, 49] In the literature, a detailed description of these affecting parameters can be found.[50]

A mathematical description for the adsorption of proteins at hydrophilic/hydrophobic interfaces is offered by various theoretical models. It is proposed that only unfolded proteins adsorb at the interface resulting in structure stability. On the contrary, it is also proposed that the protein unfolding at the interface causes an increase in surface pressure.[46]

The relation between adsorption of proteins, which can adsorb with two different modifications with different partial molar area, was first derived by Joos and Serrien.[51] The Serrien model

describes the time-dependent interfacial tension γ with the interfacial tension in equilibrium γ_{eq} and two exponential functions:

$$\gamma(t) = \gamma_{eq} + \left[\alpha\, exp\left(-\sqrt{\frac{4t}{\pi\tau}}\right) + \beta\right] exp\,(-kt) \tag{2.7}$$

The diffusion with the relaxation time τ, which depends on the equilibrium surface concentration, the diffusion coefficient D and the protein the protein concentration c (Eq. 2.8), is described in the first exponential term.

$$\tau = \frac{\Gamma_{eq}^2}{4Dc^2} \tag{2.8}$$

The second exponential term describes the reorientation and the formation of a protein layer at the interface with the kinetic constant of reorientation k, while α and β are parameters such that $\alpha + \beta = \gamma_0 - \gamma_{eq}$ (with γ_0 being the surface tension of the solvent).[47, 51]

2.2. Three Phase Contact Angle and the Formation of Pickering Emulsions

The three phase contact angle θ determines the shape of sessile water droplets on solid surfaces under an apolar fluid (oil, air). It is the angle between the liquid/liquid (or liquid/gas) interface and the tangents to the solid surface and describes the wettability of a particle surface. θ depends on the morphology and chemical composition of the surface and also on the oil-water interfacial tension. Water droplets have $\theta > 90°$ on hydrophobic surfaces and with decreasing hydrophobicity of the surface θ decreases as well. When the surface is wetted equally by oil and water, a droplet wit $\theta = 90°$ can be observed. Thus, a further a decrease in hydrophobicity results in $\theta < 90°$ (Figure 2.2).[52]

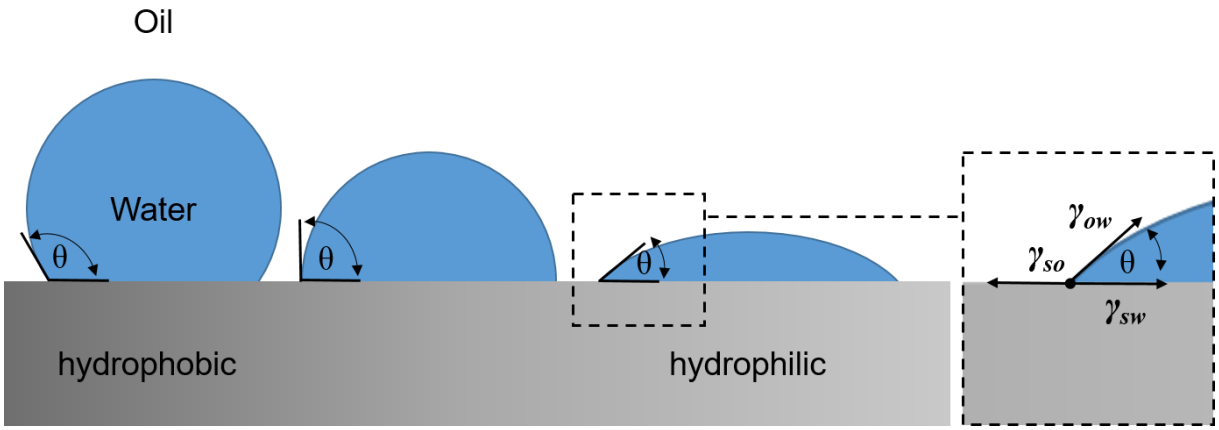

Figure 2.2 Water droplets with different contact angles θ under oil on a solid surface.

According to the Young's equation, the contact angle depends on the interfacial tensions at the particle-water, solid-oil and oil-water interfaces, respectively γ_{sw}, γ_{so} and γ_{ow}:

$$cos\theta = \frac{\gamma_{so} - \gamma_{sw}}{\gamma_{ow}} \tag{2.9}$$

After the attachment to the oil-water interface, this equation is also adaptable for a colloidal particle as shown in Figure 2.3. Here, the three phase contact angle is conventionally measured through the aqueous phase.[52]

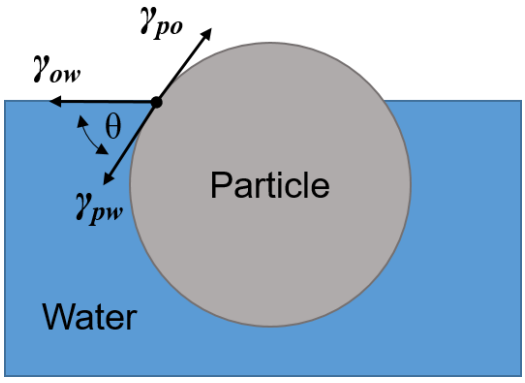

Figure 2.3 Solid spherical particle attaches to the oil-water interface developing the contact angle θ.

Neither the formation of a meniscus around the particle nor the deformation of the liquid interface is assumed in Figure 2.3. Under partial wetting conditions, the adsorption of solid particles is very strong. The free energy of attachment for a spherical particle of radius *r* from the water phase is related to the interfacial tension and the size of the solid particle:[52, 53]

$$\Delta G_{aw} = -\pi \cdot r^2 \gamma_{ow} (1 - cos\theta)^2 \quad (2.10)$$

For the attachment from the oil phase, the equation has a plus sign instead of a minus sign in the brackets of the equation (2.10). When the contact angle is 90°, the adsorption is the strongest corresponding to a maximum stability of emulsions.[54] A particle only wetted by water exhibits a three phase contact angle θ of 0° and does not change the free surface energy of the system. Increasing the oil wettability of a particle increases θ and due to the particle attachment the free surface energy is reduced. When θ is above 90°, the particle is more wetted by oil than by water further reducing the surface energy.

Furthermore, θ also determines the preferred emulsion type. In case of a closely packed particle layer on a liquid-liquid interface, the liquid with the poorer wettability on the particles has the preference to become the dispersed phase of an emulsion. When a liquid-liquid interface forms a curve, one side is being stretched, while the opposite side is being compressed. Surfactants with a small hydrophilic part and a comparable large hydrophobic part force the interface to curve towards the aqueous side, because upon compression the smaller hydrophilic parts can be more easily packed. The same applies to particles. Closely packed particles at the oil-water interface with θ > 90° for example block the curving towards the oil phase, because the major part of the particles is immersed in this phase. Due to the excess space for the particles, curving towards the aqueous phase is easier. Therefore, particles with θ > 90° tend to stabilize W/O emulsions and particles with θ < 90° stabilize O/W emulsions (Figure 2.4).[55, 56]

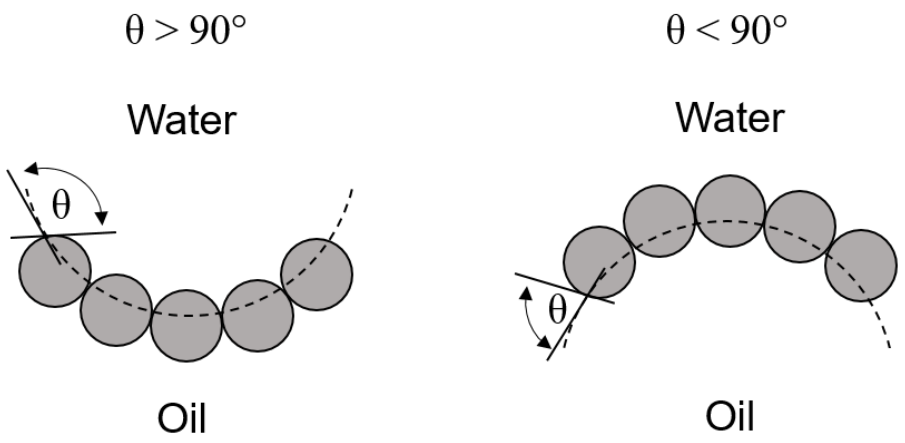

Figure 2.4 Type of emulsion depending on the three phase contact angle θ.

However, for particles with intermediate wettabilities the type of particle stabilized emulsions also depends on the volume fractions of the liquid phase.[54] Emulsions that are stabilized by

solid particles are called Pickering emulsion. S. U. Pickering was the first to report the stabilizing effect of solid particles in O/W emulsions.[57] These particles do not have to be amphiphilic and can be inorganic or organic. The stabilization with particles is similar to the stabilization with surfactants. For the system, the sum of interaction energies between particle/apolar phase and particle/polar phase can be more favorable than the energy of the direct interaction between the apolar and the polar phase leading to an energetic stabilization. Similar to surfactants surface coverage with particles enables steric and electrostatic stabilization as well.[43, 58, 59] As a result of aggregation the solid particles adsorb at the O/W interface and form a particle layer, which leads to a mechanical barrier preventing the droplets from coalescence. By means of attractive interactions, that are required for the formation of a rigid layer of solid particles, these particles are held together at the O/W interface. Notably, capillary forces are specific to particles adsorbed at the liquid/liquid interface. The droplet size as well as the emulsion type (O/W or W/O) can be controlled by the choice of particles. Hydrophobic particles favor W/O Pickering emulsions, while hydrophilic particles favor O/W Pickering emulsions.[53]

In this thesis, protein microcapsules are formed from O/W emulsions stabilized by a BSA layer around the oil droplets. Furthermore, the Pickering effect will be used for the formation of composite BSA microcapsules with various solid particles in the capsule shell.

2.3. Bovine Serum Albumin

Bovine serum albumin (BSA) is one of the most studied proteins, because of its abundance, and in many protein assay system the most popular standard protein. Proteins, which are omnipresent in nature, consist of a selection of 20 covalently bonded amino acids. The first level of the protein structure is built by this linear amino acid sequence and known as the primary structure. Three-dimensional structures, also called secondary structure, are formed by hydrogen bonds between or within adjacent peptide chains. The most common examples of such secondary structures are α-helices, β-pleated sheets and β-turns. Due to non-covalent interactions between amino acid side chains such as hydrogen bonds, hydrophobic interactions, ionic bonds or disulfide bonds, the three-dimensional arrangement of the secondary protein structures builds the tertiary structure. Several proteins cluster together and form a superstructure, which is the quaternary protein structure. External stimuli such as high temperatures, organic solvents (e.g. alcohol or chloroform), extreme pH values, acids and bases

or inorganic salts can destroy the secondary and tertiary protein structure and the loss of this native structure is termed denaturation.[60-62]

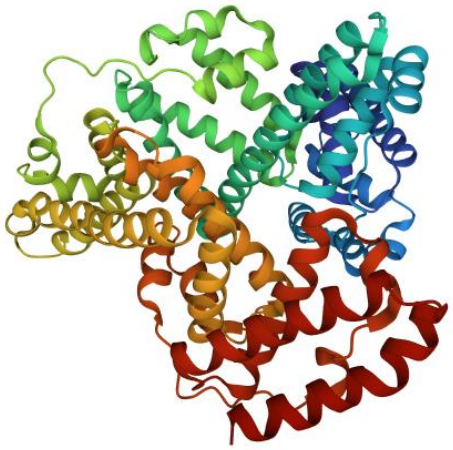

Figure 2.5 3D structure of BSA.[63]

BSA is a globular protein, which means it exhibits a spherical structure, where the hydrophilic parts are mainly located at the exterior and the hydrophobic groups are mainly in the interior of the protein structure, therefore it is water-soluble.[60-62] The protein structure of BSA is shown in Figure 2.5. Moreover, it is the most acidic protein in serum with an isoelectric point of 4.75. Comprising almost 50 to 60% of the total plasma proteins, BSA is the most abundant protein in the serum. It is produced in the liver and is one of the most soluble proteins that can be dissolved in water up to a concentration of 30% (w/v). BSA is made of 583 amino acids and is usually a monomeric protein with a molecular weight of 66 kDa, but dimers are present as well. Furthermore, it has 17 disulfide bonds and one free thiol group. Its structure is organized in nine loops that are grouped as three homologous domains with a length of 14.1 nm and a width of 4.1 nm. About the half of the amino acid residues are in the alpha-helical conformation. Along its structure the molecule is non-uniformly charged with a nearly neutral carboxyl terminus and a highly negative charged amino terminus. At pH 4 to 4.5 BSA changes from the native N state to a structurally loose and electrophoretically fast-moving species known as the F state. Fourty titratable carboxyl groups, which are hidden in the N state, appear due to this transition. In alkaline solutions up to pH 10 to 11, the N state is stable. Having two very strong and five strong binding sites, BSA works as a carrier of insoluble long-chain fatty acids. Typically, commercial preparations show microheterogeneity, which means that the BSA molecules are not identical and have minor differences. Thus, slight variations in physical

chemical behavior upon ion exchange, electrophoresis or salting-out procedures occur. This phenomenon arises from the precipitation from its natural source the blood serum, which is also the reason for the slightly yellow color.[64, 65]

2.4. Minerals relevant for Biosystems

The synthesized composite materials in this work consist of either hydroxyapatite, silicon dioxide or calcium carbonate as main inorganic component chosen because of their biocompatibility. Therefore, these minerals will be presented in more detail in the following section.

2.4.1. Hydroxyapatite

One of the most important biominerals in nature are calcium phosphates, which are abundant in biological systems as in bones and teeth and in geological environments.[66-68] Calcium phosphates reach high interest in material research of biomedical applications, especially in bone tissue engineering,[69-72] since they have excellent biodegradability and bioactivity, which strongly depend on the crystallinity, purity and the Ca/P ratio.[67, 73]

The least soluble and second most stable calcium phosphate in humid atmospheres and fluids under neutral to alkaline conditions is hydroxyapatite (HAP). Moreover, it is the main component of bones. The formula of HAP is $Ca_5(PO_4)_3OH$ or $Ca_{10}(PO_4)_6(OH)_2$, which is the formula of the unit cell displaying that the crystal unit cell contains two molecules. It exhibits a Ca/P ratio from 1.67 for stoichiometric HAP to ~ 1.5 for calcium deficient HAP. Its structure can be hexagonal or monoclinic, which is thermodynamically more stable. Only at stoichiometric conditions the monoclinic structure is formed, while the hexagonal structure is formed at non-stoichiometric conditions because of impurities and therefore mainly found in nature.[66-68, 74] Furthermore, the hexagonal crystal structure is assigned to the space group $P6_3/m$ with lattice parameters a = b = 9.4303 Å, c = 6.8911 Å and $\gamma = 120°$. The monoclinic crystal structure is assigned to the space group $P2_1/b$ with lattice parameters a = 9.84215 Å, b = 2 Å, c = 6.8815 Å and $\gamma = 120°$.[67] The ordering of the hydroxyl groups is the difference between those two HAP structures. In the hexagonal structure, the hydroxyl groups have a random

ordering (O-H, H-O, O-H, H-O) and in the monoclinic structure they have an alternating ordering (O-H, O-H, O-H).

All biological calcium phosphates contain impurities, which are ion substitutions of foreign ions into the crystal lattice. The following ion substitutions are common in biological apatites: OH^- and Cl^- can be substituted by F^-, while OH^- and PO_4^{3-} can be substituted by CO_3^{2-} and Ca^{2+} by Sr^{2+}, Na^+ or Mg^{2+}. For example, in tooth enamel F^- increases the crystallinity, stabilizes HAP and its solubility product becomes four orders of magnitude smaller, whereas $Zn^{2+}$and Mg^{2+} inhibit the crystal growth of HAP.[68]

In biomedical applications such as dental implants, bone cement, toothpaste additive or matrices for controlled drug release HAP reaches high interest.[71] Additionally, it is used as sorbent for poisonous chemical substances[75] and as carrier for various catalysts.[76-78]

Over the last century, different methods to synthesize nanocrystalline HAP presented: plasma spray process,[79] solution spray dry method,[80] chemical vapor[81] and plasma deposition,[82] solid state mixing,[83] sol-gel method,[84] ultrasound[85] and mechanochemical processing,[86] flux cooling method,[87] hydrolysis method,[88] hydrothermal method,[89] patterning process,[90] microemulsion techniques[91] and precipitation method.[92]

2.4.2. Silicon Dioxide

The principal component of sand is silicon dioxide (SiO_2). Since millions of years, zooplankton radiolarians and phytoplanktonic diatoms have used SiO_2 in their shells. It is a mostly colorless and hard substance with high melting point. SiO_2 can be amorphous or crystalline. For the noncrystalline form, glass is the most known example, while quartz is the most common crystalline form. Biosilica, which is generally amorphous as well, and glass only have a softening point. SiO_2 in the rather inert crystalline state occurs in several forms: for example cristobalite, quartz and tridynamite, which exist in a low temperature (α) and high temperature (β) form, as well as stiskovite. These different forms of SiO_2 have the basic Si–O–Si structure but different Si–O–Si angle and/or Si–O bond lengths.[93, 94]

Because of its biocompatible and non-toxic characteristics, SiO_2 has reached a lot attention in the last decade. Moreover, the surface of silica is rich in hydroxyl groups, which enables its modification by several different functional moieties such as antibodies, polymers or

alkoxysilanes. By siloxane chemistry, the surface modification can be realized to obtain multifunctionality. There is a large of syntheses for various silica nanostructures such as core-shells, mesoporous silica or spheres.[95]

2.4.3. Calcium carbonate

Found throughout the earth's crust and in organisms, calcium carbonate is a naturally occurring compound. It is used of most organisms for their inorganic materials followed by silica and calcium phosphate. Five crystalline modifications and an amorphous form of calcium carbonate are known. Three of the crystalline modifications are anhydrous (aragonite, vaterite and calcite) and two are hydrates (monohydrocalcite and ikaite). The thermodynamically most stable phase under ambient conditions is calcite, which is used in many materials. Aragonite is the next stable modification that is stable when large amounts stabilizing additives of magnesium are present and common in nature as well.[96-102]

The different mineral forms of calcium carbonate depend on the conditions at its formation such as pressure and temperature. With calcium in the center and a carbonate group at each of the vertices, the structure of calcium carbonate in minerals can be viewed as triangle. Various organisms extract and synthesize calcium carbonate from seawater that is used in skeletal structures. Marine organisms such as coccolithophores, coralline algae, corals, foraminiferans, mollusks and sponges use dissolved calcium carbonate and carbon dioxide to generate calcium carbonate. In the form of aragonite skeletons calcium carbonate is secreted by corals, while oysters from pearls by secreting calcium carbonate to encase foreign objects inside their shells.

In the industry, calcium carbonate is widely used as filler and coating pigment to whiten paper. The second most common use of calcium carbonate is in the production of polyvinyl chloride, polyolefins and thermoset polyesters by replacing the more expensive resins. Moreover, it is an additive to coatings and paints for various purposes such as anti-corrosion, opacity control, particle size distribution, pH control and weather resistance.[93]

2.5. Ultrasound for the Formation of Capsules

According to the frequency ranges, sound waves are divided into three main groups: a) infrasound with frequencies below 16 Hz; b) acoustic, which has frequencies from 16 Hz to 16 kHz and c) ultrasound with frequencies from above 16 kHz (higher than the human ear can respond to), while the upper limit is usually 5 MHz for gases and 500 MHz for liquids and solids.[103, 104]

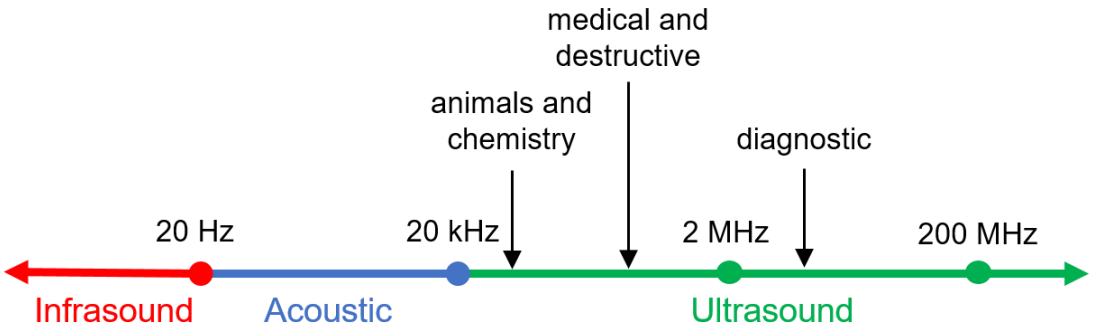

Figure 2.6 Frequency range of sound waves.

Within the large frequency range, the use of ultrasound is further divided into two areas. The high energy (low frequency) waves between 20 and 100 kHz are used for plastic wielding, cleaning and to affect chemical reactivity in nanomaterial synthesis and catalysis. The low amplitude (high frequency) waves known as low power or high frequency (diagnostic) ultrasound are used to measure the absorption coefficient and velocity of the wave in a medium in the range from 2 to 10 MHz. These waves are employed in chemical analysis, medical scanning and the study of relaxation phenomena. The application of ultrasound in material chemistry is extended and can be found in the following categories: chemical reactions (chemical synthesis,[105-107] polymer degradations,[108] kinetic studies,[109] structural determinations,[110] production of new types of nanoparticles[111, 112] and fabrication of highly non-equilibrium structures.[113, 114] All these possible applications of ultrasound irradiation in chemistry and physics make ultrasound an important and unique tool in nanotechnology.

While an acoustic field is applied to a liquid, the pressure waves of the sonic vibrations create an acoustic pressure P_a propagating through the medium, which must be added to the ambient (barometric) hydrostatic pressure P_h, present in the medium.[103, 115] The applied acoustic pressure is time dependent and is represented by the following equation:

$$P_a = P_A sin2\pi ft \tag{2.11}$$

where P_A is the maximum pressure amplitude and f is the frequency of the acoustic wave. The intensity I of the wave that is the energy transmitted per second per square meter of fluid is described as follows:

$$I = \frac{P_A^2}{2\rho c} \tag{2.12}$$

where ρ is the density of the medium and c is the velocity of the sound in this medium. While the sound wave propagates through the liquid, oscillation of the molecules is induced relative to their mean rest position. By inducing the motion of molecules, the ultrasound transmits through a liquid by longitudinal motion as a pressure wave alternately compressing and reducing the density of the medium.

As the velocity of the sound in liquids is typically ~ 1500 m/s with acoustic wavelengths from 10 to 10^{-4} cm being far above atomic and molecular dimensions, the chemical effects of ultrasound are not caused by a direct interaction with molecular species.[116] Sonochemistry is mainly a result of acoustic cavitation, which is the formation, growth and implosive collapse of gas/vapor filled bubbles in a liquid.[117] This collapse of the bubbles is very fast occurring in a short time interval. The evolution of the bubbles and their collapse during cavitation results in the concentration of the sound energy and leads to the formation of localized transient hot spots. The compression of the gas inside the bubbles produces locally high pressures (1000 atm) and enormous heating (5000 K) during the final stages of cavitation.[118] These extreme conditions result in the formation of highly reactive species such as hydrogen ($H^{\cdot}$), hydroxyl ($OH^{\cdot}$) and hydroperoxyl ($HO_2^{\cdot}$) radicals and hydrogen peroxide (H_2O_2).[119-121] Numerous fast reduction-oxidation reactions can be initiated by these radicals. The bubble collapses cause a conversion of the surface energy into mechanical energy and heat. The chemical effects of ultrasound, which can be divided into three areas, were reported by Wood and coworkers:[110]

- Homogeneous sonochemistry of liquids
- Heterogeneous sonochemistry of liquid-liquid or liquid-solid systems
- Sonocatalysis (which overlaps the other two areas)

The physical effects of high-intensity ultrasound include bulk thermal heating, enhanced mass transport, emulsification and a variety of effects on solids.

The acoustic cavitation starts at a point known as cavitation threshold, which depends on different parameters such as:

- the ultrasonic generator performance (frequency, power output)
- reaction medium properties (viscosity, surface tension, vapor pressure, the type and concentration of the gas inside the liquid, presence of solid particles)
- operation parameters (applied external pressure and temperature of the irradiated liquid)
- geometry and size of the reactor

Irradiation frequency

The appropriate irradiation frequency to achieve changes in chemical reactivity is between 20 and 50 kHz.[103, 122] The possibility of cavitation in liquids decreases with increasing ultrasonic frequency. For an equivalent amount of chemical work, higher frequencies require more power, because at the higher frequencies the higher rates of molecular motions result in greater power losses. For example, to make water cavitate at 400 kHz ten times more power is required than at 10 kHz.[104]

Output power

Electrical energy is transformed into ultrasonic energy, which is a mechanical energy, by ultrasound generators.[123, 124] Usually, the power of the ultrasonic device is expressed as the electrical input or output power to or from the ultrasound generator. An increase in sonochemical effects will be provided by increasing the intensity of the ultrasound. The bubble sizes decrease with increasing frequency and increase with increasing power. The smaller bubbles exhibit sonochemistry, while the larger ones exhibit sonoluminescence.[103, 125]

Physical properties of the liquid

In viscous liquids, the cavitation process is more difficult to produce. Therefore, one of the basic factors that determines the nature and rate of collapse of the cavitation bubbles is the surface tension of the liquid.[116, 126, 127] It is possible to operate the various cavitation processes (erosion of solid surfaces,[128] sonoluminesence,[129] induced reactions,[130] etc.) by changing the surface tension of the liquid. An increase of the surface tension results in the enhancement of

the work of the cavitation bubble evolution. Consequently, the probability of microbubble formation decreases accompanied by the reduction of cavitation intensity. To reduce the surface tension and thus increase the efficiency of ultrasonic treatment, surface active materials (surfactants, functionalized nanoparticles, lipids, polyelectrolytes, etc.) can be added to the sonicated liquid.[116, 131-134] The accumulation of the organic solutes at the gas/aqueous interface of the cavitation bubbles can play an important role in numerous ultrasound induced/enhanced processes including polymerization reactions,[135, 136] biomedical applications,[137, 138] the destruction of pollutants and hazardous chemicals[139-141] and the formation of nanoparticles.[142-145]

Temperature of the liquid

Varying the temperature of the liquid is one of the simplest methods to modify the activity. Thus, the density of the bubbles, their size and dynamics in the cavitation field can be influenced.[146-148] A low temperature is favorable in sonochemistry since the vapor pressure is decreased under this condition.[103, 125] The rarefaction cycle will cause boiling of the liquid medium and the formed cavitation bubbles would be filled with solvent vapor, therefore in most cases it is not suitable to carry out sonochemical reactions in a solvent near its boiling point.[149] During the compression cycle the collapse of these bubbles would be cushioned and as a result extremely high temperature and pressure would be generated. It is possible that the bubbles would not collapse under these thermodynamic conditions. For that reason, it is important in sonochemistry to control the temperature of the cavitated liquid.[104]

The presence of gases

Any gas dissolved in the liquid would be forced out of the solution during the rarefaction cycle to form the nucleus of a cavitation bubble.[125, 146, 150] The motion of the bubbles is accompanied by a light emission known as sonoluminescence. The cavitation threshold and the shock wave intensity released after the collapse of the bubbles are lowered with increasing gas content in the liquid. Different types of bubbles are produced: a) empty bubbles (true cavitation bubbles), b) vapor filled bubbles, c) gas filled bubbles (unless the liquid medium is degassed) and d) a combination of vapor and gas filled bubbles.[151] The maximum temperature (T_{max}) and pressure (P_{max}) of the bubble at the moment of its collapse can be described as follows:

$$T_{max} = T_0 \left(\frac{P_m (K-1)}{P} \right) \tag{2.13}$$

$$P_{max} = P \left(\frac{P_m (K-1)}{P} \right)^{K/K-1} \tag{2.14}$$

where T_0 is the ambient (experimental) temperature, K is the polytropic index of the gas (or gas vapor) mixture, P is the pressure in the bubble at its maximum radius and P_m is the pressure in the liquid at the moment of transient collapse ($P_m = P_h + P_A$).[104] The following equation is an expression for the ratio T_0 (T_{max}):

$$\frac{T_0}{T_{max}} = \left\{ 1 + Q \left[\left(\frac{P_h}{P_m} \right)^{1/3\gamma} - 1 \right] \right\}^{3(\gamma-1)} \tag{2.15}$$

where Q is the ratio of the resonance amplitude to the static amplitude of vibration of the bubble and γ is the specific heat ratio of the gas within the bubble. Employing gases with large γ values high sonochemical effects are gained from gas-filled bubbles according to equations 2.13, 2.14 and 2.15. Therefore, monoatomic gases (e.g. He, Ar, Ne) are preferably used instead of diatomic gases (e.g. N_2, air, O_2).[104]

External (applied) pressure

Another parameter affecting the cavitation process is the external (applied) pressure. The cavitation threshold for the system and the released energy upon cavity collapse can be increased by increasing the external pressure.[103] Thus the cavitation may be suppressed, otherwise of the cavitation bubbles will not be sufficient. Furthermore, the hydrostatic pressure can influence the acoustic cavitation as well. The cavitation can be intensified by increasing the hydrostatic pressure since the intensity of the shock wave generated due to the collapse of the bubbles increased at higher pressure levels.[104]

Shape of the reaction vessel

For the correct application of the ultrasonication the shape of the vessel is critical. Some energy is reflected, when the ultrasonic wave impinges on any solid surface.[152] The reflected ultrasound is a minimum, when the base of the container is flat such as in a conical flask. In contrast, an

enormous proportion of the ultrasonic wave is reflected, if the base of the vessel is spherical and the ultrasonic wave hits the vessel at an angle.

2.6. Protein Microcapsules and Composite Microcapsules

The controlled delivery of active components for different application, for example in the biomedical field, requires encapsulation methodologies with high tenability and performance. In this context, promising materials are biocompatible polymers, protein capsules and hybrid polymer-protein capsules. For the preparation of protein capsules and shells there are numerous methods described in the literature. Methods to obtain micro- to nanoscale capsules based on micro-emulsion technology are most widely adopted and a variety of approaches for the controlled generation and stabilization of micro-emulsions have been used such as single emulsions, double emulsions,[153] polymerization techniques,[154] phase separation coacervation technique,[155] spray drying and spray congealing,[156] solvent extraction[157] and ultrasonic emulsification.[24] The characteristics of the materials used as components in the synthesis exhibit a significant influence on the stability of the final structures. The most important methods used for the formation and stabilization of protein capsules will be shortly described in this section.

To synthesize micro-containers from biopolymers using single emulsions, the proteins are dispersed in an aqueous medium followed by emulsification in a non-aqueous medium. Subsequently, physical or chemical cross-linking of the dispersed droplet is carried out to ensure the structural integrity. The cross-linking can be achieved by using chemical cross-linkers, such as glutaraldehyde, or intrinsically by means of heat, which has the advantage of minimizing undesired reactivity with other components and potential toxicity.[34]

With double emulsions more complex structures can be obtained. In this manner, the primary single water-in-oil emulsion is added to a further aqueous solution containing a second biopolymer, which will form the outer shell of the capsule and as a result a double emulsion is generated. Thus, this method allows the encapsulation of water-soluble species, which is suitable for the delivery of water-soluble drugs.[34]

The ultrasonic emulsification method to create protein microcapsules involves mechanical mixing by exposure of high-intensity ultrasonic waves to an oil/water interface. Consequently, an oil-in-water emulsion is formed where the protein molecules adsorb at the interface of the

droplet. This technique is well known and has been the topic of various reviews,[24, 33, 158, 159] it is also used in this work to generate protein microcapsules and in section 5.2., the mechanism of the formation of these microcapsules via ultrasonic emulsification will be described in detail.

By drying, the stability of single or double emulsions upon long-term storage can be enhanced. The dispersion medium of the liquid emulsion is removed and the encapsulant and liquid that protects the mono- or multilayers are transformed upon heat treatment in the solid state. Before its final application, the dried emulsions that are physically very stable can be liquidized again. Nowadays spray-drying is the most common technology used in food industry for the microencapsulation of food ingredients due to its technical availability and low costs.[160]

During this fast process of microcapsule formation via ultrasonic emulsification, one or more substances dispersed into the organic phase can be encapsulated into the capsules. Tetracycline (TTCL), which is an antibiotic drug with a broad spectrum of activity, was successfully encapsulated in sonochemically fabricated BSA microcapsules by Avivi and coworkers.[22] Using the same procedure anticancer Gemcitabine HCl (Gemzar)[161] and paclitaxel (Taxol)[162] were encapsulated by Grinsberg et al. Furthermore, these drugs can also be released and kill the desired cells. The loading process of sonochemical fabricated protein microcapsules is, compared with protein microcapsules of other formation methods, short and highly efficient.

Additionally, to create protein shells different groups combined proteins and a second component for electrostatic interactions in layer-by-layer synthesis routes.[163, 164] Möhwald and coworkers employed layer-by-layer templating of proteins, which were then cross-linked to form a stable shell. They first adsorbed BSA on the $MnCO_3$ particles and subsequently added the dispersion to a glutaraldehyde solution to cause a reaction of its aldehyde groups with the amine groups of BSA. By incubation in low molar HCl, cores could be dissolved, which results in hollow 5 µm capsules with BSA shells.[5] Later on Mertz and Caruso et al. developed a non-covalent linking method based on physical adsorption by functionalizing silica templates with bromoisobutyramide that acts as an intermolecular linker of adsorbed human serum albumin.[165]

A further class of microcapsules are composite microcapsules whose shells are composed of different components such as proteins or polymers and colloidal particles. By stabilizing the emulsions mainly through self-assembly of colloidal micro- or nanoparticles at the liquid-liquid interface these microcapsules are generated. Here, the colloidal particles serve as modular building blocks and this allows the incorporation of their characteristics into the functional capabilities of the microcapsules. Through the choice of the particles the physical

characteristics of the composite microcapsules like biocompatibility, mechanical strength and permeability can be controlled.[166] For the synthesis of these microcapsules with densely packed colloidal particle shells, different methods have been introduced including the Pickering emulsion based formation, colloidal particle deposition on templates and amphiphilicity-driven self-assembly of nanoparticle vesicles from polymer-grafted colloids.

The formation of composite capsules trough Pickering emulsions includes the synthesis of a water-in-oil or an oil-in-water emulsion with particles dispersed in one of the two phases and the adsorption of these particles at the oil-water interface of the emulsion droplets. Emulsion based composite capsules are the topic of several reviews and research papers.[166-168] The tendency of the particles to adsorb and stay at the interface depends on different factors such as the radius of the particles and their surface chemistry, influencing the wettability of the particles by the water and oil phase. In section 2.2. and 8.1., more details can be found.

The templated formation of composite capsules was introduced by Caruso in 1998 by reporting the sequential adsorption of SiO_2 nanoparticles and oppositely charged polyelectrolytes on polystyrene template particles through electrostatic interactions.[169] A precise control of the shell thickness is enabled by depositing a defined number of layers on the template. Thus, this layer-by-layer templating method determines the size and morphology of the capsules.

Furthermore, Eisenberg and coworkers introduced the self-assembly of amphiphilic block copolymers into different morphologies, including spherical vesicular structures, two decades ago.[170] For the formation of capsules with colloidal particles in the shell, the principle of amphiphilicity-driven self-assembly has been transferred to colloidal particles. This self-assembly of amphiphilic polymer-grafted particles to vesicle-like capsules has been controlled by different techniques such as emulsification by preparing oil-water emulsions and following evaporating of the organic solvent,[171] dialysis from a selective solvent against water to slowly change the solvent composition[172] or by drying a thin film of the particles on the wall of a vial and subsequently rehydrating the film.[173]

3. Materials and Methods

This chapter gives data about all used chemicals and their origin. Moreover, all methods that were used in this work are briefly described. Analytical instruments and their application are introduced as well.

3.1. Chemicals

Protein microcapsules

Bovine serum albumin (BSA, > 95%) was purchased from Alfa Aesar (Germany). Toluene (≥ 99,5%) was purchased from Th. Geyer (Germany), Miglyol 812 was purchased from Sasol (Germany) and mint oil was purchased from Hofmann und Sommer GmbH (Germany). Bis(2-hydroxyethyl)amino-tris(hydroxymethyl)methan (BisTris, ≥ 99%) buffer solution and Dithiothreitol (DTT, ≥ 99%) were purchased from Carl Roth (Germany).

Inorganic nanoparticles

Diammonium hydrogen phosphate and calcium nitrate tetrahydrate (≥ 99%) was purchased from VWR (Germany). Citric acid monohydrate was purchased from Carl Roth (Germany). Ammonium hydroxide (28–30%) was purchased from Merck (Germany). The aqueous Ludox Cl suspension (aluminum oxide coated silica NPs, 30 wt%) containing spherical particles with a size of 25 nm and a zeta potential of +30.9 ± 0.5 mV (pH = 6.5) was purchased from Sigma Aldrich (Germany). Dry spherical silica particles with a primary particle size of 25 nm and a zeta potential of -33.2 ± 0.1 mV (pH = 7.0), whose surface was partially modified with dichlorodimethylsilane (DCDMS, 71% of surface silanol groups remained intact) and called as Si71 were purchased from Wacker GmbH (Germany). Spherical calcium carbonate NPs with a size of 20 nm, whose surface was modified with stearic acid, was purchased from GetNanoMaterials (France). After the hydrophilization of these hydrophobic calcium carbonate NPs by ultrasound treatment they exhibit a zeta potential of -15.3 ± 1.3 mV (pH = 7.4). The different NPs are shown in Figure 3.1.

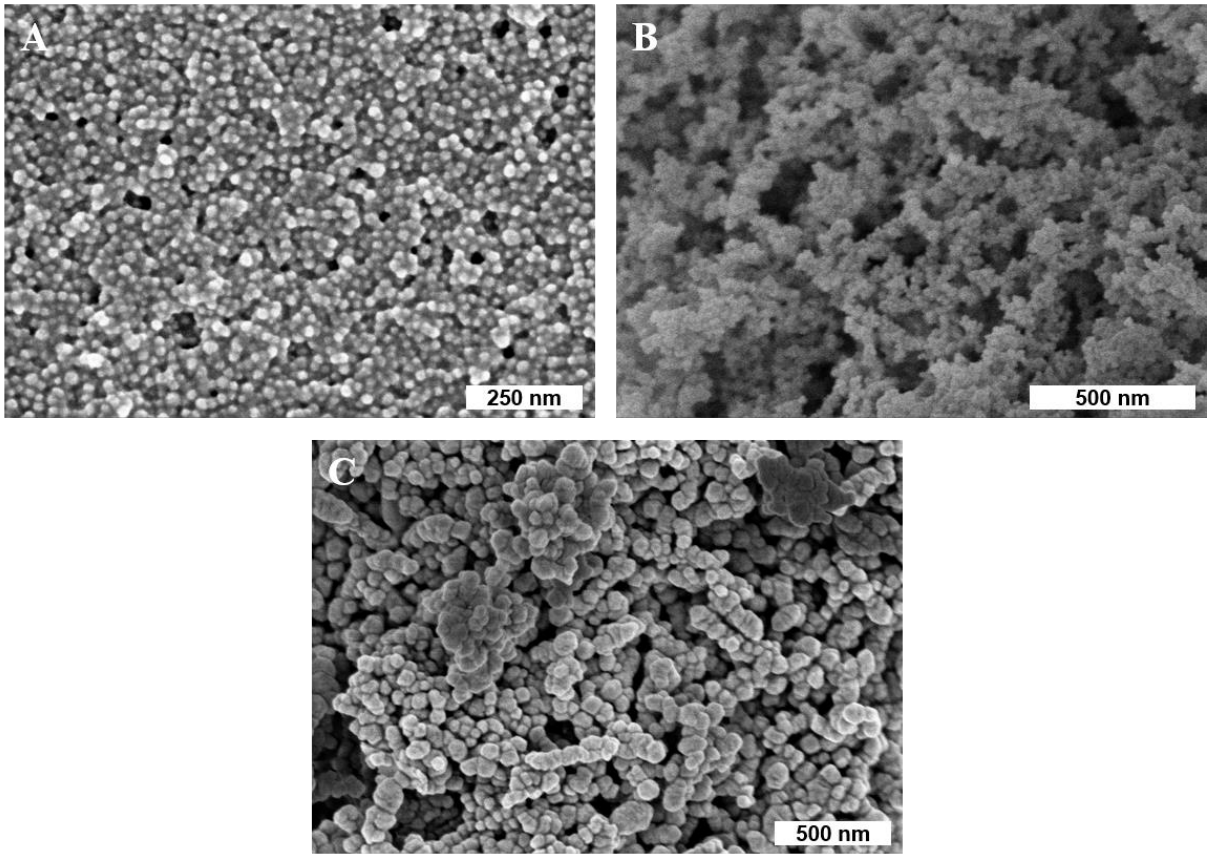

Figure 3.1 SEM images of different nanoparticles: Ludox Cl (A), Si71 (B) and $CaCO_3$ (C).

Modification

3-Aminopropyltriethoxysilane (APTES, 97%) was purchased from Alfa Aesar (Germany). Fluorescein isothiocyanate (FITC) was obtained from Riedel-de Haën (Germany). Ethanol (≥ 99,5%) was purchased from Th. Geyer (Germany) and Dimethylsulfoxid (DMSO, (≥ 99,8%)) from Carl Roth (Germany).

3.2. Optical Microscopy and Fluorescence Microscopy

A light microscope produces magnified images of objects using light. The illumination of the sample may be from above (incident-light illumination) or from below (transmitted-light illumination), which is more typical. The condenser focuses the radiation from a light source at the sample. Subsequently, the objective lens focuses the radiation leaving the sample to form an intermediate image. Then, the ocular refocuses the radiation to form an image on a detector. A basic compound microscope forms a brightfield image in which the details of the sample appear dark on a bright background. With aberration-free lenses of maximum aperture,

improvement of numerical aperture by use of immersion oil and illumination by radiation of minimum wavelength the optimal resolution is obtained. However, the Abbe resolution limit for a microscope is described by the following equation:

$$d = \frac{\lambda}{2n\,sin\alpha} \tag{3.1}$$

where *d* is the minimum resolvable distance, λ is the wavelength of the used radiation, *n* is the refractive index of the medium in which the diffraction occurs and α is the aperture angle of the lens. The resolution limit or Abbe-limit calculated with this equation is 0.2 µm.[174]

The same set up is used in fluorescence microscopy. The light source is the only difference because a fluorescence microscope uses the light of a specified wavelength. Therefore, the emitted light of a lamp with a broad spectral range like a mercury-vapor lamp is filtered. Often a combination of colored glasses and interference filters is used. The absorption of the filtered light induces transitions of the electron in the sample to the excited state. When the excited electrons relax to a lower energy state light is emitted occurring as fluorescence. Another filter separates the illumination light from the much weaker emitted fluorescence.[175]

All light and fluorescence images were taken with a DMi8 (Leica) at the highest magnification with the 100x oil objective. The LAS X software from Leica was used for image processing.

3.3. Cryo Scanning Electron Microscopy

In a scanning electron microscope (SEM) the surface of a sample is scanned point by point by a focused electron beam and the corresponding emitted electrons are used to generate an image. When the accelerated primary electrons hit a sample, they are scattered. A small fraction of the primary electrons are elastically backscattered (BSE, backscattered electrons), while most of them are inelastically scattered resulting in atomic electrons ejected from the sample, which are called secondary electrons (SE). The signals of the detected SE or BSE are used to display the surface topography of the sample.

The used electron source (electron gun) can be a tungsten filament, a LaB_6 or Schottky emitter, or a tungsten field-emission tip. The electron beam scans the sample in raster pattern regularly moving in an x-y coordinate system. To avoid collisions of the electrons with air molecules the sample is placed in an evacuated chamber. Furthermore, non-conductive samples have to be

sputtered with a thin layer of metal or carbon to avoid charges, which would deflect the electrons.[174, 176]

For the images in this work two cryo SEM were used: a S-4800 (Hitachi) with a Gatan–Alto 2500-S as cryo preparation system and a Jeol 7500F with a Gatan–Alto 7500. The samples were sputtered with platinum.

3.4. Energy Dispersive X-Ray Spectroscopy

A combination of a visual and an elemental analysis of a sample can be performed by using a SEM coupled with an energy dispersive X-ray (EDX) detector. An electron beam hits the sample leading to the removal of an inner shell electron because it transits to a high energy level. Another electron at a high energy level fills the resulting hole in the inner shell causing emission of a characteristic X-ray with energy between those two energy levels. Elements can be identified because the characteristic X-rays have a specific energy corresponding to each element.[177]

EDX spectra were recorded with a Xmax 150 and a Xmax 80 from Oxford mounted on a Jeol 7500F.

3.5. X-Ray Diffraction

The X-Ray Diffraction (XRD) is the most important method for the structural clarification of crystalline materials. For the generation of the X-rays an X-ray tube is used. The cathode emits the electrons, which are accelerated by a high voltage power source connected across cathode and anode and hit the anode with high energy. When decelerating the highly accelerated electrons on the anode X-rays are generated, whose wavelength and intensity is dependent on the applied high voltage (bremsstrahlung) and on the material of the anode (characteristic X-ray). The characteristic X-rays, whose formation was described in section 3.4., pass a monochromator, the created beam hits the sample and a detector records the intensity of the reflected X-rays at different angles.

The diffraction of the X-rays by a crystal lattice is the basic principle of this method. The atoms in this lattice scatter the X-ray waves causing destructive and constructive interferences. These waves are determined by Bragg's law:

$$n\lambda = 2d\ sin\theta \tag{3.2}$$

Where n is any integer, λ is the wavelength of the beam, d is the spacing between the diffracting planes and θ is the incident angle. Thus, information on the positioning of the atoms in the crystalline material are received.[178]

The Empyrean powder X-ray diffractometer from PANalytical (Almelo, Nl) was used to characterize the hydroxyapatite nanoparticles.

3.6. Raman spectroscopy

For the characterization of solids and molecules, Raman spectroscopy uses inelastic scattering. To investigate specific sample areas the spectrometer can be coupled to a microscope. A change in polarizability is necessary for a molecule to exhibit a Raman effect. By irradiating a sample with monochromatic light, usually from a high-intensity laser, in the ultraviolet, the visible or the near-infrared range a Raman spectrum is excited. At the frequency of the exciting radiation the strong Rayleigh line and shifted from this frequency further weak lines can be observed. The frequency difference of the scattered light relative to that of the incident light can be negative and positive, known as Stokes and anti-Stokes frequency, respectively. Is the wavelength of scattered light the same as the incident light, it is known as elastic scattering. Is the wavelength of the scattered light different, it is known as inelastic scattering. With energy change larger than 1 cm^{-1}, Raman scattering is an inelastic light scattering. The elastic scattered radiation (Rayleigh scattering) is filtered out and the light of the laser interacts with the molecular vibrations causing the energy of the laser to shift (Raman shift), which gives information about the vibrational modes in the sample.[179, 180]

All Raman data was acquired using a Witec Alpha 300 Raman microscope system (Witec, Ulm, Germany) equipped with a spectrograph (600 gr/mm grating) and an Andor DU401A-BR-DD-352 CCD camera (Andor, Concord, Massachusetts, USA).

3.7. Thermogravimetric Analysis

Thermogravimetric analysis (TGA) is a technique in which the mass of a sample is measured as a function of temperature. The sample is placed in a crucible, which is connected to a balance measuring the change of mass while the sample is subjected to a controlled temperature program in a controlled atmosphere. The used atmosphere plays an important role and can be inert, reactive or oxidizing. Mass changes occur when the sample reacts with the surrounding atmosphere or when the sample loses material in several different ways. This mass change can be caused by for example drying, loss of crystal water, evaporation of volatile constituents and oxidative decomposition of organic substances in oxygen or air.[181]

The thermal stability of the samples was measured by means of thermogravimetric analysis (TGA) with a TGA2 LF/1100/885 from Mettler. Each sample was heated from 30 to 700°C, except for the hydrophilized $CaCO_3$ that was heated up to 800°C, at a heating rate 10°C/min under air atmosphere.

3.8. Pendant Drop Tensiometry

The pendant drop tensiometry is a simple method to determine surface and interfacial tension. In this method, a drop of one liquid is created from a needle and suspended in another liquid inside a quartz cuvette. The shape of the drop is a result of the relationship between gravity and the interfacial tension. Inside the drop, an increased pressure is produced caused by the interfacial tension between outer and inner phase. The correlation between the pressure difference Δp, the interfacial tension γ and the radii of the curvature of the surface r_1 and r_2 is described by the Young-Laplace equation and defined as follows:

$$\Delta p = \gamma \left(\frac{1}{r_1} + \frac{1}{r_2} \right) \tag{3.3}$$

As a hydrostatic pressure is produced inside the drop due to the weight, the pendant drop is deformed under the gravity, which affects in radii r_1 and r_2 of the curvature and results in the characteristic pear shape of the pendant drop. From the shape of the drop the interfacial tension can be calculated, when the density differences between the phases is known. From a video image of the dosed drop the shape of the drop is determined. By fitting the drop shape to the

Young-Laplace equation and comparing this fit with a calculated drop profile the interfacial tension can be determined.[182-184]

All pendant drop measurements in this work were performed by using an OCA 15 (dataphysics).

3.9. Dynamic Light Scattering

The dynamic light scattering (DLS) is a useful tool for the determination of the diffusion coefficient, which depends on the shape and size of particles, and hence the hydrodynamic radius. When a laser light encounters a solution containing particles, the light scatters in all directions and the scattering intensity is recorded by a detector. The Brownian motion of the particles causes intensity fluctuations of the scattered light. Information on the size of the particles can be obtained when the movements of the particles are monitored over a time range as small particles move faster than larger particles. To determine how rapidly the intensity fluctuates, the digital autocorrelator correlates the intensity fluctuations of the scattered light with respect to the time.

Using the Stokes-Einstein equation the hydrodynamic radius (R_h) can be obtained:

$$D = \frac{k_B T}{6\pi\eta R_h} \tag{3.4}$$

Where D is the diffusion constant, k_B is the Boltzmann constant, T is the absolute temperature and η is the viscosity of the medium.[185]

The size distribution of the HAP NPs and the pristine and the cross-linked BSA was measured with a Malvern Zetasizer Nano ZS possessing a red 632.8 nm laser. Before the measurements, the samples were filtered with a syringe filter with a 0.2 µm PVDF membrane.

3.10. Laser Diffraction

Laser diffraction measurements give information about particle size distribution based on the principle that particles of a given size diffract light through a given angle. This angle increases with decreasing particle size.

A narrow beam of monochromatic light from a He-Ne laser (λ = 633 nm) is passed through a stream of dispersed particles (in liquid or air), usually between the windows of a sample cell. The particles diffract the light and generate angular diffraction patterns. A Fourier lens or a set of lenses focuses the laser beam onto a multi-element detector to measure the intensity of the remaining or the original light beam and the intensities of the light diffracted by the particles at different angles. Subsequently, a computer software converts the detected signals into a particle size distribution.[186-188]

The size distribution of the oil loaded BSA microcapsules was measured with a Malvern Mastersizer X.

3.11. Determination of Zeta Potential

The zeta potential (ZP) is the potential at a shear plane of a colloidal particle moving under an electric field and it reflects the potential difference between the electric double layer (EDL) of the particles and the layer of the dispersant around them. The EDL develops on the surface of a charged particle when it is dispersed. The inner layer (Stern layer) consists mainly of ions with opposite charge to that of the particle. The outer diffuse layer consists of oppositely and same charged ions due to the electrostatic field of the charged NPs. When an electric field is applied to a dispersion, the charged particles move towards the oppositely charged electrode and their mobility is measured by electrophoretic light scattering.

During electrophoresis the mobile particles scatter an incident laser. The scattered light has a different frequency than the original laser and this shift of the frequency is proportional to the velocity of the particles (Doppler shift). The particle velocity *V* is then derived from the Doppler shift and the ZP is calculated with the following equations.

The ZP is derived from the electrophoretic mobility μ_e of the charged particles under the applied field, which is calculated as follows:

$$\mu_e = \frac{V}{E} \tag{3.5}$$

where *E* is the strength of the electric field. From the obtained electrophoretic mobility the ZP is then calculated using Henry's equation:

$$\mu_e = \frac{2\varepsilon_r \varepsilon_0 \zeta f(Ka)}{3\eta} \quad (3.6)$$

in which ε_r is the dielectric constant, ε_0 is the dielectric constant of the vacuum, ζ is the ZP, f(Ka) is Henry's function and η is the viscosity.[189]

The zeta potential was measured with a Malvern Zetasizer Nano ZS possessing a red 632.8 nm laser.

3.12. Sodium Dodecylsulfate Polyacrylamide Gel Electrophoresis

Sodium Dodecylsulfate Polyacrylamide Gel Electrophoresis (SDS-PAGE) is the most widely used technique by which charged protein molecules are transported through a solvent by an electrical field and separated primarily by mass. The protein is denatured by heating at 70–100°C in the presence of excess SDS, which is a negatively charged detergent that unfolds proteins and breaks the interactions with other proteins. Furthermore, a thiol reagent is employed to break disulfide bonds. Thus, the reduced polypeptides bind the same amount of SDS and this complex forms a rod with its length roughly proportional to the molecular weight of the protein. Now all proteins are negatively charged and can be separated by their size. The proteins placed in particular wells migrate down through the polyacrylamide gel matrix towards the positive electrode and create lanes of protein bands, when an electrical current is applied. The distance they moved depends on charge, pore size and molecular weight. Smaller proteins progress faster through the gel than larger proteins, which are slowed down by the pores of the gel and therefore localized on the top of the gel.

The pore sizes in the gel are inversely related to the polyacrylamide concentration. To enable a broader range of protein sizes to be separated, gradient gels are prepared to have a low percentage of polyacrylamide at the beginning of the sample path and a high percentage at the end. A reference by which the mass of the protein samples can be determined is provided, when a set of proteins with known masses runs next to samples in the same gel. These sets of reference proteins are called molecular weight or mass markers.[190, 191]

3.13. Scanning Force Microscopy

Scanning force microscopy (SFM) is a topographic imaging technique with a high resolution. By detecting the near-field interactions between the surface of a sample and a very small tip, the sample can be imaged at atomic resolution. For SFM imaging there are two basic modes: contact mode and tapping mode. In the contact mode, the tip on the cantilever is brought carefully into contact with the sample and then scanned over the surface of the sample in a raster. The tip-sample interactions will induce the deformation of the cantilever by maintaining a constant force on the tip. By a photodetector these deformations can be detected by means of a laser and converted to an electrical signal, which is read by a computer. For this purpose, the laser is focused on the back of the cantilever and its reflection is projected on the photodetector. As a result, the sample topography is recorded. The tapping mode is similar to the contact mode. The exception is that the piezo (acoustic) or the magnetic coil provides a constant driving force leading to an oscillation of the tip at a certain frequency.

Additionally, SFM-based force spectroscopy is also an interesting approach to determine the interaction forces of biological systems. By recording the deflection of the cantilever while the tip approaches the surface, the SFM force curve is obtained, which can be used to extract information, such as elasticity and stiffness.[192]

Precise imaging of a dried BSA microcapsule that was loaded with toluene was conducted by SFM with a Bruker Dimension Icon with OTESPA-R3 tips (k = 26 N/m, f = 300 kHz).

The nanocompression measurements were performed with a SFM MFP-3D (Asylum Research) linked with an inverted microscope (Zeiss). The tipless cantilever HQ:NSC36 (k = 2,0 N/m, f = 180 kHz) from MikroMasch and a measuring speed of 1 µm/s was used. Before the measurements, the microcapsules were immobilized on a glass substrate that was covered with polyethylenimine. Subsequently, the measurements were carried out in a BisTris buffer solution (20 mM, pH 7) in a liquid measuring cell.

4. Experimental

The details of experimental techniques used in this work are described in detail in the following chapter.

4.1. Synthesis of Protein Microcapsules

The microcapsules were prepared following Suslick's method.[193] In a cylindrical vessel, 1.4 mL oil (toluene, Miglyol or mint oil) was layered over 2.1 mL of a 5% w/v BSA solution. The used ratio of aqueous/organic phase was 3:2 (v/v). A high-intensity ultrasonic horn with a tip diameter of 2 mm was placed at the oil-water interface. To maintain the temperature below 30°C during ultrasonication, the vessel was positioned in an ice bath. The sytems were sonicated for 3 minutes at an acoustic power of ~ 200 W cm^{-2}. Simultaneously, the systems were mixed with a magnetic stirrer. The obtained microcapsules were dialyzed against distilled water with pH of 6.2 ± 0.3 using a dialysis tube with a cutoff of 1000 kDa (Spectrum Labs Spectra/Por Dialysis Membrane Biotech CE) to remove residual chemicals and fragments of broken microcapsules.

4.2. Synthesis of HAP NPs

The standard synthesis route of the HAP NPs is based on the work of Jutz et al.[6] A 5 mM diammonium hydrogen phosphate solution was adjusted to pH = 9 with small amounts of a 1% ammonium hydroxide solution. A 10 mM calcium nitrate solution, which contained 2.5 mM citric acid, was added to an equal volume of the diammonium hydrogen phosphate solution under moderate stirring.

For the synthesis of composite protein-mineral microcapsules, the concentrations of the diammonium hydrogen phosphate and the calcium nitrate solution were doubled to 10 mM and 20 mM, respectively. Moreover, citric acid was not used and calcium nitrate was added while the diammonium hydrogen phosphate was sonicated at an acoustic power of ~ 100 W cm^{-2}. The obtained nanoparticle suspension was concentrated by centrifugation and redispersed with a 20 mM BisTris solution (pH = 7).

4.3. Synthesis of Composite Protein Microcapsules

In the first step, the NPs were pre-modified with BSA. For this purpose, a 1% NP suspension in distilled water (Ludox Cl, Si71, $CaCO_3$ or HAP) was added dropwise to an equal volume of a 5% w/v BSA solution in distilled water with pH 6.7. After thorough washing process including multistep washing and subsequent centrifugation at 14000 rpm, the BSA modified NPs were redispersed with a 20 mM BisTris solution (pH = 7).

The stearic acid covered $CaCO_3$ NPs were hydrophilized before the pre-modification with BSA by adding 1 mL 0.1 M NaOH and 1 mL 0.1 M Na_3PO_4 to 100 mg $CaCO_3$ in 10 mL distilled water and sonicating the mixture for 1 min.

In a cylindrical vessel, 1.4 mL oil (toluene, Miglyol or mint oil) was layered over 2.1 mL of a BSA modified NP suspension. The used ratio of aqueous/organic phase was 3:2. A high-intensity ultrasonic horn with a tip diameter of 3 mm was placed at the oil-water interface. To maintain the temperature below 30°C during ultrasonication, the vessel was positioned in an ice bath. The systems were sonicated for 3 minutes, except for the Ludox Cl samples that were sonicated for 1 min, at an acoustic power of ~ 200 W cm^{-2}. Simultaneously, the systems were mixed with a magnetic stirrer.

4.4. Fluorescent Labelling/ Modification of composite Protein Microcapsules

Fluorescent labelling

FITC was dissolved in DMSO at a concentration of 1 mg/mL. 210 µL of the FITC solution was added to 3.5 mL emulsion containing the composite capsules. The resulting solution was mixed by manual shaking and stored over night at 4°C in the dark for reaction.

Modification with APTES, FITC and RITC

The Ludox Cl NPs were dispersed in 5 mL ethanol at a final concentration of 1 wt%. To remove residual water the solution was centrifuged at 10000 rpm and redispersed with an equal volume of ethanol. Subsequently, 0.167 mL of an ammonium hydroxide solution (30%) and 900 µL of

a 0.06 M 3-aminopropyltriethoxysilane (APTES) solution in ethanol were slowly added while the suspension was mixed with a magnetic stirrer. The mixture was continuously stirred over night (ca. 16 h). After further centrifugation and redispersing in ethanol, 60 µL of a 0.5 mg/mL FITC solution in DMSO was added and the mixture was stored at 4°C for 2 h. The suspension was centrifuged again and then redispersed with 2.5 mL BisTris buffer solution (0.02 M, pH = 7). Thereafter, 2.5 mL of a 5% rhodamine B isothiocyanate (RITC) labelled BSA solution was added, the mixture was once more centrifuged and redispersed with 2.5 mL BisTris. Finally, the synthesis of the oil loaded composite protein microcapsules was carried out as described in 4.3.

4.5. SDS-PAGE

The formation of intermolecular disulfide bridges should lead to covalently bonded oligomers that can be verified by their size and should be cleaved by reducing agents. Thus, the samples were analyzed by reducing and non-reducing sodium dodecylsulfate polyacrylamide gel electrophoresis (SDS-PAGE). The sample of empty capsules as well as one of pristine BSA as control were mixed with non-reducing buffer (ROTILoad 2, Carl Roth) with or without addition of DTT (100 mM) and separated using a gradient gel (4 - 15 %, Bio-Rad) at constant current of 25 mA. Each lane of SDS-PAGE assay was loaded with the same amount (13.5 µg) of abovementioned samples. Afterwards, the gel was stained with Coomassie Brilliant Blue R-250 (Applichem). A protein ladder (ROTIMark TRICOLOR XTRA, Roth) was used to determine the size of the samples.

4.6. Measurements of Interfacial Tension on the oil/water Interface

All IFT measurements were carried out using the pendant drop method described in the chapter 3 “Materials and Methods” in section 8. The droplet consisted of the aqueous BSA solution while the surrounding phase consisted of oil. BSA was dissolved in distilled water and the used BSA concentrations were 0.5 % w/v and 5% w/v. The used oil phases were toluene, Miglyol 812 and mint oil. The measurements were performed until the droplet ripped off due to the decreasing surface tension or until a stable plateau was obtained. Moreover, all measurements were repeated three times.

5. Protein Microcapsules

The preparation of protein-based microcapsules filled with water-insoluble liquids using high-intensity ultrasound is well known but the underlying chemical processes remained elusive. The synthesis of the protein microcapsules is a complex process and for a better understanding of the formation, the microcapsules were characterized with various methods. This chapter will present information on the conformational complexity of BSA at interfaces and the examination of the mechanism of the microcapsules' formation. The results of this chapter were partly published.[9]

5.1. Adsorption Kinetics of BSA at oil/water interfaces

One of the frequently used techniques for the determination of the interfacial tension (IFT) of protein-stabilized liquid/liquid systems are the IFT measurements by pendant drop tensiometry. In the Method chapter 3.8. a description of the measurements can be found. The obtained data describe the time-dependent IFT, give information on protein properties at the liquid/liquid interface and an understanding of adsorption processes at the interface can be provided. The theoretical background of the IFT can be found in the Theory chapter 2.1.

This chapter presents the pendant drop experiments of BSA at the oil/water interface with different oils. The IFTs of all tested oils were measured against distilled water, a 0.5% w/v and a 5% w/v BSA solution.

BSA is a surface active protein and its amphiphilic properties are caused by a hydrophobic core containing most of the nonpolar amino acids and a hydrophilic surface where mainly the polar amino acids are located. In an oil/water system, BSA unfolds and rearranges at the hydrophobic/hydrophilic interface.

In Figure 5.1 the reduction of the IFT over time caused by BSA is shown for toluene, Miglyol and mint oil. Beverung et al. described three regimes for the protein adsorption at the oil/water interface.[49] Regime I, the induction period, cannot be identified in the diagrams because it only occurs for low concentrated proteins.

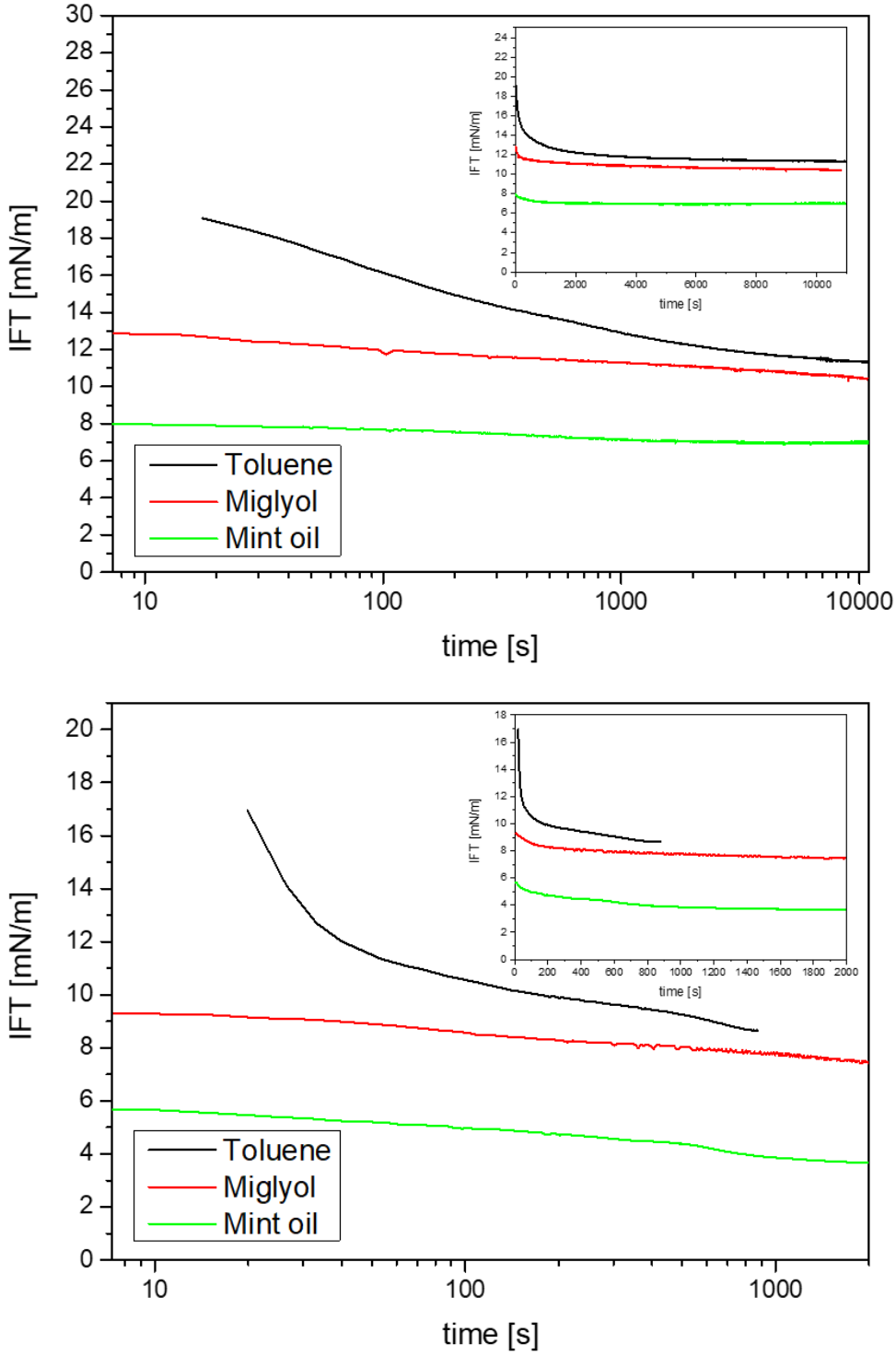

Figure 5.1 Interfacial tensions of toluene, Miglyol and mint oil against a 0.5% (top) and a 5% BSA solution (bottom) as logarithmic plot with the linear plot in the inset.

In this regime, the diffusion of the protein molecules to the interface takes place and the adsorbed proteins begin to change their conformation to expose the hydrophobic residues of the core of the protein. In regime II, a sharp decrease of the IFT can be observed which indicates

an increase of protein concentration at the interface. The subsequent adsorption of additional protein molecules leads to a saturation of the interfacial protein monolayer. The relaxing of the adsorbed proteins from their rigid conformations results in an increase of contacts between the protein and the oil phase. Regime II can only be identified for toluene. Miglyol and mint oil start directly with regime III showing that BSA adsorbs faster at the interface of these oils in the first two regimes than at the interface of toluene. In the last regime, a slowdown of the decline of the IFT is shown and continues until a plateau is reached and the IFT is in an equilibrium state (γ_{eq}). The results are summarized in Table 5.1 and Table 5.2. The IFTs against distilled water are in reasonable agreement with the literature.

Table 5.1 List of IFTs in equilibrium state (γ_{eq}) of pendant drop measurements of toluene, Miglyol and mint oil against distilled water, 0.5% w/v and 5% w/v BSA. Superscripted notes are literature sources used for comparison.

	γ [mN/m]	***γ_{eq} [mN/m]***	
Oil	**H_2O**	**0.5% w/v BSA**	**5% w/v BSA**
Toluene	36 ± 2[194]	11.5 ± 0.2	8.4 ± 0.1
Miglyol	19.3 ± 0.6[195]	10.0 ± 0.3	7.03 ± 0.08
Mint oil	14.96 ± 0.02[196]	7.04 ± 0.09	4.0 ± 0.2

Table 5.2 List of equilibration times *t* of pendant drop measurements of toluene, Miglyol and mint oil against 0.5% w/v and 5% w/v BSA.

	t [s]	
Oil	**0.5% w/v BSA**	**5% w/v BSA**
Toluene	10.000	900
Miglyol	>10.000	2000
Mint oil	2000	1000

The time to reach the equilibrium state decreases with increasing protein concentration. At low bulk concentrations proteins adsorb slowly. Thus, the IFT decreases over a longer period of time. At higher concentrations the IFT decreases rapidly until it reaches a plateau, which depends on the bulk concentration. In the beginning of the adsorption process the protein molecules close to the interface adsorb at the surface layer. At low surface coverage they change their conformation and by intermolecular interactions they form mechanically stable surface

structures. More and more protein molecules enter the interface with increasing adsorption time, making it harder for the new adsorbing protein molecules to rearrange there as well. In comparison to the protein molecules adsorbed at low concentrations the interactions between those molecules are getting more complicated. The shift to lower adsorption times indicates that at higher concentrations a shorter time is needed to undergo those conformational changes.[197] For example, the IFT of toluene and a 0.5% w/v BSA solution needed 10.000 s to reach the equilibrium and with an increased BSA concentration (5% w/v) the equilibrium value of the IFT was reached much faster (900 s). This behaviour was also observed for Miglyol and mint oil. Moreover, Table 5.1 shows that the IFT values shift when different oils are used. The BSA-stabilized mint oil/water interface has the lowest interfacial tension compared to the other two oils.

5.2. Formation of Protein Microcapsules upon Ultrasound Treatment

It is widely accepted that the capsule formation is a result of two very fast subsequently occurring phenomena: emulsification and shell cross-linking.[20, 23-25] The ultrasonic treatment of a two-phase liquid system leads to the formation of oil-in-water (O/W) emulsion stabilized by protein molecules adsorbed at the interface of emulsion droplets. Additionally, the propagation of the ultrasound wave through a liquid medium produces acoustic cavitations, i.e. the formation, growth and collapse of bubbles. The collapse is a very fast adiabatic process and yields highly reactive radicals[23, 26, 27] like superoxide. Suslick et al. proposed that the superoxide radicals cause the reaction between thiol groups in cysteines, which are present in BSA and that the protein capsule shells are held together by cross-linking through interprotein disulfide linkages arising from this oxidation of cysteine. However, the BSA molecule possesses only one thiol group enabling solely the formation of dimers but not a cross-linked network.

This inconsistency can be resolved by taking into account the results of Zhang and coworkers, who investigated the effect of ultrasound on the thiol groups and disulfide bonds of wheat gluten.[198] According to their findings, the ultrasound treatment can dynamically change the amount of thiol groups and disulfide bonds in the protein. After a few minutes of ultrasound treatment, the content of thiol groups was rapidly increased due to the sonochemical reduction of disulfide bonds and reached the value up to three times the initial amount. On the contrary, the content of disulfide bonds was quickly decreased up to 20% and then fluctuated within the same range. Assuming the similar effects in the case of BSA we can suggest that the cross-

linking mechanism leading to the formation of a stable capsule shell is based on the rearrangement of disulfide bonds upon ultrasonication. Since the native BSA molecule contains 17 intramolecular disulfide bonds, it is reasonable to assume that ultrasonically induced reductive cleavage of approx. 20% of them should yield 3 to 4 thiol groups in addition to the single thiol group in the pristine BSA. These groups can be then easily oxidized by the superoxide radicals leading to the formation of new intermolecular disulfide bonds and a cross-linked network. The rearrangement of intramolecular disulfide bonds into intermolecular ones can explain how BSA with only one oxidizable native thiol group can be cross-linked and form the shell of the microcapsules.

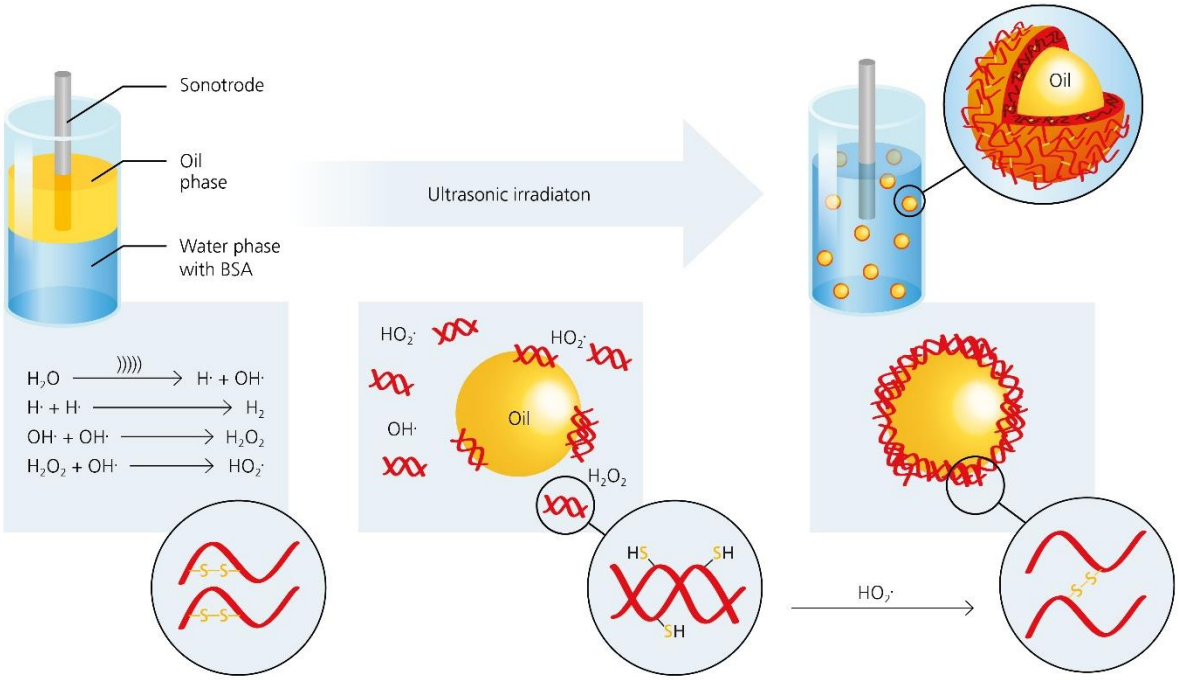

Figure 5.2 Synthesis scheme of oil loaded BSA microcapsules.

Figure 5.2 displays the mechanism of the synthesis of oil loaded BSA microcapsules. The synthesis is described in detail in chapter 4.1. The obtained microcapsules exhibit a spherical morphology and have protein shells with the average thickness of 10 nm (Figure 5.3 A). The surface of the capsule shell is rather rough but this appearance could also be caused by the cryo SEM sample preparation. Figure 5.3 B shows the toluene-loaded capsules with fluorescently labelled shells after one-week storage at standard laboratory conditions.

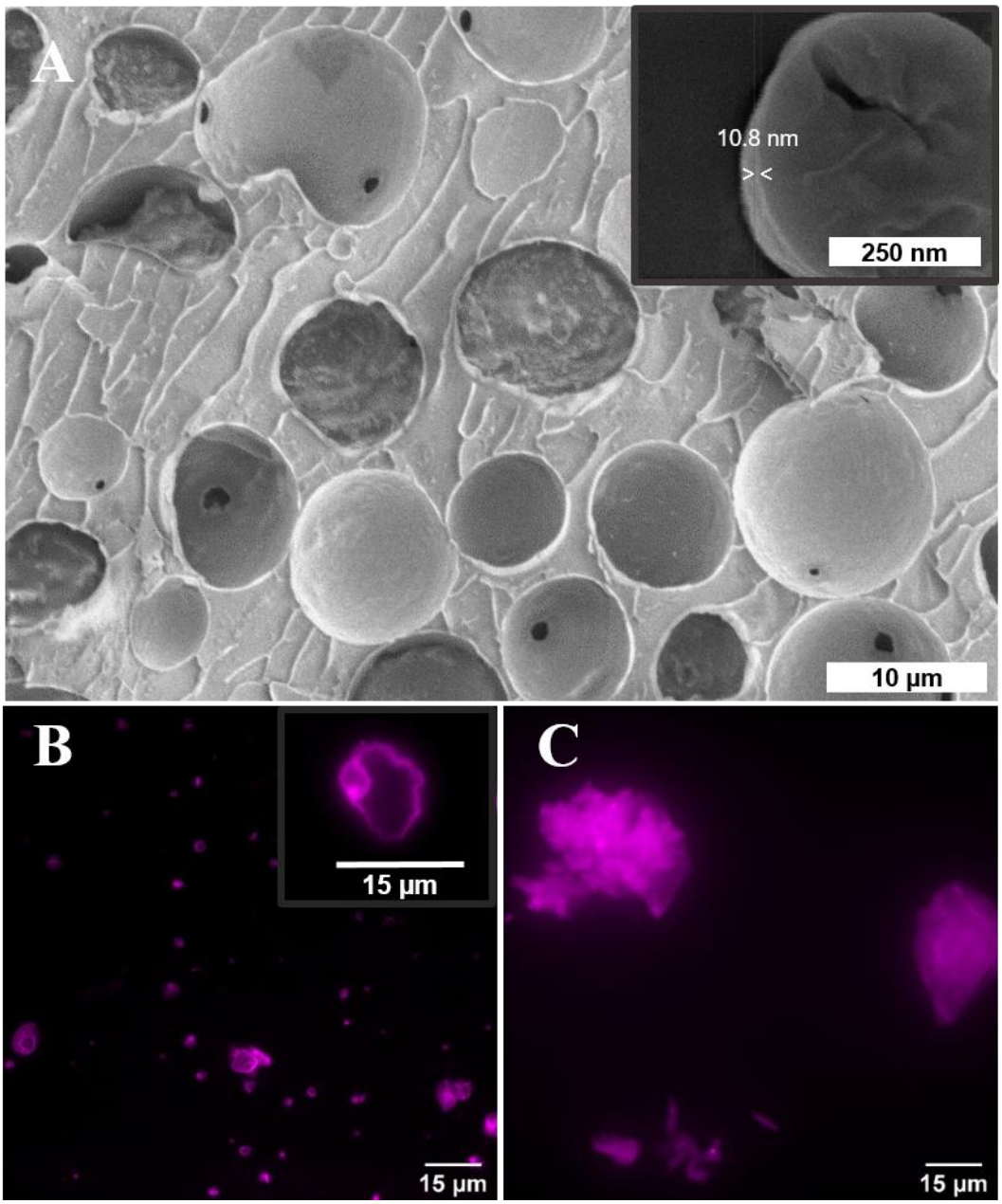

Figure 5.3 Cryo-SEM image of protein microcapsules loaded with toluene. Enlarged image of the cross section of a microcapsule and measurement of shell thickness is presented in the inset (A); fluorescence microscopy images of collapsed RITC labelled BSA microcapsules after one week aging, prepared by sonication (B) and by means of vortex mixer (C).

The capsule cores made of volatile toluene were evaporated and only the thin protein-based capsule shells and shell fragments remained. Clearly different results were obtained for protein stabilized emulsion droplets prepared by use of a vortex mixer (IKASONIC U50 control, IKA Werke Germany) (Figure 5.3 C). After a week, only residual protein debris with wide variability of shapes were observed without any evidences of empty capsule shells or their fragments.

This essentially lower stability of the protein stabilized emulsion generated by vortex suggests that even a vigorous shaking of toluene with an aqueous protein solution still does not possesses an sufficient energy to induce permanent covalent cross-linking of the capsule protein shells.

Laser diffraction was used to determine the size distribution of BSA microcapsules loaded with toluene, Miglyol or mint oil (see Figure 5.4). The results show, that all microcapsules are polydisperse. The capsules loaded with toluene show the broadest size distribution, while the Miglyol and mint oil loaded capsules exhibit a significantly narrower size distribution. The largest microcapsules with sizes of 1–3.5 µm were obtained when toluene was used as oil phase for the synthesis. Notably, there is also a fraction with very small capsules below 500 nm. However, the size influences the diffracted light intensity, i.e. the larger the capsules the higher the intensity of the diffracted light. For that reason, the intensities of those peaks are not a good measure for the concentration of the particle fraction. The sizes of the capsules loaded with Miglyol or mint oil are mainly in the submircometer range with 0.25–1 µm. These results are in good agreement with the IFT measurements discussed in section 5.1.1. The highest IFT was obtained with toluene, while the IFT values with Miglyol or mint oil were lower. This shows that the IFT influences the size of the microcapsules. As the IFT decreases smaller capsules sizes are obtained.

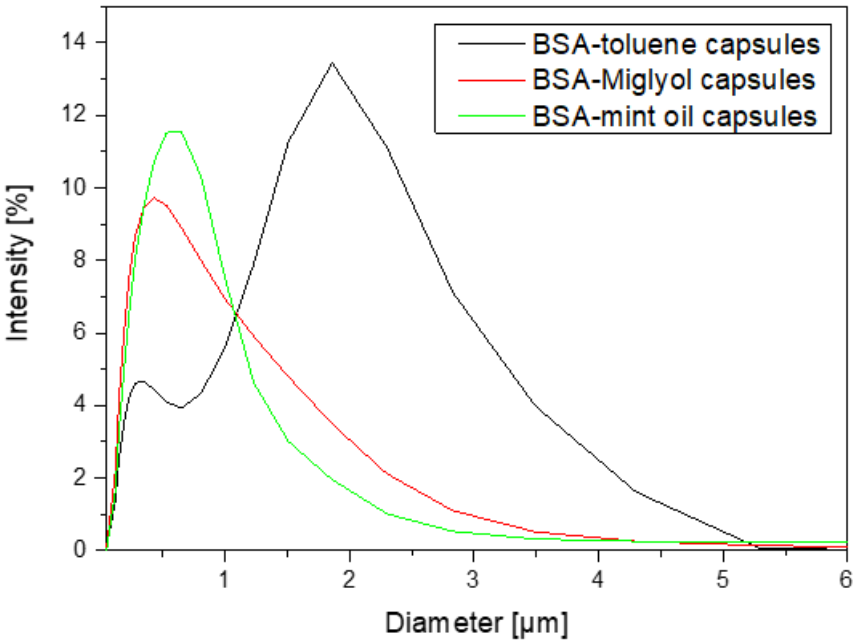

Figure 5.4 Results of laser diffraction measurements for toluene, Miglyol and mint oil loaded BSA capsules.

Furthermore, scanning force microscopy (SFM) was used to determine the wall thickness of empty cross-linked BSA microcapsules that were loaded with toluene. The result is displayed in Figure 5.5.

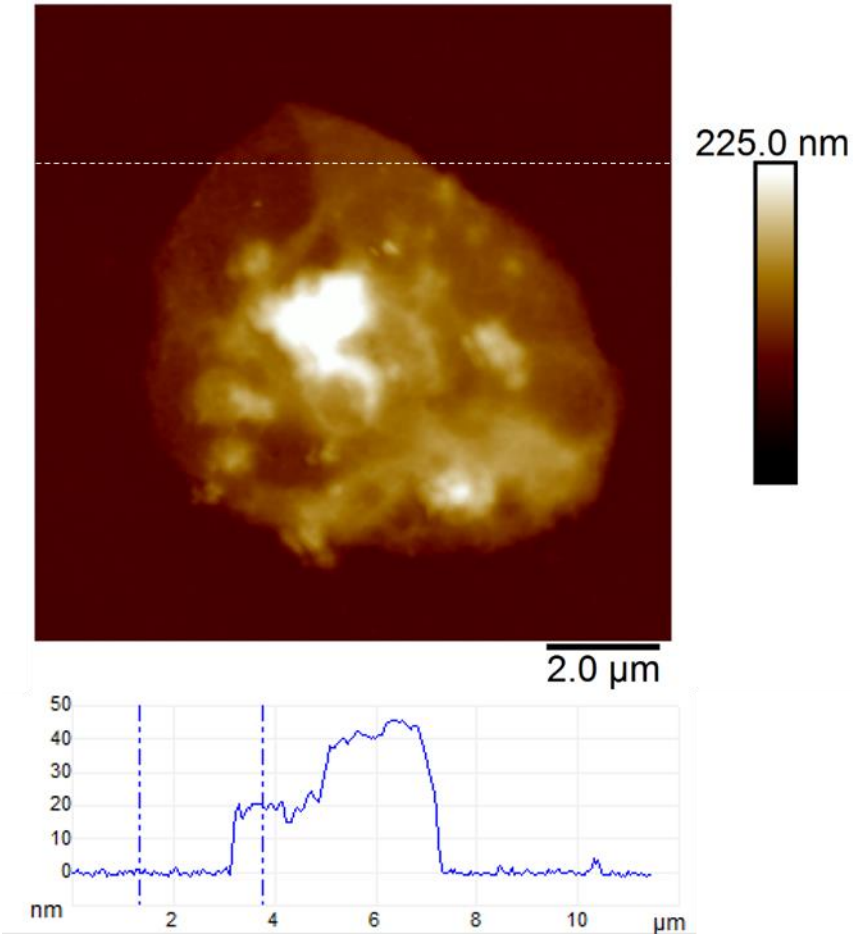

Figure 5.5 SFM height image and height profile diagram of an empty and dried BSA microcapsule

The SFM height image shows a microcapsule after one-week storage at standard laboratory conditions. The microcapsule emulsion was allowed to stay for 2 weeks only covered with Parafilm, the core of the capsules made of volatile toluene was evaporated and only the thin protein based capsule shells remained. This aqueous solution was deposited on a silicon wafer for further evaporation of the water, so that the sample could be examined with SFM. The microcapsules exhibit a spherical morphology and this round shape is still mainly intact after the process of evaporation and drying. The height profile diagram shows two different heights at approximately 20 nm and 40 nm. The height image illustrates that along the line where the height profile was measured the protein shell is folded on the top right causing two different

heights. In the area with a height of 20 nm the shell is not folded but taking into account that the dried flattened microcapsule still has two layers of the protein shell due to spherical shape in its original state it shows that the protein microcapsule has a shell thickness of 10 nm.

In the following chapter., the DLS measurement of BSA will show a diameter of approximately 5 nm demonstrating that the BSA microcapsules have a very thin protein shell. The information on the shell thickness of the protein microcapsules is used below in chapter 9 for the calculations of their mechanical properties.

5.3. Analysis of the cross-linking Mechanism

SDS-PAGE and DLS are both suitable methods to determine the molecular weight and the size of proteins, respectively. Additionally, the Raman spectroscopy, which is a non-destructive technique that only needs a small amount of the sample, is very sensitive to small changes in the chemical structure detecting subtle differences in the molecular environment. These techniques were used to examine changes in the BSA molecules after the ultrasound treatment.

SDS-PAGE

To examine the protein cross-linking in the microcapsule shell and to shed more light on the mechanism of their formation, SDS-PAGE was performed. Figure 5.6 shows the SDS-PAGE assay of empty BSA microcapsules and pristine BSA as control before and after the treatment with dithiothreitol (DTT). This reducing agent was used for the reductive cleavage of disulfide bonds within the protein as well as in the cross-linked proteinaceous shells. The empty BSA microcapsules in lanes 2 and 4 show numerous diffuse bands in the SDS-PAGE assay, especially at higher molecular weights in the range from 140 kDa to >310 kDa. This means that the microcapsule shells contain some proteinaceous components in this molecular weight range. However, distinct bands at approximately 55 kDa can also be observed, still indicating the presence of a significant amount of monomeric BSA in the shells, as follows from the comparison with the pristine BSA in lane 7. Here, in addition to the prominent main band at 55 kDa, only a slight smearing between 140 kDa and 240 kDa can be seen but no smear or diffuse bands above 240 kDa are visible. The observed appearance of the lane 7 for the pristine BSA is in good agreement with the data in the literature, both in well-known as well as in recently published works.[199-207] Notably also, the view of the pristine BSA's lane practically did

not depend on the protein concentration in a wide range (from 3 mg to 50 mg) of the concentrations studied, well coinciding with the formerly reported results.[200, 204, 207]

Especially in the parts of SDS-PAGE assays corresponding to higher M_w, neither essential changes nor an occurrence of additional bands, indicating the presence of high-molecular components were detected.

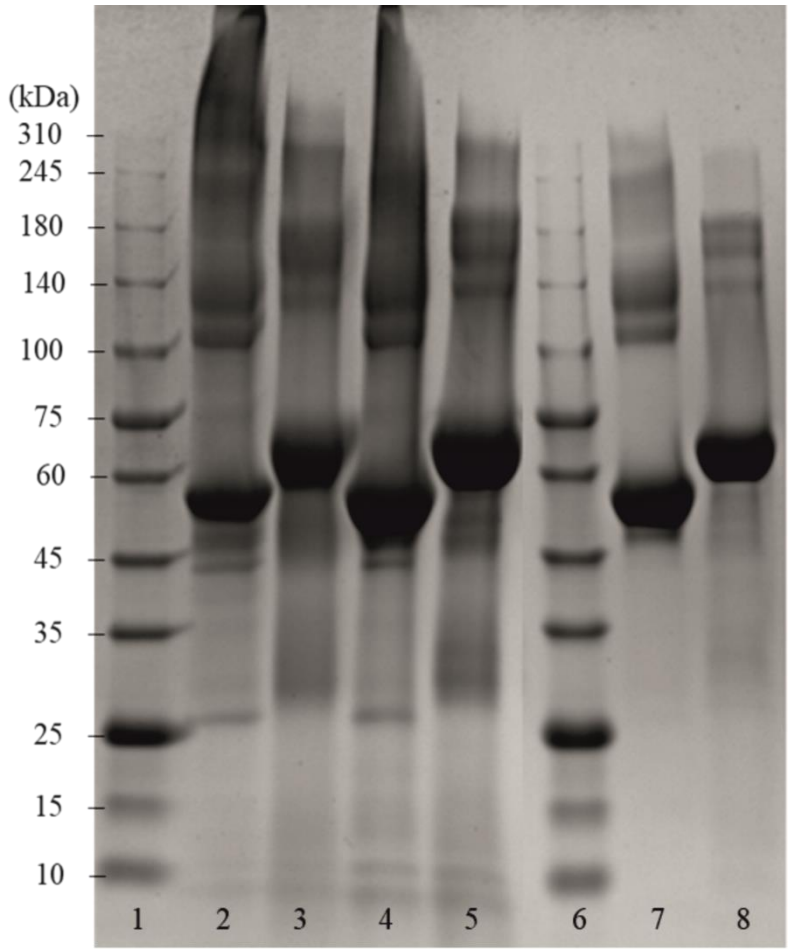

Figure 5.6 Coomassie-stained SDS-PAGE gel of empty BSA microcapsules, which were loaded with toluene, and pristine BSA. Lanes 1 and 6: reference marker; lane 2: empty capsules (dialyzed); lane 3: sample 2 treated with DTT; lane 4: empty capsules (washed with dropping funnel); lane 5: sample 4 treated with DTT; lane 7: pristine BSA; lane 8: pristine BSA treated with DTT.

Moreover, this property of BSA to maintain a well-resolved lane pattern over a broad concentration range has enabled its use as a standard protein in the SDS-PAGE assays, which utilize a BSA dilution series.[208]

In the case of BSA microcapsules reduced with DTT (lanes 3 and 5), the S–S bonds in the shells are cleaved and protein bands at smaller molecular weights were obtained showing an significantly lower smearing at M_w > 180 kDa as compared with lanes 2 and 4. However, for the pristine BSA treated with DTT in the same fashion (lane 8), there are no signs of molecules with molecular weights above 180 kDa. Under the assumption that DTT can cleave both inter- and intramolecular S–S bonds, the comparison of lanes 3, 5 and 8 allows the conclusion that the shells of protein capsules, although to an essential extent cross-linked via intermolecular disulfide bonds between BSA may also contain molecules bound together by other forces such as hydrogen bonds or hydrophobic interactions.

DLS

Dynamic light scattering (DLS) is known as a simple and quick experimental technique to identify and measure the size of various, especially globular proteins[207, 209] in a non-invasive manner. Since the intensity weighted (Z-average) peak will change its mean size and its width even at small changes in population sizes in the sample, DLS is proven to be an extremely sensitive method enabling clear comparisons between populations existing in samples and identification of samples where essential dimerization, oligomerization or aggregation[210] are happening. Therefore, to verify the SDS-PAGE findings described before DLS measurements were carried out for samples of pristine BSA, empty BSA capsules and BSA chemically cross-linked with glutaraldehyde (GA). The corresponding results are presented in Figure 5.7.

As one can see, the DLS spectrum of the pristine BSA displays only one peak around 6 nm, which correlates well with the hydrodynamic diameter of monomeric BSA.[207, 211-213] In contrast to this spectrum, the DLS spectrum for ultrasonically cross-linked BSA demonstrates two very distinct peaks; one – in the same size range as for the pristine BSA and the second one – at around 130 nm. The first of these two peaks corresponds to the abovementioned BSA monomers. The second one can be attributed to the cross-linked BSA oligomers occurred due to ultrasound treatment. The DLS spectrum for the chemically cross-linked BSA only displays a single peak at approximately 80 nm, which reflects the presence of BSA in this sample practically solely in the oligomeric form resulted from chemical cross-linking.

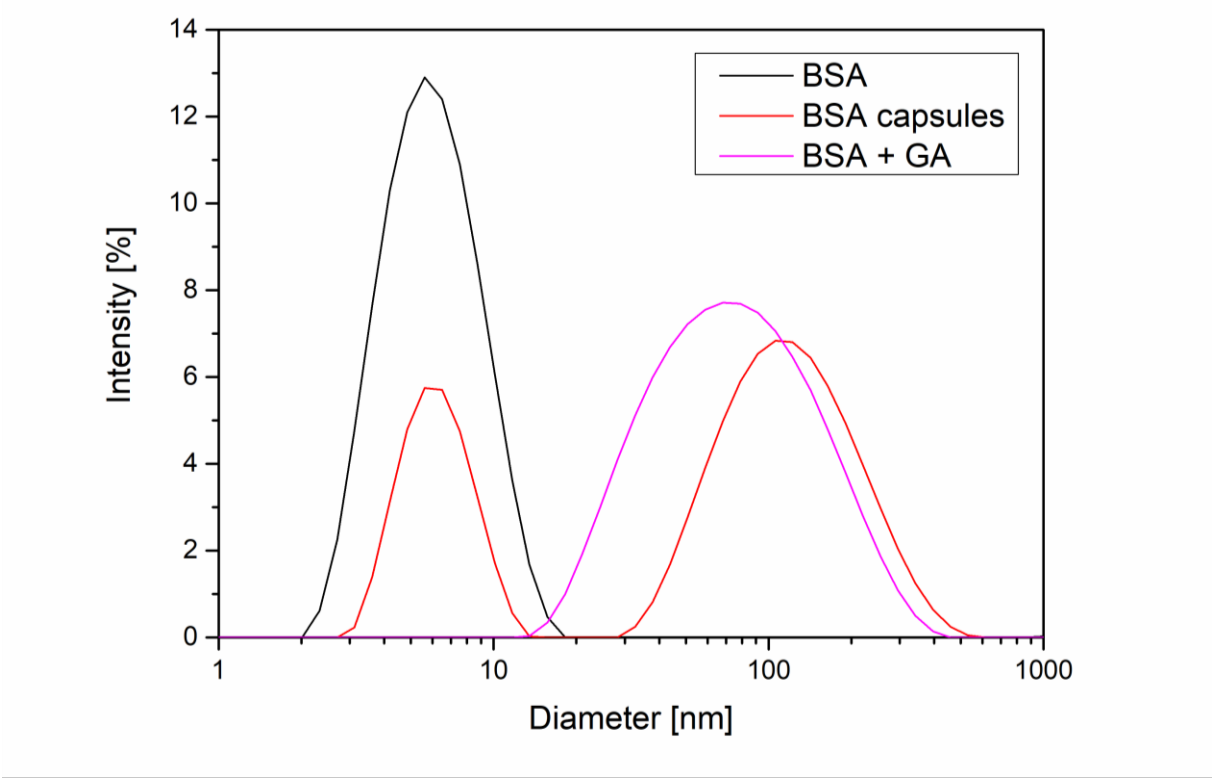

Figure 5.7 Results of DLS measurements for pristine monomeric BSA, empty BSA capsules and BSA chemically cross-linked with glutaraldehyde (GA).

This set of results proves undoubtedly the formation of the BSA oligomers caused by sonication. In addition, a well-pronounced peak in the lower nanometer range for ultrasonically treated BSA indicates that monomeric BSA is still present in significant amounts. Taking into account the relative sizes of peaks for both monomeric and oligomeric fractions of BSA in this sample, one can estimate[210] the amount of latter as high as several mol%. On the other hand, the low-molecular weight oligomers whose presence in sonicated samples can be inferred from SDS-PAGE data, are probably either too small or form too minor fractions to cause additional peaks in the DLS spectrum. Moreover, the application of the empirical equation between the size and molecular weight of globular proteins[214] yields an approximate molecular weight of oligomeric BSA of many millions of Da.

Raman Spectroscopy

To verify the findings of the SDS PAGE and the DLS measurements described before and to understand how the capsule formation affects disulfide bonds in BSA, Raman measurements

were performed for pristine BSA, toluene, dried BSA microcapsules and also for BSA and dried BSA microcapsules that were treated with DTT (see Figure 5.8).

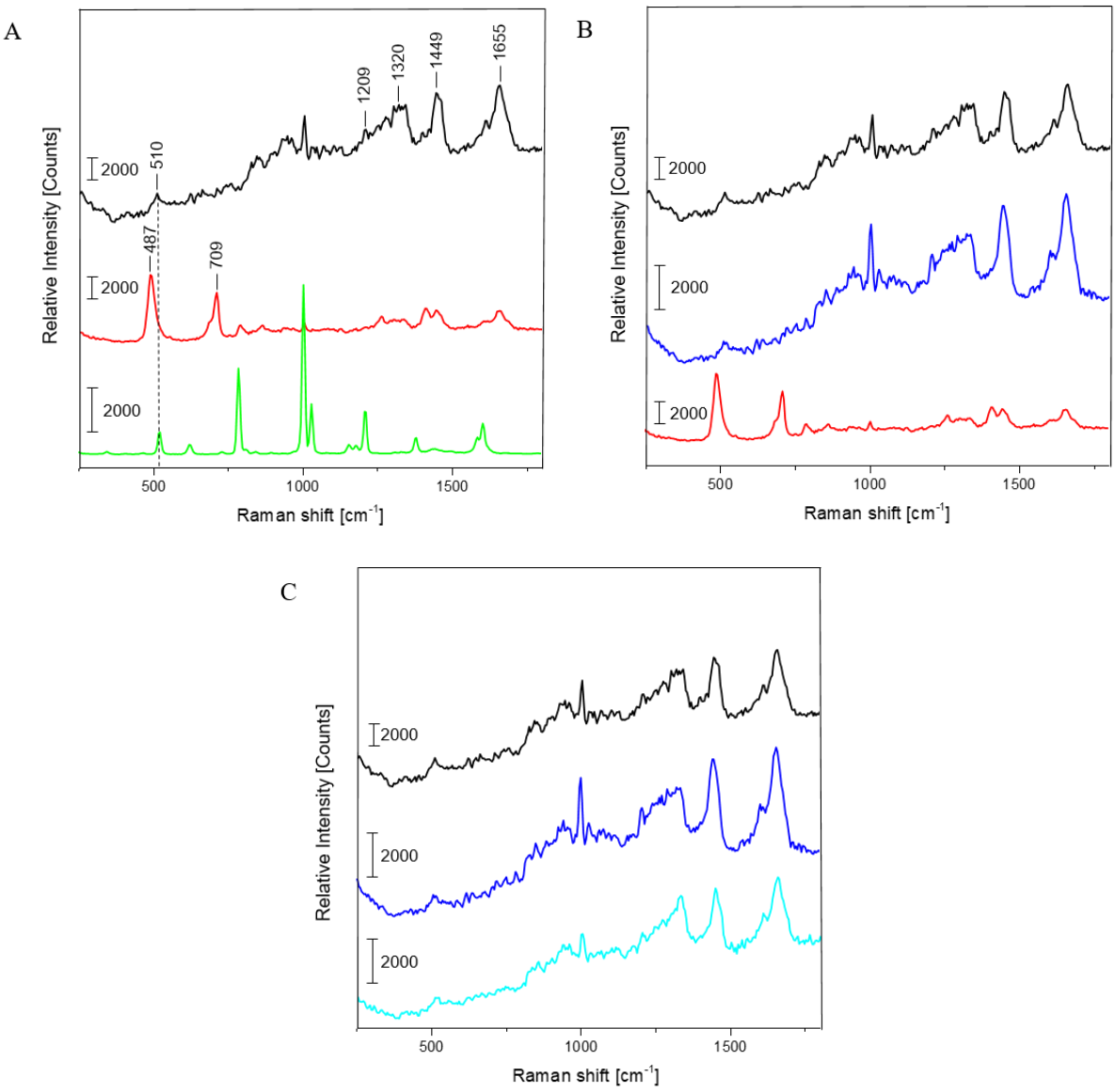

Figure 5.8 Raman spectra for: (A) pristine BSA (black), dried BSA-toluene-capsules (red), toluene (green), (B) capsules treated with DTT (blue) and (C) pristine BSA treated with DTT (light blue). Data acquisition conditions: excitation wavelength = 488 nm; laser power density = 3.7×10^4 W/cm^2.

Raman spectroscopy is sufficiently sensitive to detect and resolve the protein conformational changes on the basis of spectral changes in the low frequency range,[215] in contrast to FTIR spectroscopy, which can be used to monitor changes in the three-dimensional structure of proteins as it was successfully done by Silva et al.[33] The FTIR results and simulations presented in their paper substantiate that the capsule formation and their following stabilization can be

caused by the spatial rearrangement of protein molecules at the oil/water interface upon ultrasound treatment and by following hydrophobic interactions of corresponding moieties in the protein molecules with changed conformation. With that, the presence of cysteine groups is not required for the formation of a stable capsule shell.[33, 34] On the other hand, the mechanism involving the ultrasonically induced covalent cross-linking of BSA molecules in the capsule shell via intermolecular S–S bridges formation is nowhere controverted or denied in the paper of Silva et al. and in other publications of the Cavaco-Paulo's group.[33, 34] FTIR used therein as a main analytical tool is simply not sensitive enough for undoubtful confirmation or refutation of this phenomenon.[215]

Thus, Cavaco-Paulo and co-authors did not exclude the mechanism of covalent cross-linking between proteins in capsules via disulfide bonding but admitted such a possibility along with other physically or physicochemically driven mechanisms of capsule stabilization. These authors have also at no point claimed that this mechanism is a major reason for proteinaceous capsule formation; on the contrary, they suggested the plurality of various mechanisms leading to the formation of protein capsules:[34] "the possibility to form protein capsules from proteins like silk fibroin and cysteine-free peptides indicates the presence of further driving forces in addition to covalent cross-linking, namely hydrophobic, electrostatic interactions and enhanced mass transport, induced by ultrasound in liquid media".

Figure 5.8 A shows the Raman spectra of BSA, toluene and dried BSA-toluene capsules. The major bands that appear in the Raman spectrum of BSA are the amide I (~1655 cm^{-1}), CH_2 and CH_3 bending (~1449 cm^{-1}), amide III (~1200–1300 cm^{-1}) and S–S stretching vibration (~510 cm^{-1}).

The amide I band around 1650 cm^{-1} along with the broad amide III band around 1300 cm^{-1} show that the secondary structure of BSA is mainly in α-helix form.[216, 217] The peak at 510 cm^{-1} refers to the disulfide bonds of the cystine in the pristine BSA. In general, the S–S stretching vibration can appear in the 450–550 cm^{-1} range depending on the surrounding molecular structure, which makes this part of Raman spectra useful for the characterization of structural changes in proteins. Nonetheless, the interpretation of the disulfide peak position is not simple since several competing models have been proposed explaining the correlation between the peak wavenumber position and conformation of the molecule containing the corresponding bond. One model proposes that the wavenumber position of the S–S stretching vibration is dependent on the torsional angles in the Cα–Cβ–S–S–Cβ′–Cα′ conformation.[218, 219] In this instance, the peak position of the S–S stretching vibration should appear at 510 cm^{-1} for the

lowest energy *gauche–gauche–gauche* (*g–g–g*) conformation, at 525 cm^{-1} for the higher energy *gauche–gauche– trans* (*g–g–t*) conformation and at 540 cm^{-1} for the highest energy *trans–gauche–trans* (*t–g–t*) conformation (see Figure 5.9).

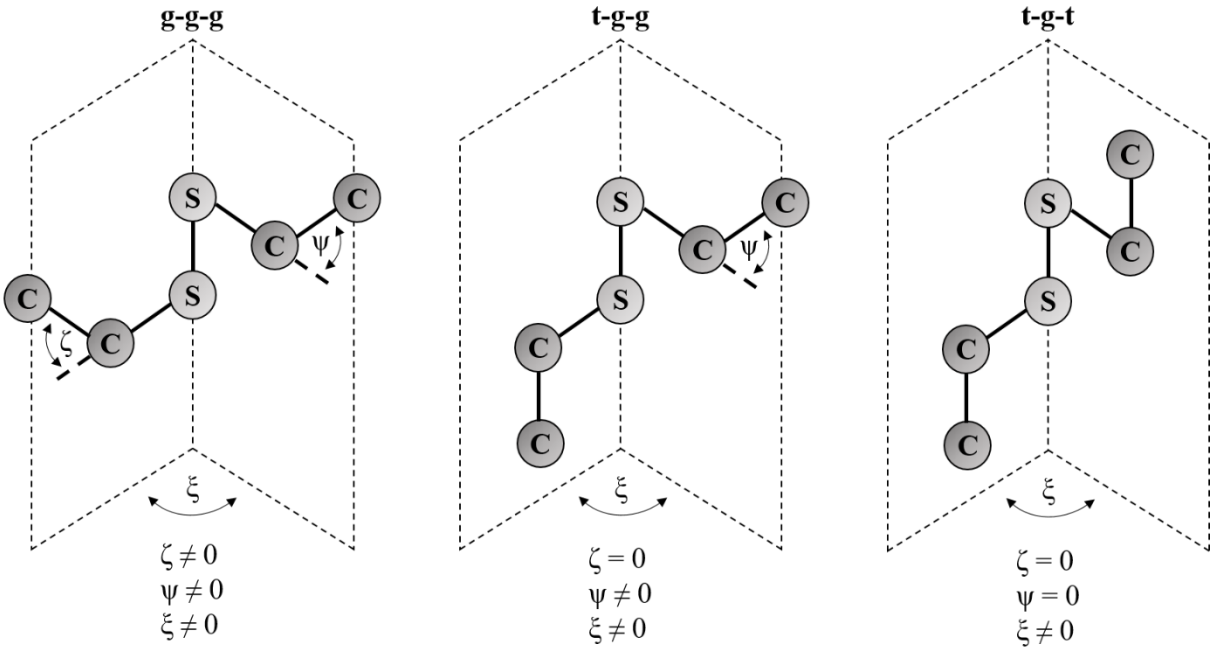

Figure 5.9 Schematic representation of the three conformations of disulfide bonds.[220]

Accordingly, the disulfide bonds in BSA have a *g–g–g* conformation. However, this theory does not explain the shift of S–S stretching vibration to wavenumbers below 510 cm^{-1} as can be seen in the Raman spectrum of the dried BSA–toluene capsules at 487 cm^{-1} (Figure 5.8 A and B, red spectra). This band also cannot be attributed to traces of toluene as follows from its Raman spectrum (Figure 5.8 A, green spectrum). In another approach, the Raman shift of the S–S stretching vibration is dependent on the dihedral angle between the planes containing the Cβ–S and the S–Cβ′ bonds of the Cα–Cβ–S–S–Cβ′–Cα′ group, respectively.[221-223] Disulfide bonds with an S–S stretching vibration with a value near 510 cm^{-1} should have a Cβ–S–S–Cβ′ dihedral angle of ±90°.[224] Although the mostly observed S–S stretching vibrations exist between 500 and 540 cm^{-1}, the strained disulfide groups with dihedral angles less than ±65° are also possible.

Biswas and coworkers observed a peak at 486 cm^{-1} while investigating the surfactant protein B (dSP-B1–25) with Raman spectroscopy.[224] This protein is a homodimer with three intramolecular disulfide bonds and one intermolecular disulfide bridge.

On the basis of several interpretations proposed by these authors for the spectrum of protein B, the following explanation for the system in this work is suggested: the peak position at 487 cm^{-1} (Figure 5.8 A and B, red spectra) indicates that there is a highly strained but stable disulfide bond conformation with a dihedral angle in the range of ±10° due to the crosslinking of the neighboring protein molecules in the capsule shell. This strain could also lead to the increase of the intensity of this peak as can be observed in the spectrum of dried capsules in Figure 5.8 A and B. Relative amounts of intramolecular disulfide bonds of BSA and intermolecular disulfide bonds occurred due to the ultrasound treatment can be compared as follows. Although the intensity of the same peaks in the different spectra cannot be compared quantitatively, it is possible to make an inherent comparison of different peaks in the same spectrum (inherent normalization of a spectrum)[225] and then recognize these results when consider different spectra. In accordance with this, the relative intensity of the disulfide band at 510 cm^{-1} in the spectrum of the pristine BSA is quite low compared to the intensity of the amide I peak at 1655 cm^{-1} (black spectrum in the Figure 5.8 A).

On the other hand, the relative intensity of the band for the intermolecular disulfide bridges in the capsule shell (487 cm^{-1}) is higher than the intensity of the amide I peak at 1655 cm^{-1} in the sample containing only BSA capsules (red spectra in the Figure 5.8 A and B). This qualitative comparison indicates that the relative intensity of the band for the residual intramolecular S–S bridges at 510 cm^{-1} in the spectrum for BSA capsules should be lower than the band corresponding to intermolecular S–S bridges in the capsule shell at 487 cm^{-1}, i.e. the contribution of intermolecular S–S bridges to the resulting Raman spectrum in the low frequency range is prevalent and the results suggest that a significant amount of intramolecular bridges is converted into intermolecular ones.

The exploration of the residual intramolecular S-S bridges in the same Raman spectrum is however complicated by the higher intensity of the peak for intermolecular ones - the right shoulder of the stronger peak at 487 cm^{-1} covers the weak residual signal at 510 cm^{-1} almost completely. Furthermore, the Raman spectrum of the capsules shows an additional peak at 709 cm^{-1}, which refers to the C–S stretching vibration of the N–C–C–S–S moieties with N and S–S in the trans-conformation.[224] This is another hint for the intermolecular cross-linking in the shells causing the conformational changes in the BSA molecules after the capsule formation.

Additionally, the capsules spectrum shows a band around 1450 cm^{-1}, which is assigned to the CH_2 and CH_3 bending vibration, and one around 1410 cm^{-1} corresponding to the C=O stretching vibration of dissociated carboxyl groups.[226] On the contrary, this band appears only as a shoulder in the spectra of the pristine BSA and DTT treated capsules. The observed difference could be explained by the reduction of the band intensity at 1450 cm^{-1} due to sterical constraints in the local surrounding of CH_2 moieties caused by the intermolecular crosslinking at the capsule formation. Thus, the C=O stretching vibration around 1410 cm^{-1} becomes visible as an individual peak in the capsules' spectrum.

Figure 5.8 B shows the Raman spectrum of the BSA capsules after the treatment with DTT and subsequent dialysis in comparison to the spectra of the capsules before the cleavage of the disulfide bonds and of the pristine BSA. The two additional peaks at 487 cm^{-1} and 709 cm^{-1} that are typical for the capsules spectrum are not present after the reaction with DTT. Furthermore, the peaks of the cleaved capsules correlate with the peaks of pristine BSA. This demonstrates that after the cleavage of the S–S bonds initial structure of BSA was regained. The effect of DTT to pristine BSA (Figure 5.8 C) were also investigated. The Raman spectra of BSA before and after the treatment with DTT are nearly identical, which allows the assumption that after removal of the DTT by dialysis, the thiol groups of the BSA molecules could be easily rearranged back to intramolecular S–S bonds, e.g. by an oxidative action of oxygen from the air.

The detailed analysis of Raman spectra for pristine BSA, empty BSA capsules and the samples cleaved with DTT brings additional evidences for the formation of intermolecular S–S bonds in the BSA composing the capsule shells and therefore confirms the findings of the SDS-PAGE and DLS measurements discussed before.

6. Characterization of HAP Nanoparticles

Different nanoparticles (NPs) will be used for the formation of composite microcapsules. However, in contrast to the other NPs, which will be introduced in the next chapter, the HAP NPs were synthesized and not purchased. The commercial HAP NPs available as dispersion exhibit a needle-like shape that might be less suitable to form a capsule shell than spherical NPs. Furthermore, those NPs are typically stabilized with different stabilizers (like citric acid or phosphoric acid etc.), which shift their isoelectric point (IEP) to an acidic pH range. This would complicate the adsorption of BSA on the surface of the HAP NPs, which will be discussed in detail in section 6.5. Thus, the commercial HAP NPs are not suitable as shell material for composite BSA microcapsules. As a consequence, the HAP NPs were synthesized and needed to be characterized to ensure that HAP with suitable properties was generated.

In the Theory chapter 2.3.1. Hydroxyapatite (HAP) was introduced belonging to the biominerals that occur in form of bones and teeth in the human body. Thus, as HAP being biocompatible, its production is very interesting for implants and capsules carrying drugs. Moreover, the reactants needed for the HAP synthesis are available at a reasonable price and non-toxic. In the following sections, the characterization of the synthesized HAP nanoparticles using different methods will be discussed.

6.1. XRD

XRD is the standard technique for the characterization of crystals. By use of XRD the NPs could be identified as hydroxyapatite by comparing the position of the diffraction peaks with the literature[6, 227] and the corresponding diffraction pattern is shown in Figure 6.1. The peaks appear broad and this broadening can arise from a small crystal size or a low degree of crystallinity.[228] Moreover, XRD is also a convenient method to determine the size of single crystal nanoparticles. With the Scherrer equation,[229] which relates the size of sub-micrometer crystals to the broadening of the peak in the diffraction pattern, a mean size of about 15 nm was calculated.

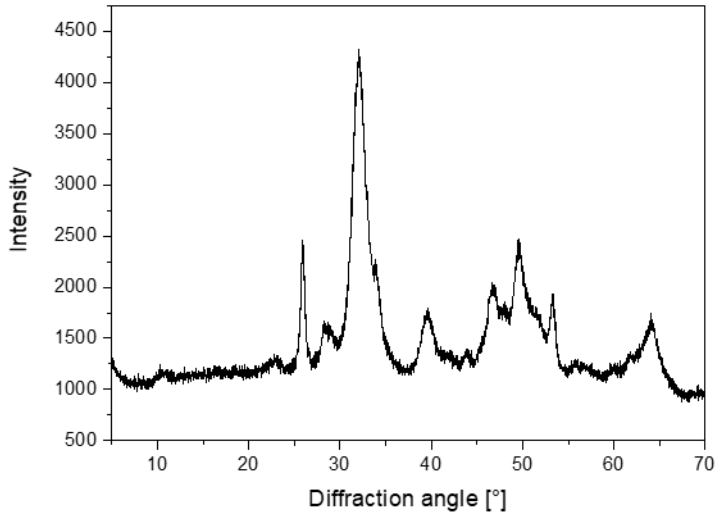

Figure 6.1 XRD pattern of HAP NP prepared by stirring.

6.2. Raman Spectroscopy

The Raman spectrum of HAP NP is shown in Figure 6.2 and it is in good accordance with the literature.[230, 231] All bands are assigned to the internal vibrational modes of the phosphate group. The symmetric stretching mode has a characteristic and very strong peak at 965 cm^{-1}. The band at 432 cm^{-1} is attributed to the bending mode, the band at 590 cm^{-1} is assigned to asymmetric bending mode, while the bands at 1048 cm^{-1} and 1071 cm^{-1} are corresponded to the asymmetric stretching mode.

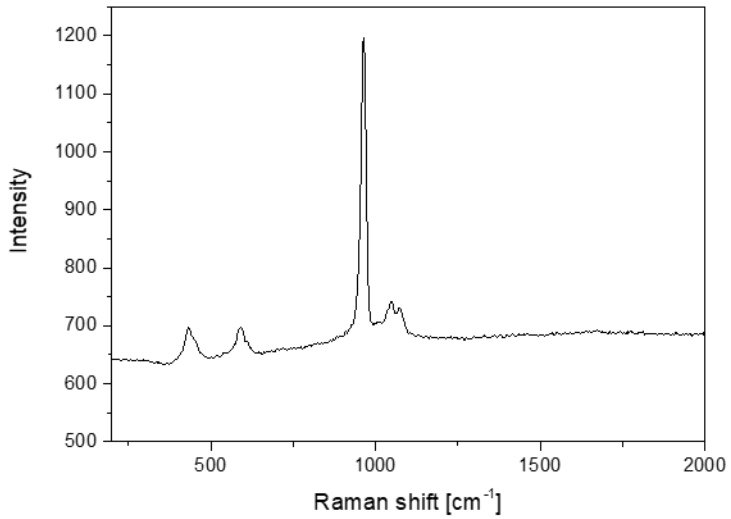

Figure 6.2 Raman spectrum for HAP NP.

6.3. SEM

The synthesis of the HAP NP was described in chapter 4.2. SEM was used to characterize the morphology and size of those NP that are shown in Figure 6.3. The particles displayed in Figure 6.3 A are in the lower nanometer range with an average particle width of 10 to 20 nm and a length of approximately 100 nm and have a needle-like shape. The particles synthesized by sonication (Figure 6.3 B) are also in the lower nanoscale with several tens of nanometer but have an irregular sphere shape.

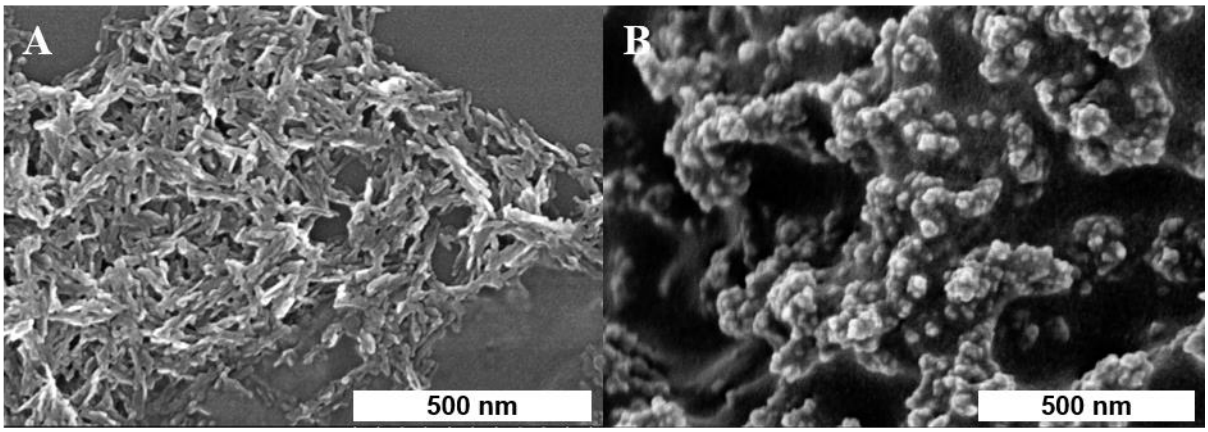

Figure 6.3 SEM image of synthesized HAP NP prepared by stirring (A) and sonication (B).

Both types of particles showed a tendency to agglomerate. As mentioned before due to the formation of bubbles during the ultrasonic irradiation that grew and collapse implosively transient hot spots with enormous temperatures are created. These temperature and pressure variations directly influence the synthesis of the HAP NP, including the particle size and its morphology. HAP NPs described in the literature that were also prepared by precipitation methods exhibit average particle sizes between 80 and 200 nm in length and between 20 and 40 nm in width.[227] The particle sizes of the HAP NP synthesized for this work are in the same range.

6.4. DLS

The particle size distribution of a HAP NP suspension measured with the Malvern Zetasizer Nano ZS is shown in Figure 6.4. The average particle size is about 100 nm. Nevertheless, DLS

is mostly used for the size characterization of spherical particles. The commercial devices prepared for spheres do not take into account the geometries of non-spherical particles and the contribution of the rotational diffusion, which can have important effects on the size determinations. However, the DLS measurement is in good agreement with the particle size shown in the SEM image (Figure 6.3 A).

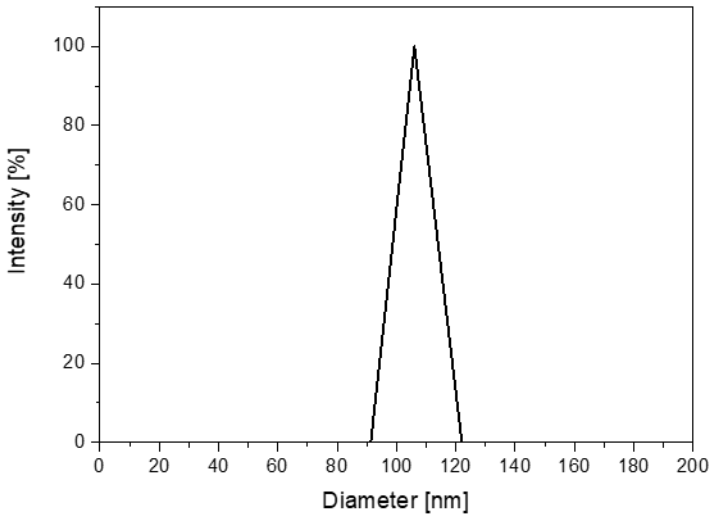

Figure 6.4 DLS measurement for HAP NP prepared by stirring.

6.5. Zeta potential

Figure 6.5 shows the pH dependence of the zeta potential of the synthesized HAP nanoparticles. The zeta potential measurements for HAP reported in the literature show that the isoelectric point (IEP) of HAP nanoparticles can vary depending on the preparation method but is usually in the pH range of 5.5–7.[232-235] The IEP of the NPs synthesized with the standard route (red) was observed close to a pH of 5.8. Similar zeta potential values were also measured by Kandori and coworkers.[236] To enable the electrostatic attraction between HAP and BSA, which has its IEP at a pH of 4.75, the IEP of HAP needed to be shifted to a higher pH. Furthermore, the increase of pH leads to the decrease of the pH-dependent solubility product of HAP.[68] The solubility of HAP NPs at a physiological pH of 7.4 is negligible.[237]

The HAP NPs were synthesized by adding a calcium nitrate solution to an equal volume of a diammonium hydrogen phosphate solution under moderate stirring. The synthesis is described in detail in chapter 4.2. Subsequently, the aqueous medium of the HAP suspension was replaced

with a 10 mM $Ca(NO_3)_2$ solution, the mixture was stirred for 4 h and subsequently dialyzed against distilled water over night (blue). In consequence of this treatment, the zeta potential values of the HAP nanoparticles increased and the IEP shifted to the pH 6.4. Synthesizing the HAP NPs without citric acid (light blue), increasing the concentration of $Ca(NO_3)_2$ to 20 mM and extending the stirring time to three days (magenta) led to a further shift of the IEP to pH = 7. This shift takes place due to the adsorption of the Ca^{2+} ions to the HAP NPs.

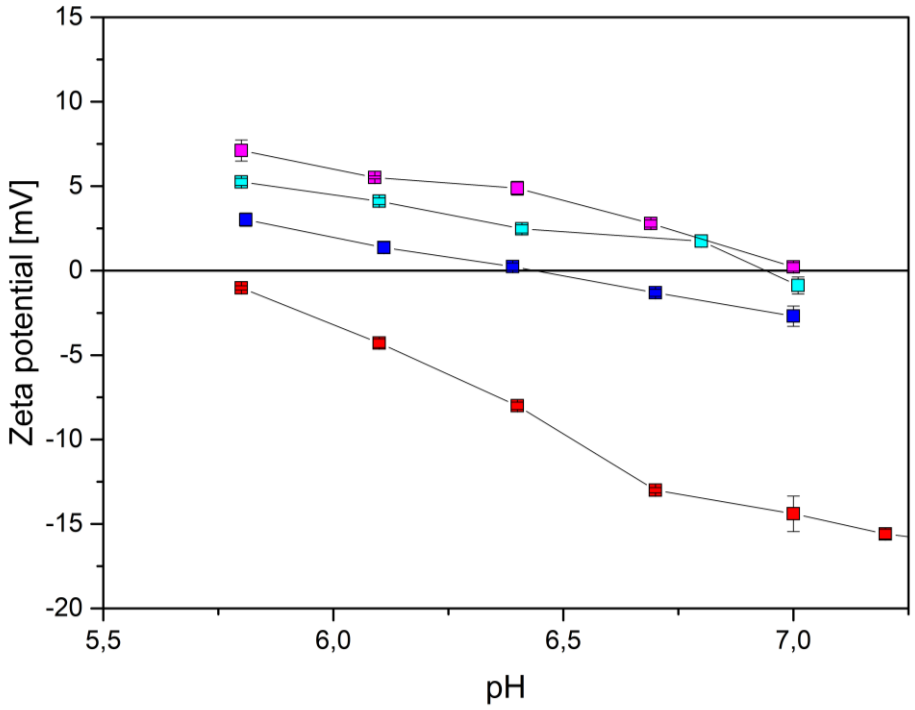

Figure 6.5 Zeta potential measurements of synthesized HAP nanoparticles at different pH values: HAP synthesized according to Jutz et al.[6] (red), HAP treated with 10 mM $Ca(NO_3)_2$ (blue), HAP (without citric acid) treated with 10 mM $Ca(NO_3)_2$ (light blue) and HAP (without citric acid) treated with 20 mM $Ca(NO_3)_2$ (magenta).

Thus, a positive zeta potential of +7.1 ± 0.6 mV at pH = 5.8 could be achieved and should facilitate the adsorption of BSA, which has a negative zeta potential at this pH value, on the surface of HAP NPs because of the electrostatic attraction. The HAP NPs that were treated with 20 mM $Ca(NO_3)_2$ for three days (magenta in Figure 6.5) were used for the synthesis of the composite microcapsules. The pH value of the BSA solution was adjusted to 5.8 before the addition of the HAP suspension to ensure optimal electrostatic attraction. This mixture was dialyzed against distilled water with a pH of 5.8 using a dialysis tube with a cutoff of 1000 kDa over night to remove free BSA. Subsequently, the toluene loaded microcapsules were synthesized via sonication as described in 4.3. The microcapsules were washed with distilled

water and after creaming, the emulsion was separated from the aqueous phase and dried for TGA. The results of this analysis, which will be discussed in the TGA section of the next chapter, showed that the adsorption of BSA on the surface of these HAP NPs was not successful.

7. Characterization of the modified Nanoparticles

The following chapter deals with the modification of various NPs with BSA and their characterization with different methods. Coating the NPs with BSA enables their ability to stabilize O/W emulsions and thereby the formation of composite protein-mineral microcapsules. HAP, Ludox Cl (aluminum oxide coated silica NPs), silica particles, whose surface was partially modified with DCDMS (71% of surface silanol groups remained intact) and called from now on as Si71 as well as calcium carbonate NPs, whose surface was modified with stearic acid, were chosen for the modification with BSA and further syntheses of composite microcapsules because of their biocompatibility and affordability.

7.1. TGA

The TGA measurements were used to determine the adsorption of BSA on the surface of various NPs and the composition of those modified particles. Figure 7.1 shows the TGA results for BSA, HAP and dried BSA-HAP-Toluene microcapsules.

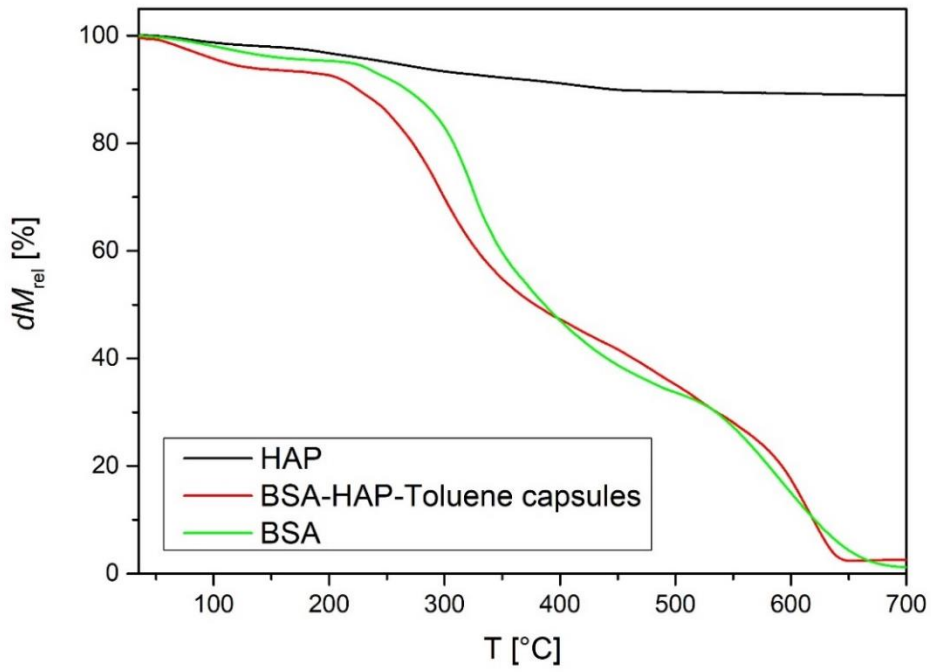

Figure 7.1 TGA measurements of HAP (black), BSA (green), and dried BSA-HAP-Toluene microcapsules (red) measured in air atmosphere.

The HAP NPs were treated with 20 mM $Ca(NO_3)_2$ for three days as described in section 6.5 and the synthesis was performed at pH 5.8 to ensure optimal electrostatic attraction.. The courses of the decomposition curves of BSA and the dried capsules are very similar including the low residual mass. This indicates that no HAP or only very small amounts are imbedded in the capsule shell.

The solubility and stability of calcium phosphates is strongly pH dependent and TGA and further experiments showed that the HAP NPs were not stable at pH 5.8. Furthermore, dialysis was not a suitable method to remove residual BSA molecules, as the removal was incomplete. Thus, the few BSA-modified HAP NPs were competing with the free BSA molecules to adsorb at the interface and since the NPs are larger, they probably move slower to the interface.

Synthesizing HAP NPs with an acceptable size and a suitable zeta potential to be imbedded in the shell of the protein microcapsules was difficult, because those characteristics are strongly dependent on the preparation method. For that reason, in the following chapters the focus was changed to the use of Ludox Cl, which are aluminum oxide coated silica NPs, for the synthesis of composite BSA microcapsules with different oils. Nevertheless, after changing the pH from 5.8 to 7 and the washing procedure from dialysis to centrifugation, the HAP NPs were used for the capsule formation as well.

This chapter will describe the successful adsorption of BSA on various NPs including HAP examined by TGA (Figure 7.2). The TGA curve of the pristine BSA is displayed in all TGA diagrams for better comparison. A three-step decomposition curve can be observed for the pristine BSA. The initial weight loss at 100°C is assigned to the dehydration of the sample. The weight loss of BSA started when the temperature rises above 200°C. The third step is starting at approximately 450°C and ends at 600°C. The total weight loss was 97.5 wt% demonstrating that BSA decomposes completely in this temperature range.

The black curve in Figure 7.2 A belongs to the synthesized HAP and it shows a weight loss of 11 wt% as the temperature was increased to 700°C because of the evaporation of the residue crystal water. The green curve of the BSA modified HAP NPs started with the degrading as pristine BSA at 200°C and it stopped decomposing at 600°C as well but with a weight loss of 75 wt%. Comparing the TGA curve of pristine BSA and HAP it is clear that the thermal decomposition of the amino acid residues of BSA and its peptide chains is responsible for this weight loss showing that the residual 25 wt% are attributed to HAP.

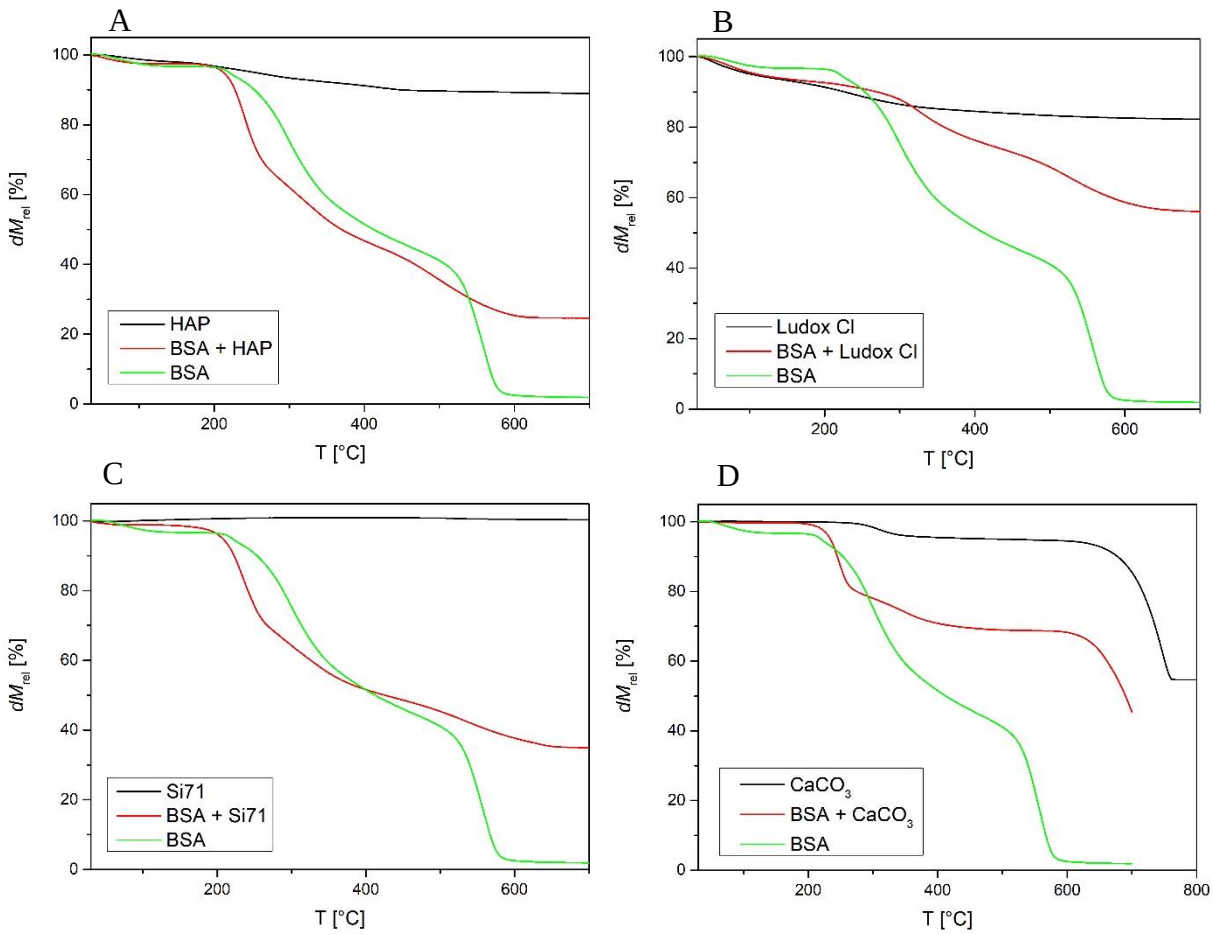

Figure 7.2 TGA measurements of BSA adsorbed on HAP (A), Ludox Cl (B), Si71 (C) and $CaCO_3$ (D) measured in air atmosphere.

A similar behavior has been observed for the other NPs. The Ludox Cl particles exhibit a weight loss of 18 wt % (Figure 7.2 B) which is in the same range as the weight loss of HAP, while the weight loss of the BSA modified Ludox Cl particles is 44 wt%. The amount of the residual Ludox Cl with 56 wt% is more than twice as high as the residual HAP with 25 wt%.

The TGA curves for the pristine and the BSA modified Si71 particles are shown in Figure 7.2 C. No weight loss was observed in the TGA curve of the pristine Si71 particles, whereas the BSA modified NPs have a weight loss of 65 wt% leaving 35 wt% as residual silica particles.

Figure 7.2 D displays the thermal decomposition of the $CaCO_3$ NPs, that were hydrophilized by sonication and the same particles additionally modified with BSA. The decomposition begins when the temperature rises above 600°C and ends at approximately 750°C with a weight loss of 45 wt%. It decomposes to calcium oxide and carbon dioxide.[238, 239] The BSA modified $CaCO_3$ NPs begin to decompose at 200°C slightly faster than the pristine BSA. At 600°C where

BSA is fully degraded and before the decomposition of the $CaCO_3$ NPs starts, the residual mass is 68 wt%. The TGA measurements showed that BSA adsorbed strongly on four different types of NPs and can be detected even after thorough washing process including multistep washing and subsequent centrifugation.

Notably, the adsorbed BSA decomposes faster than the pristine BSA. The TGA curve of the BSA modified Ludox Cl particles is the only sample where the adsorbed BSA decomposes slower than the pristine BSA, except from the beginning where the dehydration takes place. It is possible that this behavior is caused by the electrostatic attraction between BSA and Ludox Cl while the adsorption of BSA on the other NPs is driven by different interactions such as van der Waals forces, hydrogen bonding and hydrophobic interactions. This will be discussed in detail in the next section.

Moreover, the TGA curves show that the highest content of adsorbed BSA, which was amounted to 75 wt%, was found on the HAP NPs. The adsorption of BSA on HAP depends on the interaction of the anionic carboxyl group of the protein and the cationic calcium ions while the negative phosphate group follows a strong interaction with the positive amino group.[240, 241] The TGA measurements indicates that these interactions could be stronger than the hydrophobic interactions between Si71 or $CaCO_3$ and BSA and the electrostatic attraction between Ludox Cl and BSA.

7.2. Zeta Potential

The stability of a colloidal system is strongly depending on the interactions between particles and molecules. An excellent tool providing information of particle charges and electrostatic stabilization is the determination of the zeta potential (ZP) of those colloidal systems.

The ZP of BSA, the pristine and the modified NPs was determined using a Malvern Zetasizer Nano ZS. Figure 7.3 shows how the ZP of BSA, Ludox Cl and HAP changes at different pH values and the zeta potential values of pristine and BSA modified nanoparticles are listed in Table 7.1.

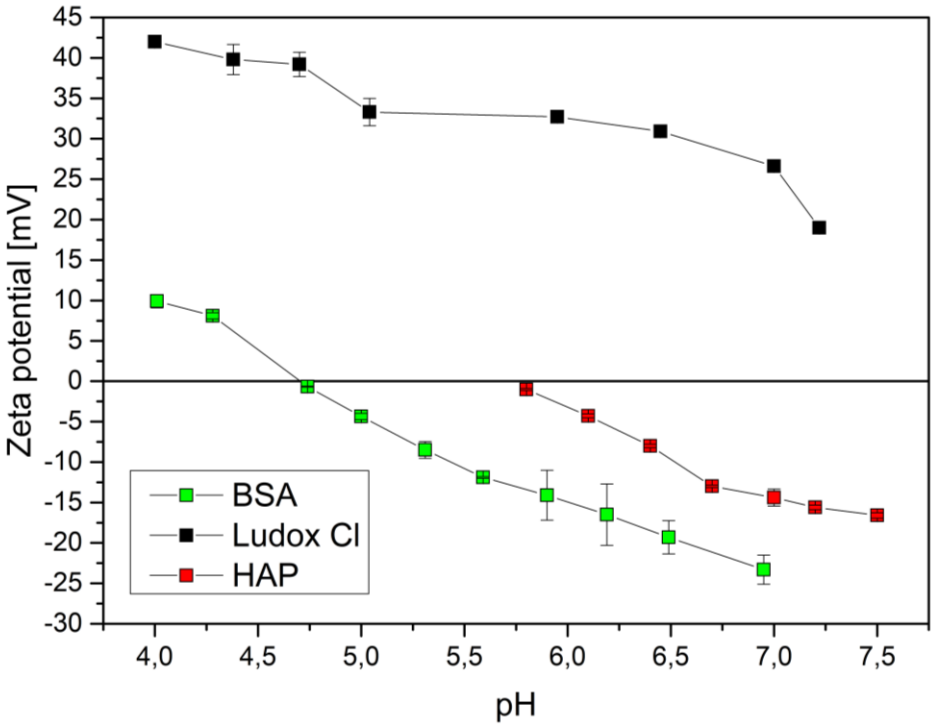

Figure 7.3 Zeta potential measurements of BSA, Ludox Cl and HAP at different pH values.

The measurements have been carried out to examine the charges of the different nanoparticles before and after the adsorption of BSA took place and to gain a deeper understanding of this process.

As reported in the literature the isoelectric point of BSA is at pH 4.7[242] and above this pH value BSA is negatively charged. In contrast, the Ludox Cl NPs have a strongly positive charge, which is the perfect precondition for the adsorption of BSA due to the electrostatic attraction between those positively charged particles and the negatively charged protein molecules. After the addition of BSA and a thorough washing process including multistep washing and subsequent centrifugation, the zeta potential of the Ludox Cl NPs with adsorbed BSA was reversed and had an equivalent zeta potential to BSA with a value of -19.8 mV at pH 6.6, showing that the adsorption was successful.

Table 7.1 List of zeta potential values of pristine and BSA modified nanoparticles.

Nanoparticles	pH	Zeta potential [mV]
BSA	6.5	-19.3 ± 2.1
BSA	7.0	-23.3 ± 1.8
Ludox Cl	6.5	+30.9 ± 0.5
BSA + Ludox Cl	6.6	-19.8 ± 0.4
HAP	7.0	-14.4 ± 1.1
BSA + HAP	7.0	-16.9 ± 0.4
Si71	7.0	-33.2 ± 0.1
BSA + Si71	7.0	-26.3 ± 0.1
$CaCO_3$ (hydrophilized)	7.4	-15.3 ± 1.3
BSA + $CaCO_3$	7.4	-25.1 ± 1.0

In the investigated pH range from 5.8–7.2 the HAP NPs synthesized with the standard route, which was described in the chapter 4.2., have a negative zeta potential as well as Si71 and $CaCO_3$ (hydrophilized) at pH 7 and 7.4, respectively. The IEP of $CaCO_3$ is usually at pH 8.9 and therefore the ZP at pH 7.4 should be essentially positive.[243, 244] This allows the assumption that the stearic acid was not completely removed from the $CaCO_3$ surface during its hydrophilization by sonication. However, after the adsorption of BSA the zeta potential of the modified HAP, Si71 and $CaCO_3$ NPs shows a slight shift towards the value measured for the pristine BSA. Since these NPs are not oppositely charged to BSA, the electrostatic attraction cannot be considered to be the driving force for the adsorption of the protein molecules. The protein adsorption is the result of various interactions between the components, including van der Waals forces, hydrogen bonding and hydrophobic interactions. Nevertheless, in particular cases like with Ludox Cl, the electrostatic forces clearly dominate the adsorption of BSA at the solid/water interface.

7.3. SEM and EDX

To obtain qualitative and quantitative information on the adsorption of BSA to the different NPs the energy dispersive x-ray spectroscopy (EDX) was performed. In chapter 3 “Materials and Methods” in section 4 detailed information about this technique can be found.

In Figure 7.4 a summary of the EDX measurements is given. Additionally, SEM images of the BSA modified NPs are shown on the left, while an overview of the elemental composition of the sample is displayed on the right.

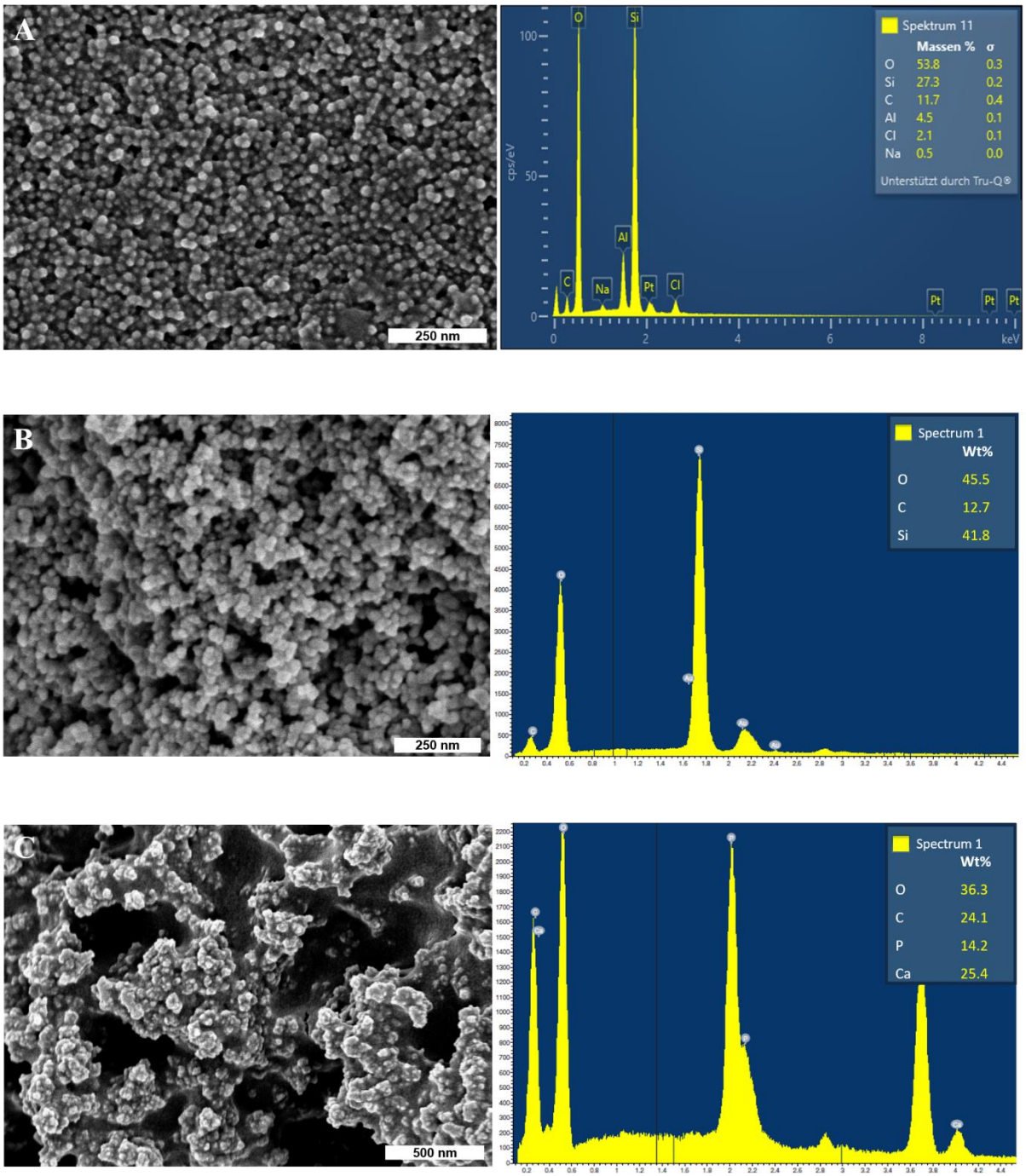

Figure 7.4 SEM images and EDX analysis of BSA modified nanoparticles: Ludox Cl (A), Si71 (B) and HAP (C).

The BSA modified Ludox Cl NPs consist mainly of oxygen with 53.8 wt% and silicon with 27.3 wt%. Furthermore, 4.5 wt% aluminum were detected, which is the evidence for the presence of Ludox Cl. In addition, 11.7 wt% carbon were detected confirming again the adsorption of BSA to the NPs like TGA and zeta potential measurements before. In contrast to the preparation for the capsule synthesis this sample was not washed with the BisTris buffer (pH =7) to avoid an influence on the intensity of the carbon signal. Instead, the sample was washed with distilled water, whose pH was adjusted to 7 with a 0.001 M NaOH solution. Therefore, 0.6 wt% sodium were detected.

In the elemental composition diagram of the BSA modified Si71 NPs 45.5 wt% oxygen and 41.8 wt% silicon were detected. The amount of detected carbon is in the same range as in the Ludox Cl sample at 12.7 wt%.

14.2 wt% phosphorus and 25.4 wt% calcium were detected in the dried BSA modified HAP NPs. Notably, this sample contained the highest amount of carbon with 24.1 wt%. These results are in accordance with the TGA measurements.

For a better comparison the pristine NPs were also analyzed with EDX (Figure 7.5). Notably, all spectra show a presence of ca. 5 wt% carbon, even though these NPs are not modified with BSA. At the accelerating voltage of 10 keV used in these experiments and the sample materials under consideration, the information depth of the EDX is of several micrometers and therefore much larger than NPs dimensions. Thus, the detected carbon peak can only be assigned to the carbon tape on the sample holder. Since all samples were prepared and analyzed in the same way, the carbon mass fractions in all samples of the NPs modified by BSA can be reduced by 5 wt%. After the correction the modified Ludox Cl and Si71 NPs contain ca. 7 wt% carbon and the modified HAP NP ca. 19 wt%.

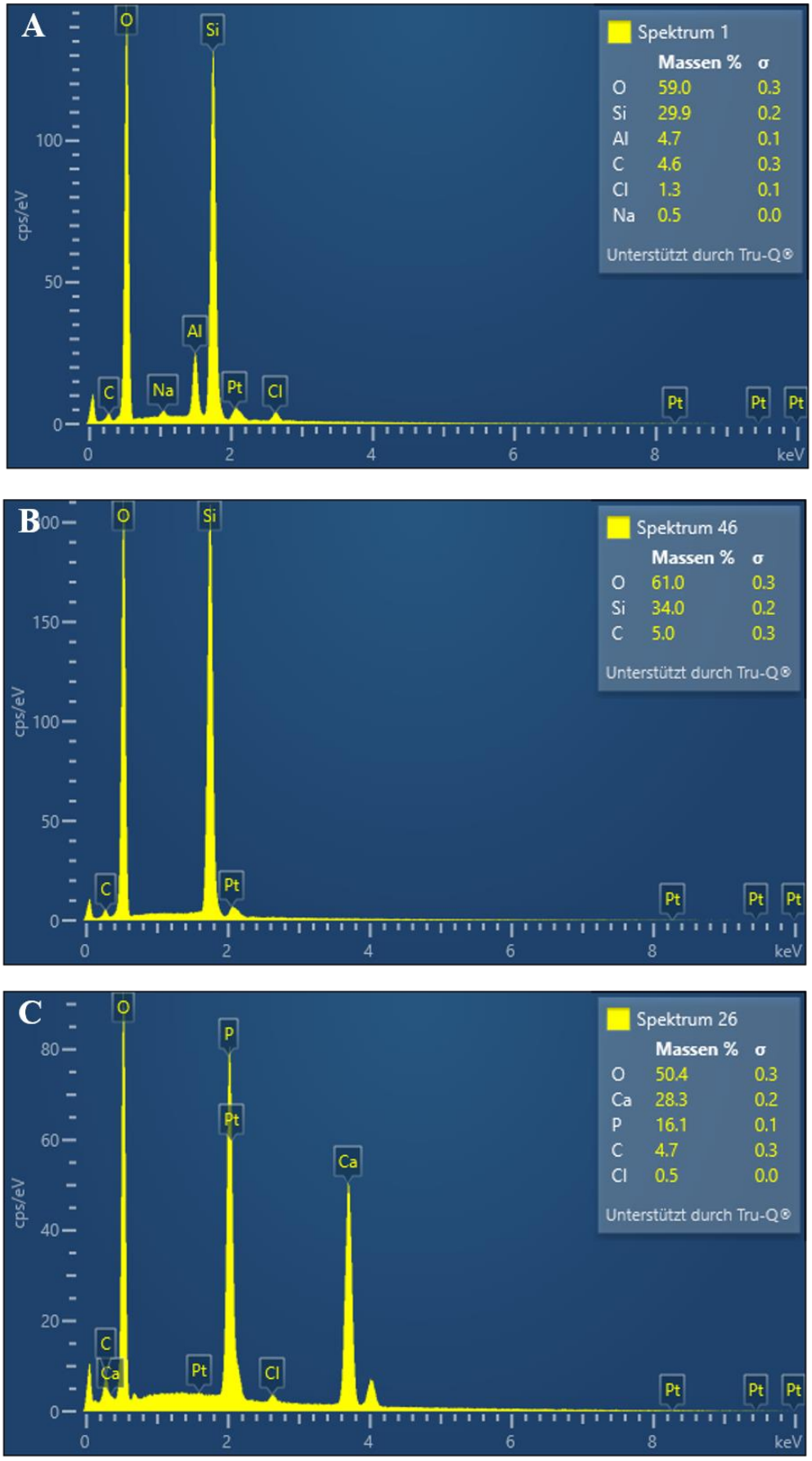

Figure 7.5 EDX analysis of pristine nanoparticles: Ludox Cl (A), Si71 (B) and HAP (C).

7.4. Raman Spectroscopy

To examine whether the adsorption of the BSA molecules to the NPs affects the protein conformation, the pristine and BSA modified NPs were additionally analyzed by Raman spectroscopy. The results are shown in Figure 7.6. BSA adsorbed on Ludox Cl and the pristine components are displayed in Figure 7.6 A. The spectrum of the BSA modified Ludox Cl NPs is basically the same as the pristine BSA spectrum. The additional peaks in this spectrum at 415 cm^{-1}, 747 cm^{-1}, 1077 cm^{-1} and 1266 cm^{-1} could be identified as buffer peaks caused by BisTris that was used during the washing process of the modified NPs to remove residual BSA, which was not adsorbed. Notably, the characteristic peak for the S–S vibration at 510 cm^{-1} is not present when BSA is adsorbed on the Ludox Cl NPs. Furthermore, the peaks of the amide I band at ~ 1655 cm^{-1} and of the CH_2 and CH_3 bending at ~1449 cm^{-1} were slightly shifted to ~ 1665 cm^{-1} and ~1460 cm^{-1} indicating that conformational changes take place when BSA adsorbs on the Ludox Cl NPs.[245] The amide I band is characteristic for the α-helix structure in BSA. Due to the interaction of BSA with the surface of the Ludox Cl NPs some of the α-helix structures may change to a β-sheet or random coil conformation. The bands that are typical for silica materials are only shown in the Raman spectrum of the pristine Ludox Cl particles. The bands at 250–650 cm^{-1} and 760–1100 cm^{-1} are attributed to the SiO_4 ring bending and Si–O stretching vibrational modes, respectively.[246] A CD study made by Giacomelli and Norde showed that the α-helix content of BSA decreased after adsorption on silica particles from 58% to 50%. The β-sheet content decreased as well by 8% while the unordered portion increased by 16%.[247] This study confirms that BSA changes its conformation upon adsorption on silica particles.

In Figure 7.6 B, the same peak shift can be observed in the spectrum of the BSA modified Si71 NPs. In contrast to the spectrum of the BSA modified Ludox Cl NPs, the characteristic peak of Si71 at ~ 500 cm^{-1} can also be found in the spectrum after the adsorption of BSA. So, it can be concluded that the BSA adsorption is much more effective on Ludox Cl resulting in a shielding of Raman scattering from Ludox Cl by BSA. As discussed before, the Si71 NPs have a negative zeta potential, consequently the adsorption was not caused by electrostatic attraction. However, Norde and Favier proposed that the decrease in ordered structure would be the driving force for the adsorption of negatively charged BSA molecules on negatively and hydrophilic silica surfaces.[248]

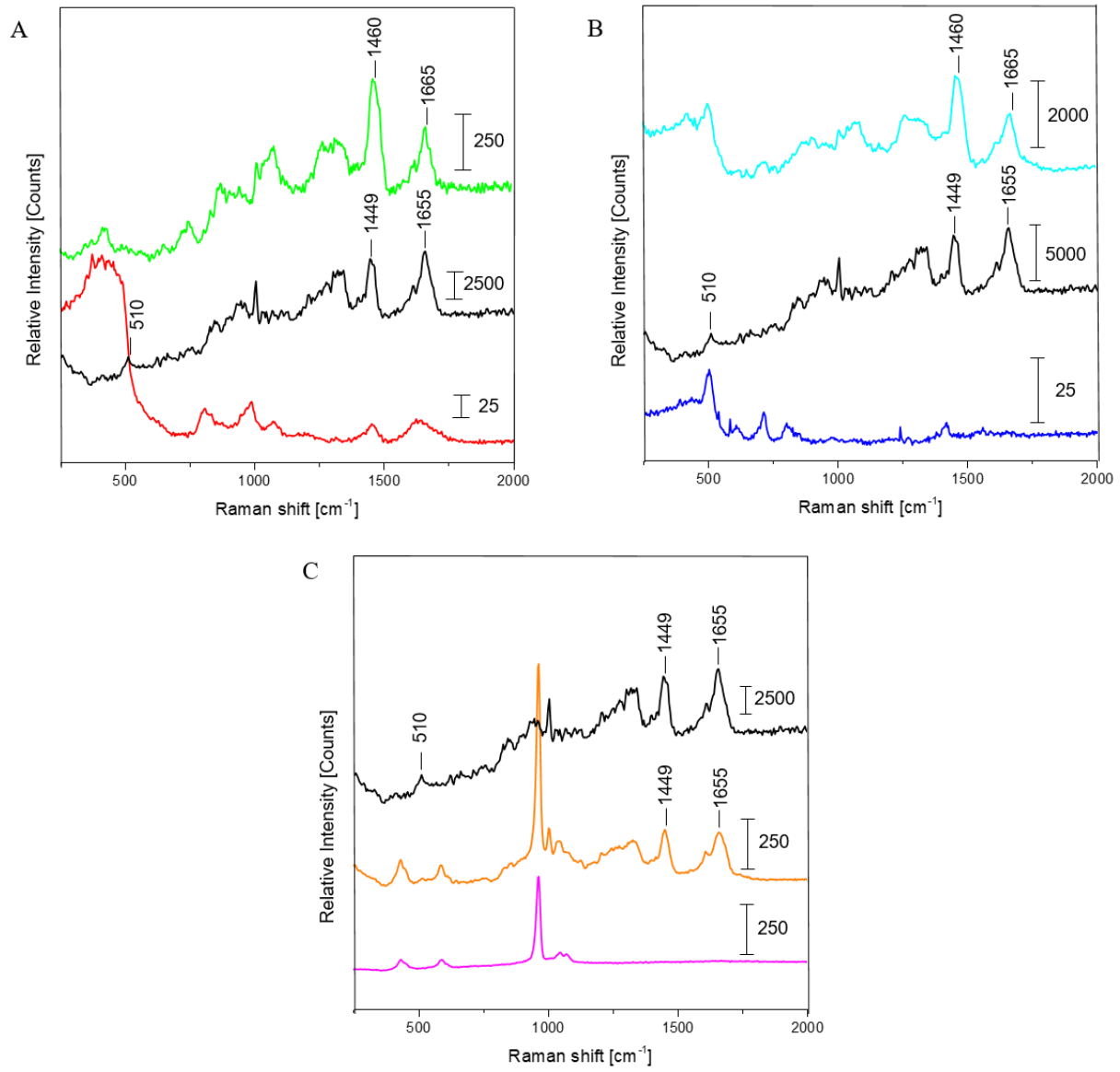

Figure 7.6 Raman spectra for: (A) pristine BSA (black), pristine Ludox Cl (red), BSA modified Ludox Cl (green), (B) pristine Si71 (blue), BSA modified Si71(light blue) and (C) pristine HAP (magenta) and BSA modified HAP (orange).

The Raman spectrum of BSA adsorbed to HAP NPs is depicted in Figure 7.6 C. The characteristic peaks of BSA and HAP are clearly recognizable and in contrast to the spectra of the BSA modified silica NPs, this spectrum is not only dominated by BSA peaks. Furthermore, the peaks of the adsorbed BSA on the HAP NPs appear at the same wavenumbers as the peaks of the pristine BSA. Consequently, no peak shift could be observed indicating that the secondary structure of BSA does not alter during adsorption to the HAP NPs. This was also confirmed by Swain, who analyzed BSA adsorbed to HAP with FTIR.[249]

8. Composite Protein Microcapsules

After the synthesis of the protein microcapsules and the successful adsorption of BSA on the surface of four different NPs, more complex protein-inorganic microcapsules with the payload of different oils were prepared using high-intensity ultrasound. The formation of the thin composite mineral proteinaceous shells was realized with the nanoparticles, which were pre-modified with BSA.

Using colloidal particles for the formation of the shell of the microcapsules, in this case silica, hydroxyapatite or calcium carbonate nanoparticles, is promising for the creation of new functional materials. The nanoparticulate building blocks of the composite shell with different chemical, physical or morphological properties can contribute to additional, sometimes even multiple, features of the resulting capsules.

The characterization and modification of composite protein microcapsules as well as the mechanism of their formation will be discussed in the following sections.

8.1. Formation of Composite Protein Microcapsules

The formation of the composite protein microcapsules is a result of emulsification. The oil-in-water (O/W) emulsion is formed due to the ultrasonic treatment of the two-phase liquid system and stabilized by modified nanoparticles, which became interfacially active after the adsorption of the BSA molecules on their surface, due to irreversible attachment of these NPs at the interface between aqueous medium and emulsion droplets. Although the ultrasound produces cavitation resulting in the formation of radicals, the intramolecular disulfide bonds were not broken and rearranged to form intermolecular bonds. The formation of a Pickering-Emulsion takes place because of the amphiphilicity-driven spontaneous attachment of the BSA-modified nanoparticles at the oil/water interface. Figure 8.1 displays the mechanism of the synthesis of oil loaded composite BSA microcapsules. The synthesis is described in detail in chapter 4.3. The obtained microcapsules exhibit a non-perfectly spherical morphology. The capsule sizes depend on the oil and the NPs that are used for the formation, which will be described in detail in the following section.

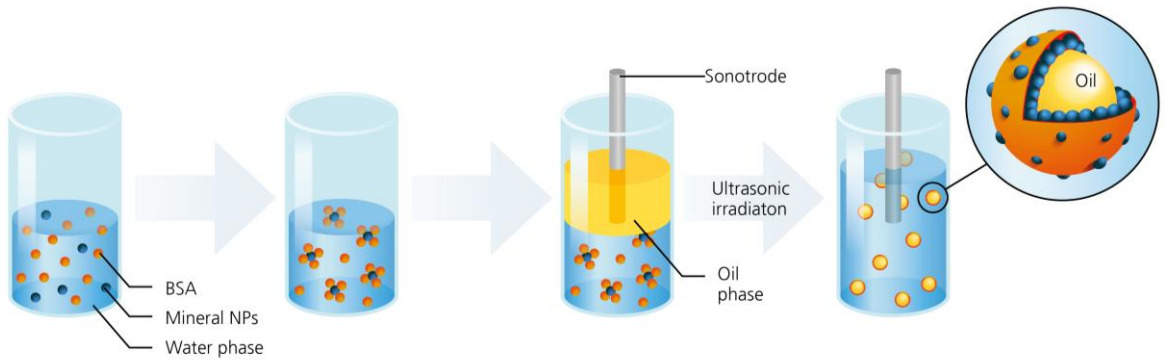

Figure 8.1 Synthesis scheme of oil loaded composite BSA microcapsules.

8.2. Influence of Nanoparticles and Oils on the Capsule Formation

Cryo SEM and cryo EDX were used to investigate the capsules morphology, fine structure and compostion of their shells with different NPs, where the elemental analysis gives information on the composition of the protein-mineral microcapsules. To visualize the distribution in the protein-mineral capsules EDX mapping was used. Raman spectroscopy was performed to examine the structural conformation of adsorbed BSA in the shell of the oil loaded composite microcapsules synthesized by ultrasound treatment.

Cryo SEM and Cryo EDX

The BSA-Ludox Cl microcapsules were synthesized by ultrasound and loaded with three different oils, respectively. The visualization of the capsules done by cryo SEM measurements is shown in Figure 8.2.

The cross section of a composite microcapsule, which was loaded with toluene, is shown in Figure 8.2 A. The shell of this composite microcapsule consists of individual Ludox Cl NPs and their aggregates forming a thin but almost densely packed particle layer at the oil-water interface.

The intact BSA-Ludox Cl microcapsule loaded with mint oil (Figure 8.2 B), which is partially imbedded in the matrix, does not exhibit spherical particles in the shell, while the inner shell surface shown in the cryo SEM image of the broken composite microcapsule loaded with Miglyol (Figure 8.2 C) is rather rough.

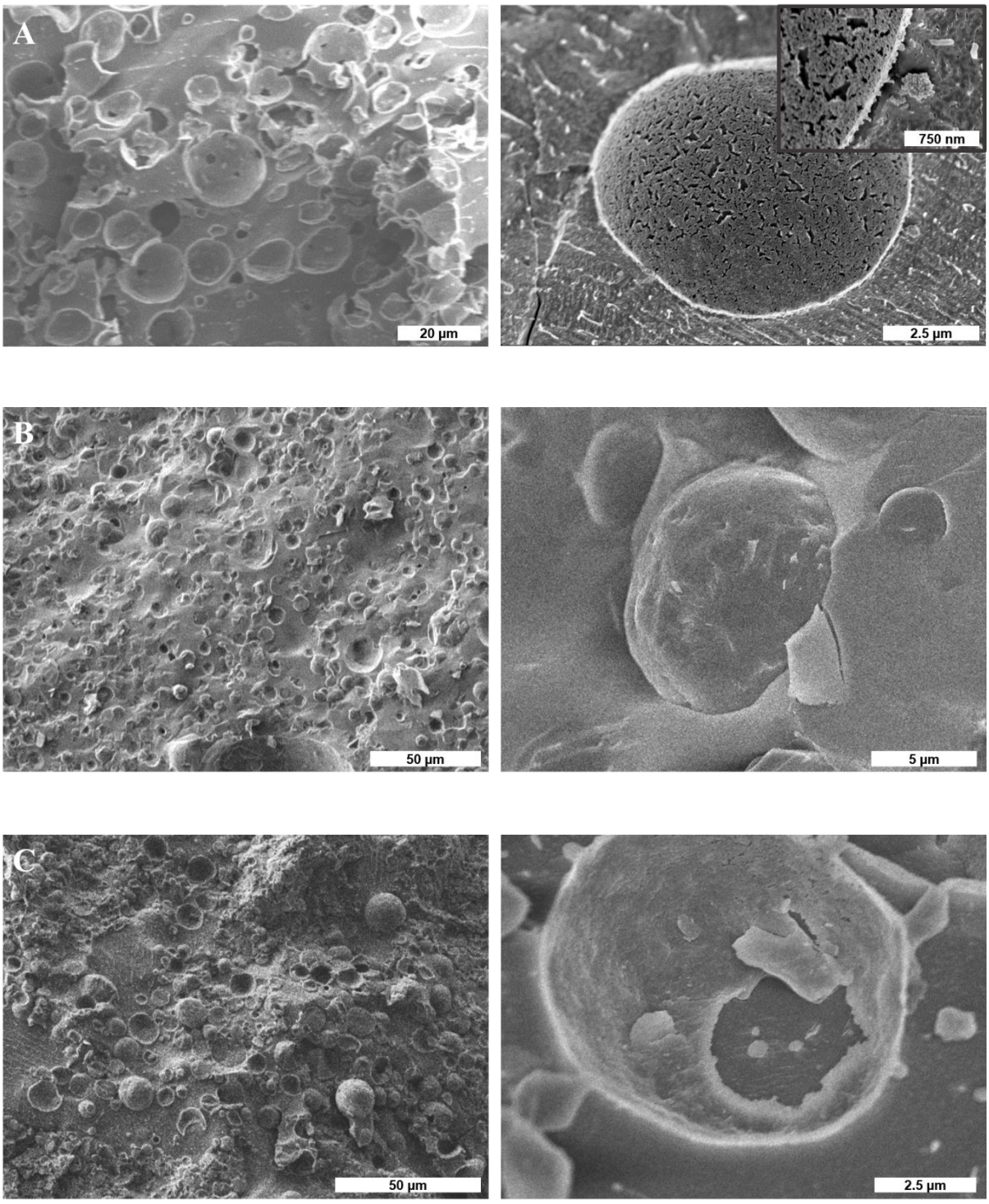

Figure 8.2 Cryo SEM images of composite BSA-Ludox Cl microcapsules loaded with different oils: toluene (A), mint oil (B) and Miglyol (C).

Notably, the composite microcapsules are larger and more polydisperse than the protein microcapsules synthesized without NPs. The toluene loaded composite capsules have sizes of 8–13 µm, while the composite capsules loaded with Miglyol and mint oil are slightly smaller with an average size of 5–7.5 µm. As shown before, the different oils have different interfacial energies, which also influences the attachment of the NPs at the interfaces of the oil droplets

and their sizes. However, all composite microcapsules have in common that they are not perfectly spherical shaped and have a rather rough surface.

Since the cryo SEM images only indicate the presence of the Ludox Cl NPs in the capsule shell, cryo EDX mapping of the composite microcapsules was performed for a better visualization of the particle distribution and for detection of the elemental composition. Figure 8.3 summarizes the EDX analysis results of BSA-Ludox Cl microcapsules loaded with toluene, mint oil and Miglyol. A cryo SEM image is shown on the left, the corresponding EDX mapping is displayed in the middle of the figure, while an overview of the elemental composition is given on the right. The EDX mapping results show that the shells of all capsules contain an essential amount of silicon (colored yellow) evidencing the presence of silica nanoparticles and their even distribution at the interface. Consequently, the capsules were successfully synthesized with Ludox Cl NPs. Furthermore, the EDX mapping shows the presence of carbon in the same area as silicon was detected caused by the modification of the Ludox Cl NPs with BSA, which is composed of amino acids. Additionally, carbon was detected in large amounts inside of broken capsules as well as in holes in the capsule shell due to residues of the loaded oil. 6.8 wt% carbon and 2.1 wt% silicon were detected in the capsule shell of BSA-Ludox Cl microcapsules loaded with toluene (Figure 8.3 A). The high amount of oxygen with 91.1 wt% is explained by the cryo measurement method, because the sample was prepared out of the liquid phase. The elemental composition of the microcapsules loaded with mint oil and Miglyol show a much higher amount of carbon with 58.4 wt% and 49.7 wt%, respectively, while the amount of silicon decreased to 0.6 wt% for both types of capsules. Since the analyzed capsules have holes or are broken, this increase in amount of carbon is caused by the residues of the loaded oils.

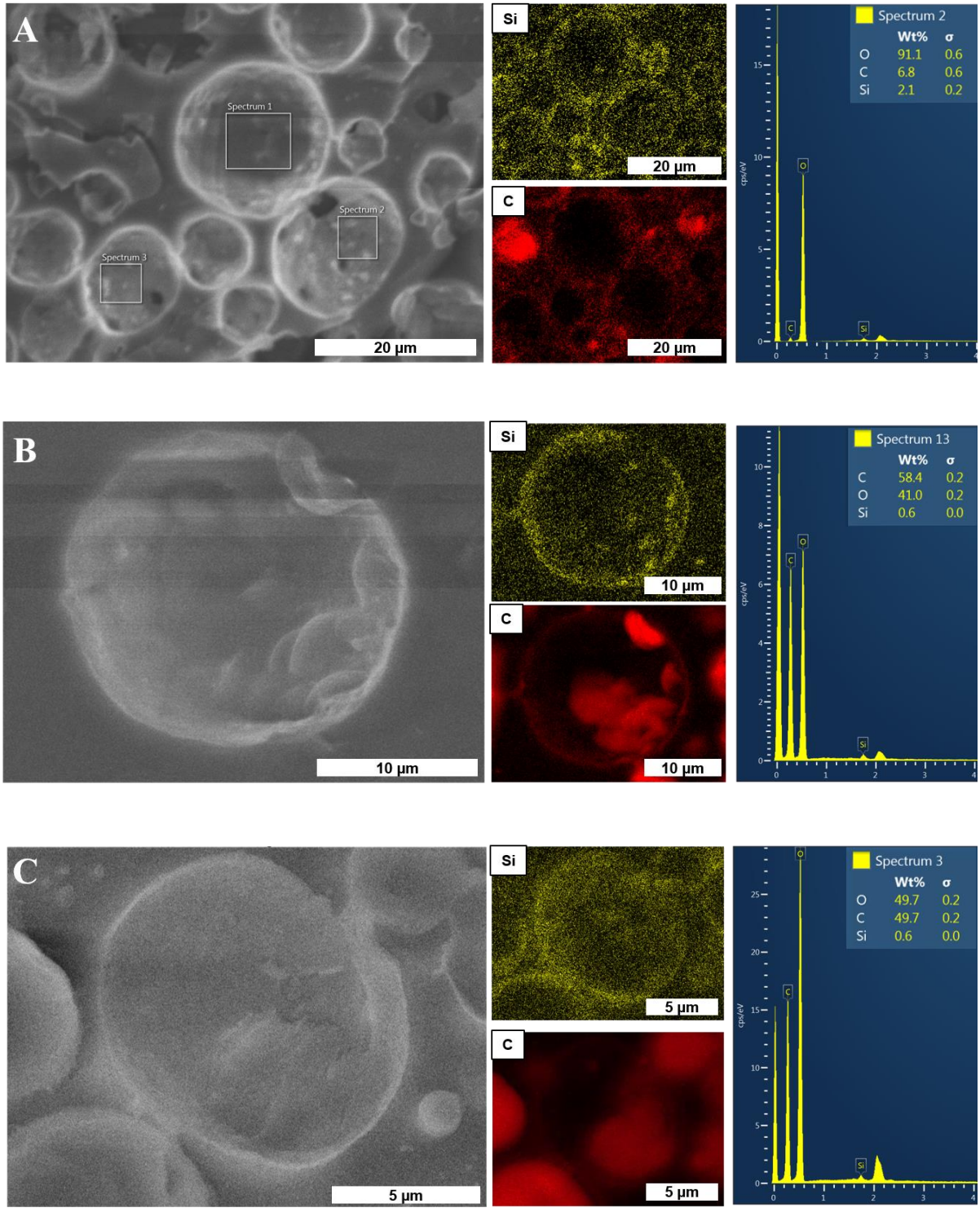

Figure 8.3 Cryo SEM images and cryo EDX analysis of composite BSA-Ludox Cl microcapsules loaded with different oils: toluene (A), mint oil (B) and Miglyol (C).

After the successful synthesis of composite protein microcapsules with a shell consisting of BSA modified Ludox Cl NPs and loaded with three different oils, microcapsules with other NPs (Si71, $CaCO_3$ and HAP) were synthesized.

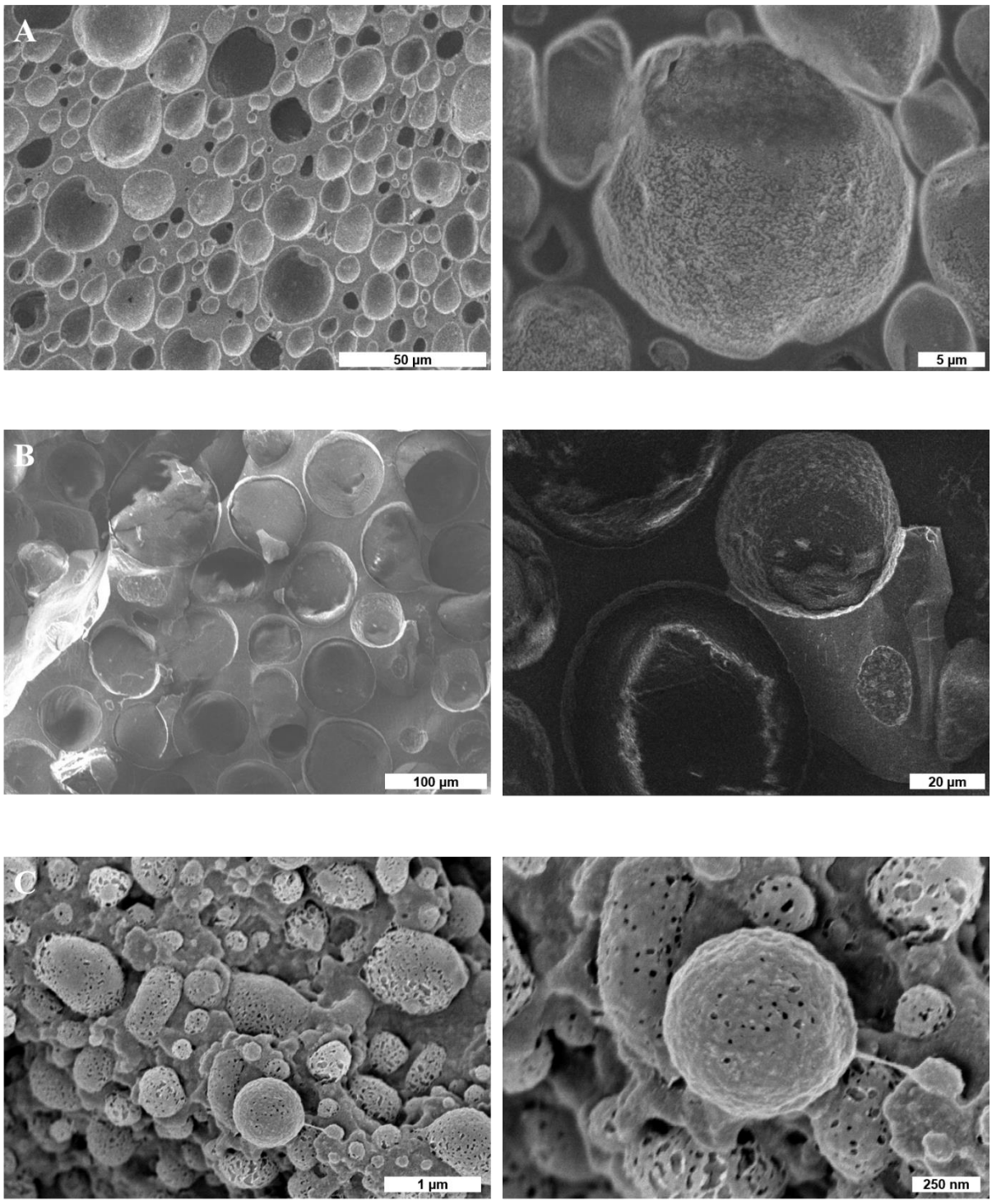

Figure 8.4 Cryo SEM images of composite BSA microcapsules loaded with toluene and synthesized with different nanoparticles: Si71 (A), $CaCO_3$ (B) and HAP (C).

The cryo SEM images of those microcapsules can be seen in Figure 8.4. The result of the microcapsule formation with Si71 is shown in Figure 8.4 A. The overview cryo SEM image illustrates the broad size distribution while the close-up image exhibits the rough inner shell surface of the BSA-Si71 microcapsule. The size of these capsules is similar to the ones

synthesized with Ludox Cl with an average size of 10 µm. However, the BSA-Si71 microcapsules demonstrate rather spheroidal shapes than spherical ones. The largest capsules were synthesized with $CaCO_3$ NPs with an average size of 50–60 µm. On the surface of these BSA-$CaCO_3$ microcapsules, a roughness can be observed as well (Figure 8.4 B). On the contrary, the composite microcapsules synthesized with HAP NPs were the smallest (Figure 8.4 C). They exhibit an average size of 1–2.5µm and in addition to a rough surface, they have numerous holes in the shell. These holes are probably caused by the evaporation of the loaded toluene during the preparation for the cryo SEM measurements. Notably, some of these microcapsules have a cylindrical shape. This shows, that the different NPs have strong influence on the size and shape of the microcapsules as they attach differently at the interface.

For more clarification of what causes this roughness on the shell surface, these capsules were analyzed with cryo EDX as well (see Figure 8.5).The EDX mapping and the corresponding elemental composition of the BSA-Si71 microcapsules (Figure 8.5 A) show similar results as seen before for the BSA Ludox Cl microcapsules that were loaded with toluene. Silicon and carbon were detected evenly distributed in the capsule shell. Even the detected amounts of silicon and carbon shown in the elemental composition are in a similar range. Figure 8.5 B shows the EDX mapping of the BSA-$CaCO_3$ microcapsules and as expected calcium and carbon were detected in the carbon shell. Notably, little aggregates are located on the inner shell surface, which are highly cyan colored indicating a high calcium content. On the other hand, the high carbon content in the middle of the broken microcapsule is once more attributed to the residues of the loaded oil causing a highly red colored spot. This is also reflected in the elemental composition showing 49.8 wt% of carbon, while the amount of calcium was 0.8 wt%. The amount of detected NPs is in a similar range as in the broken or holey capsules synthesized with Ludox Cl and loaded with mint oil or Miglyol (Figure 8.3). On the contrary, the EDX analysis of the BSA-HAP microcapsules loaded with toluene was more challenging. It is possible that the content of the incorporated particles was too low and below the detection limit, so that EDX mapping was not successful. Therefore, the BSA-HAP microcapsules were thoroughly washed with a dropping funnel, dried and then analyzed with EDX. The elemental composition proves that the BSA modified HAP NPs are contained in the capsule shell by detecting carbon, phosphorus and calcium in the dried and washed microcapsules.

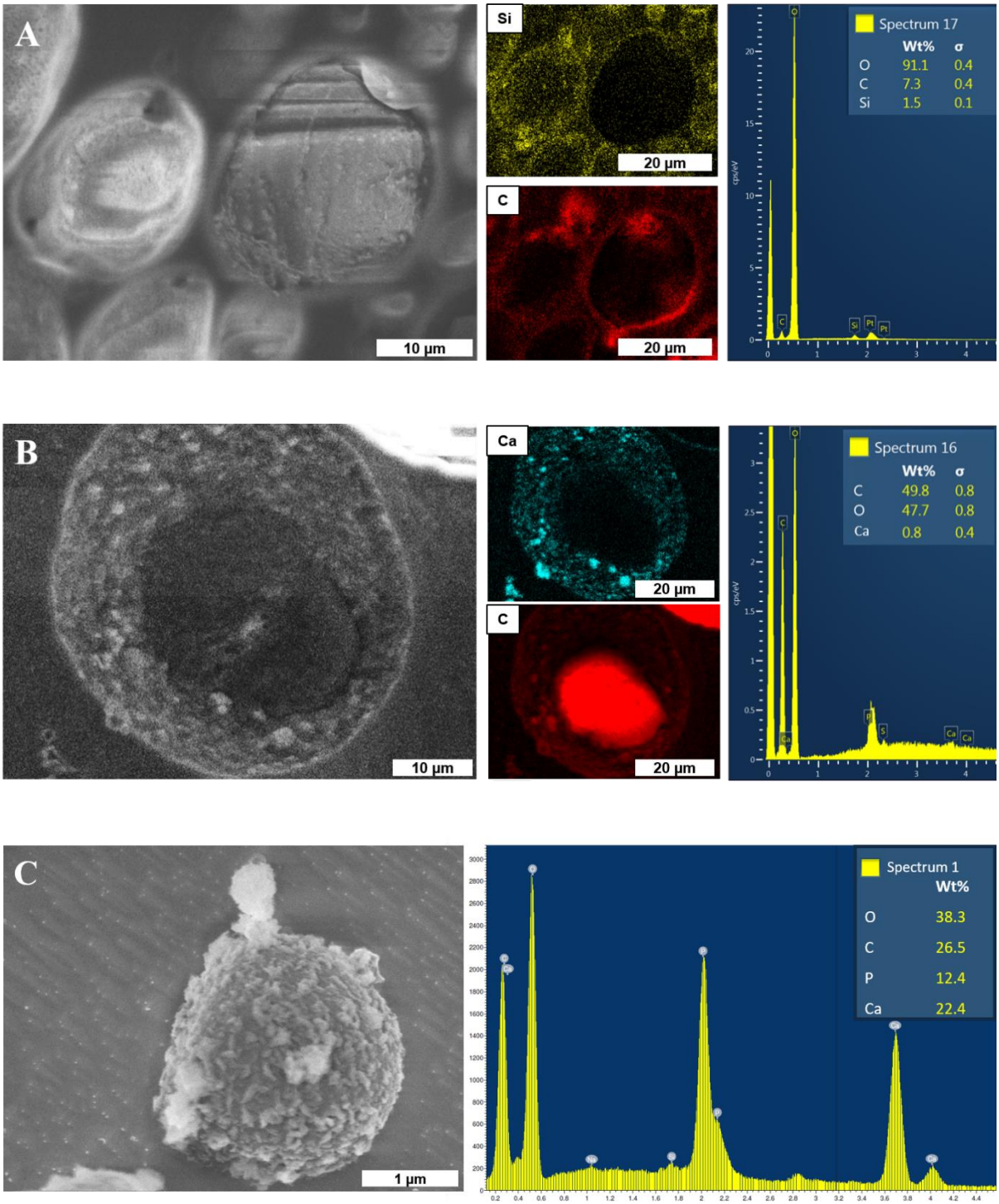

Figure 8.5 Cryo SEM images of composite BSA microcapsules loaded with toluene and synthesized with different nanoparticles: Si71 (A), $CaCO_3$ (B) and HAP (C); cryo EDX of capsules (A) and (B) and EDX of dried BSA-HAP microcapsules that were washed three times with a dropping funnel (C).

Raman Spectroscopy

After the successful characterization of the protein microcapsules and the BSA modified NPs, Raman spectroscopy was used again to examine the impact of the ultrasound treatment on the

BSA molecules that are adsorbed on the NPs surface while being at the oil/water interface and to understand the formation mechanism of composite protein microcapsules. The spectrum of the dried BSA-Ludox Cl microcapsules that were loaded with toluene is shown in Figure 8.6 and for a better comparison the spectra of pristine BSA, Ludox Cl NPs and BSA modified Ludox Cl NPs, which were discussed before, were added as well (Figure 8.6 A). Moreover, the spectrum of the dried BSA-toluene capsules without NPs was added in the right diagram (Figure 8.6 B) for better comparison.

The Raman spectra of BSA adsorbed on the Ludox Cl NPs and BSA in the shell of composite microcapsules made of Ludox Cl and BSA are nearly identical, which allows the assumption that the ultrasound treatment at the oil/water interface does not affect the conformational structure of the BSA adsorbed at the NPs surface. The comparison with the spectrum of the BSA microcapsules without NPs confirms that no conformational changes take place due to the absence of the two characteristic peaks of the cross-linked BSA at 487 cm^{-1} and 709 cm^{-1}, which were discussed before. This examination reveals that the BSA adsorbed on the NPs surface in the shell of the composite microcapsules are not cross-linked by intermolecular disulfide bonds, in contrast to the BSA molecules in the protein microcapsules made of BSA alone.

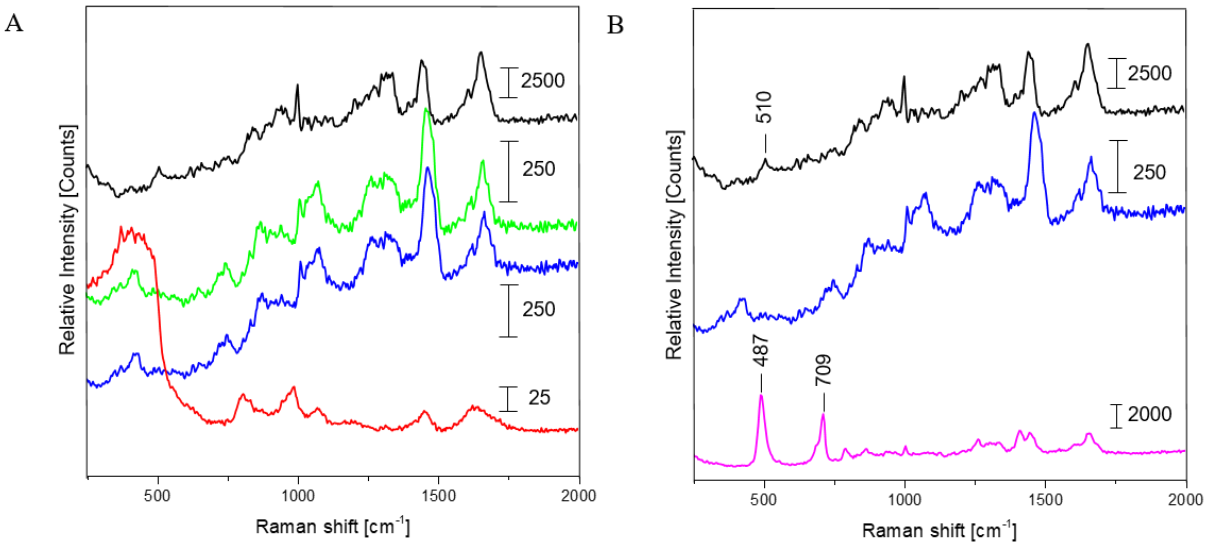

Figure 8.6 Raman spectra for : (A) pristine BSA (black), pristine Ludox Cl (red), BSA modified Ludox Cl (green), dried BSA-Ludox Cl capsules loaded with toluene (blue) and (B) dried BSA-toluene-capsules (magenta).

Instead, a Pickering-Emulsion formation takes place. When BSA is adsorbed on the NPs, it is not possible anymore to change its conformation at the oil-water interface in the fashion required for the formation of intermolecular disulfide bonds upon ultrasound treatment. Furthermore, it is likely that the sites of the BSA molecule containing the intramolecular disulfide bonds are less accessible to the radicals formed by the ultrasound treatment due to the adsorption of BSA on the NPs. Thus, the superoxide radicals are inhibited in the formation of intermolecular disulfide bonds.

8.3. Modification

Proteins can be labelled by modifying agents, which should contain moieties enabling their detection due to an intrinsic property like fluorescence. The reactive group of the modifying agent links to the functional group of the protein and after this modification the agent is covalently attached resulting in a permanently labelled protein with a unique detectable property. A variety of fluorophores is available for different applications. One of the most popular is fluorescein isothiocyanate (FITC), which is reactive towards nucleophilic sites like amines. Since FITC is able to form stable products with primary amine groups, it is highly selective for N-terminal amines in proteins.

The nucleophile attacks the electrophilic carbon of the isothiocyanate group resulting in the formation of a thiourea bond between the protein and FITC.[250] Figure 8.8 shows the BSA-Ludox Cl microcapsules loaded with toluene and modified with FITC. The fluorescence microscopy image visualizes the shell of the composite protein microcapsules consisting of the BSA modified Ludox Cl NPs. Moreover, this shows that the microcapsules can be easily modified via the primary amine group of BSA.

However, the silanol groups, Si–OH, on the surface of the Ludox Cl NPs can be easily modified to various functional groups as well by the treatment with different alkoxysilanes. 3-aminopropyltriethoxysilane (APTES) is one of the most applied alkoxysilanes, which is commonly used for the surface functionalization of silicon oxide surfaces. It can be used as an coupling agent for further functionalization due to its terminal amino group. During the modification of the Ludox Cl NPs the ethoxy groups of APTES react with the silanol groups on the silica surface to form stable siloxane bonds (Si–O–Si), resulting in ethanol as the leaving group and an aminopropyl-terminated surface.[251, 252]

APTES is very sensitive to several reaction conditions.[251, 253] Ethoxy groups can be hydrolyzed due to the presence of water in the system and via a condensation reaction. The resulting moieties react with each other to produce siloxane bonds leading to a 3D-polymerization. The result of the silanization without water in the system are reaction of only one, two or all three ethoxy groups with the silanol terminated Ludox Cl NPs. The free amine group is pointing towards the liquid phase and is available for further functionalizations (Figure 8.7 A).[254] It can be used as linkage unit to attach other functional molecules like FITC by forming thiourea linkage (see Figure 8.7 B).

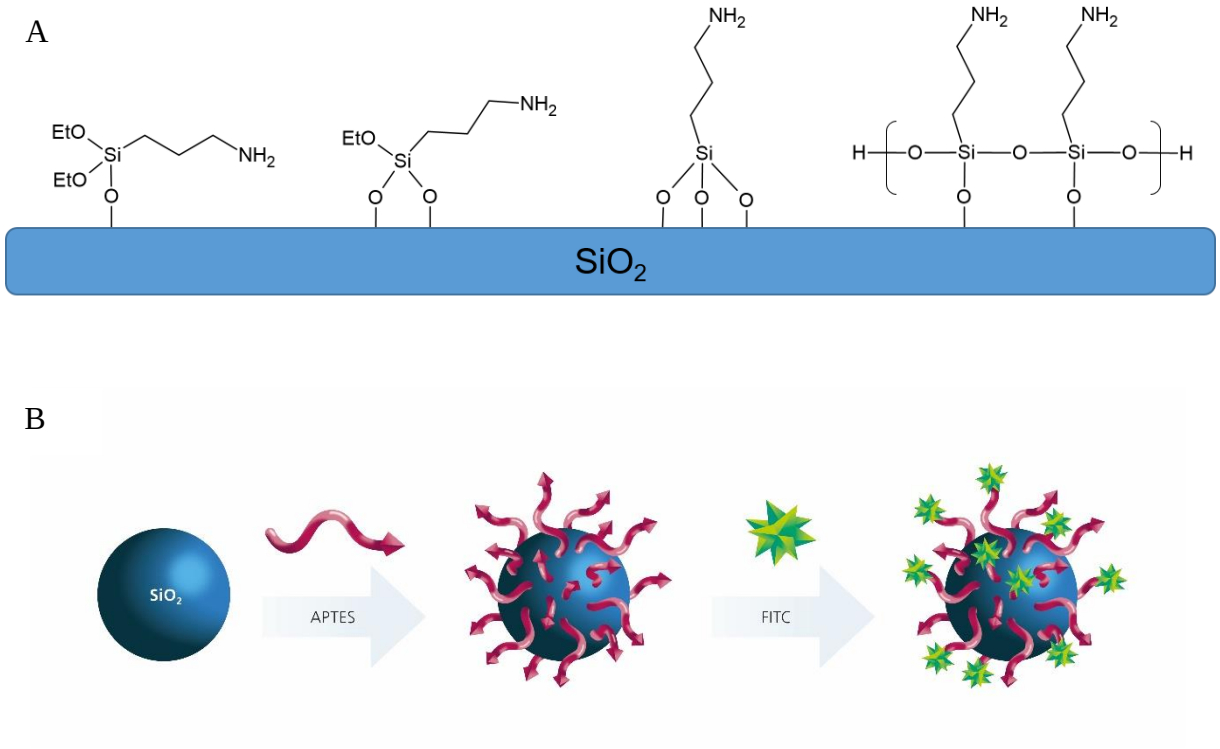

Figure 8.7 Possible orientation of the APTES molecule attached to the silanol-terminated silica (A) and illustration of the surface modification of Ludox Cl NPs with APTES and FITC (B).

The modification of Ludox Cl with APTES and subsequently with FITC was examined with fluorescence microscopy shown in Figure 8.8 and the Malvern Zetasizer Nano ZS shown in Table 8.1.

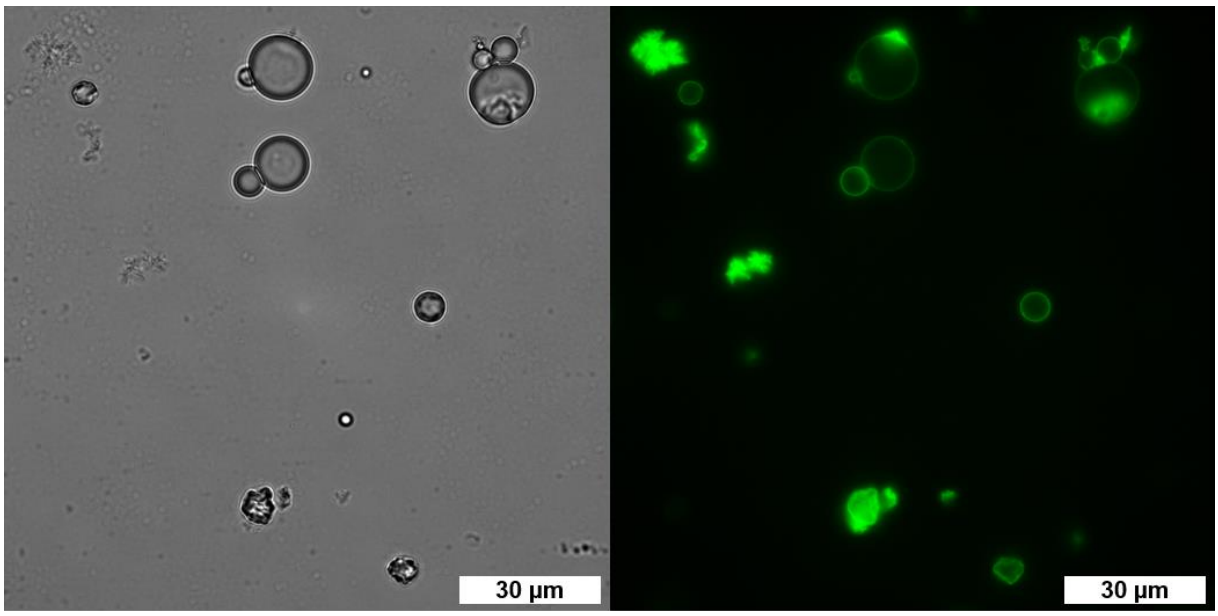

Figure 8.8 Microscopy and fluorescence microscopy image of BSA-Ludox Cl microcapsules loaded with toluene and modified with FITC.

Table 8.1 List of zeta potential values of pristine and modified Ludox Cl nanoparticles at pH=7.

Nanoparticles	Zeta potential [mV]
Ludox Cl	+26.6 ± 0.5
Ludox Cl + APTES	+42.9 ± 1.1
Ludox Cl + APTES + FITC	+29.7 ± 0.9

The modification with APTES increased the positive zeta potential of Ludox Cl from +26.6 mV to +42.9 mV, while the further modification with FITC via the amine groups resulted in a decrease of the zeta potential to +29.7 mV. Additionally, these FITC pre-labeled Ludox Cl NPs were modified with BSA as usually and used for the synthesis of composite microcapsules loaded with toluene via ultrasonication shown in Figure 8.9 A. As can be seen in the fluorescence microscopy image, the shell of the successfully synthesized composite microcapsules consists of the Ludox Cl NPs that were modified with APTES, FITC and BSA.

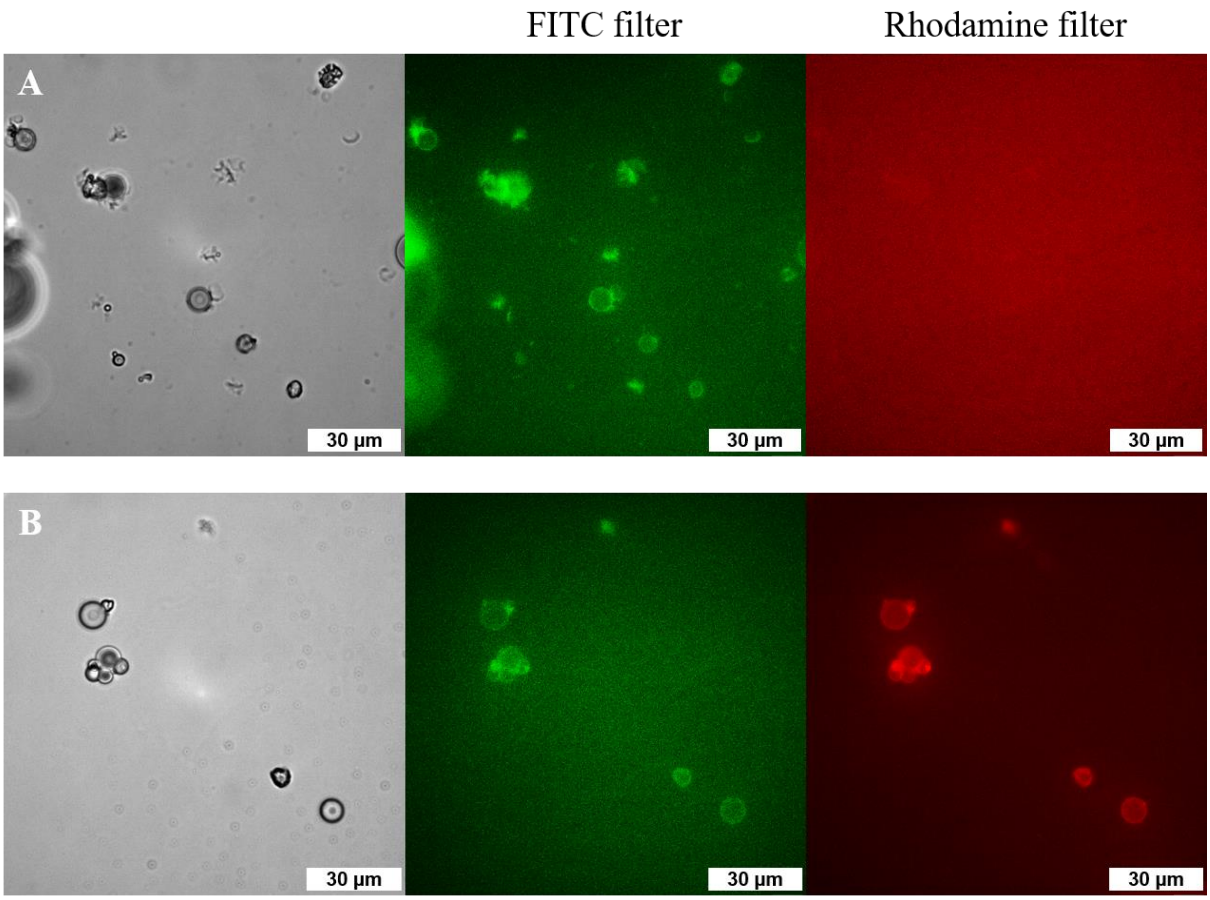

Figure 8.9 Microscopy and fluorescence microscopy images of BSA-Ludox Cl microcapsules loaded with toluene that were modified with APTES and FITC (A) and additionally with RITC (B).

After the successful modification of the composite microcapsules via the amine groups of BSA and the silanol groups of the Ludox Cl NPs separately, it was also possible to synthesize capsules that were modified simultaneously via BSA and Ludox Cl. For this synthesis BSA was pre-modified with rhodamine B isothiocyanate (RITC) via the reaction of the isothiocyanate group with the amino group of BSA (see Figure 8.9 B). The microscopy images with different filters show clearly the fluorescence of FITC attached to APTES that was bound to the Ludox Cl NPs and of RITC, which is linked to BSA.

9. Measurements of mechanical properties using SFM

The mechanical properties of the capsule shell are very important for many applications as they determine the stability of the microcapsules. Therefore, it was examined how the presence of inorganic NPs in the shell of the microcapsules affects their Young's modulus. For this purpose, scanning force microscopy (SFM) compression measurements of Miglyol loaded BSA microcapsules and composite BSA microcapsules were conducted in aqueous environment. Usually these nanocompression measurements are performed by approaching the microcapsules with a glass bead glued at a tipless cantilever known as colloidal probe. However, Glynos and coworkers showed that these measurements are also possible without using this technique by using bare cantilevers instead for the determination of the Young's modulus of microcapsules with thin polylactide shell.[255]

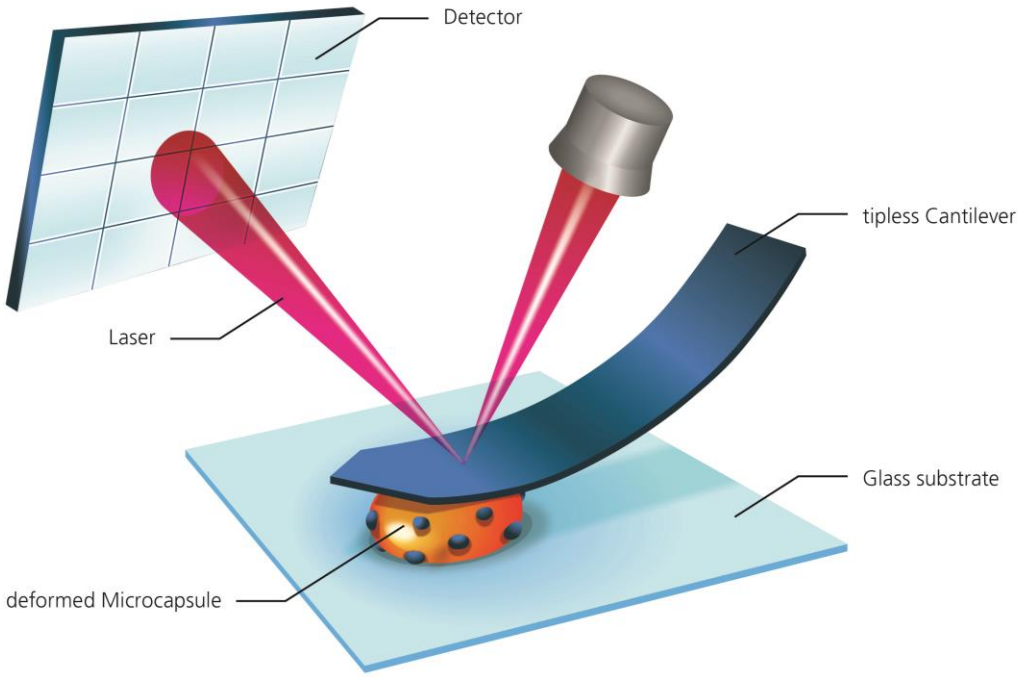

Figure 9.1 SFM indentation for Young's modulus determination of composite microcapsules

Since it turned out to be challenging to exert the load with the glass bead at the poles of the microcapsules without them moving away, bare cantilevers were used to deform the thin-walled microcapsules and calculate their Young's modulus (see Figure 9.1). The experimental

dependencies of force as function of deformation for different types of microcapsules are presented in Figure 9.2.

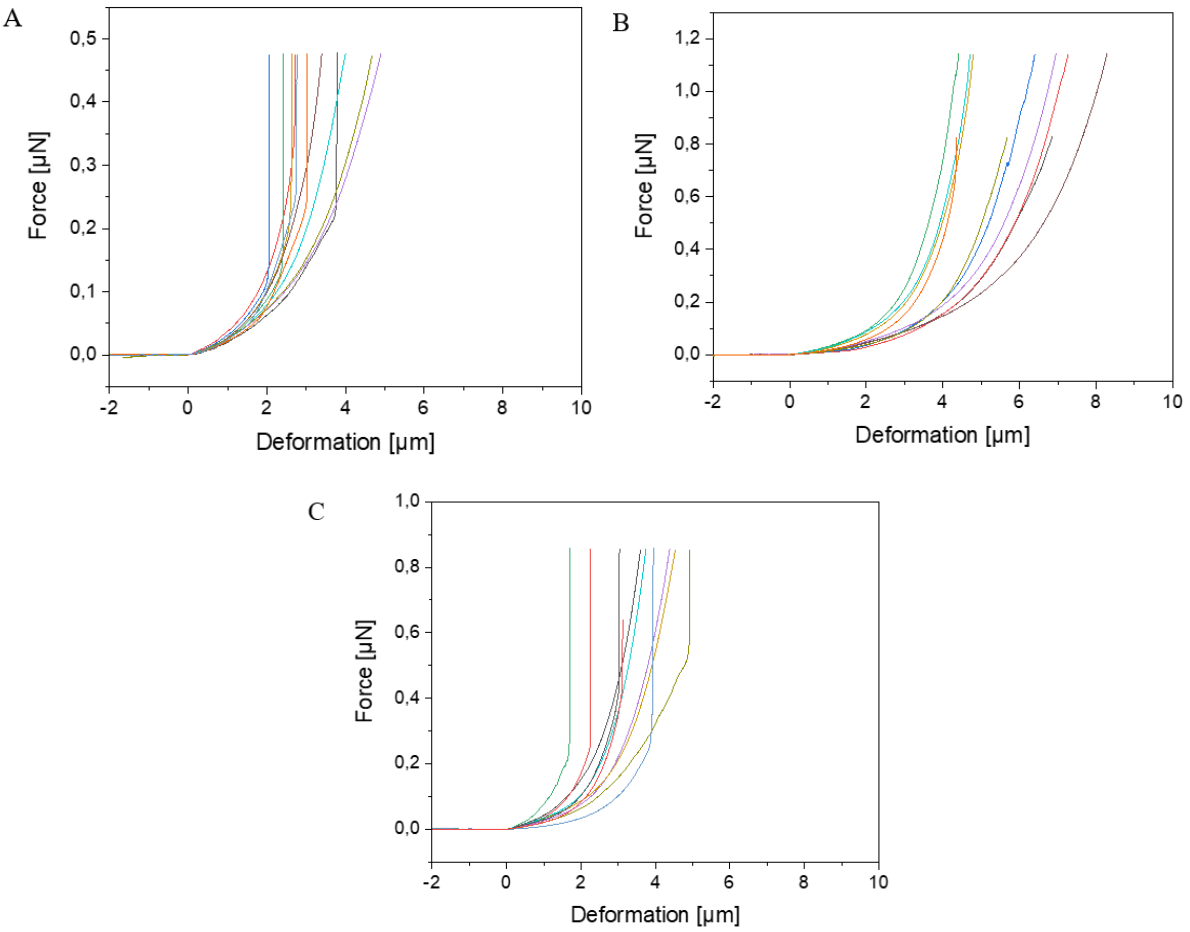

Figure 9.2 Force versus deformation curves of (A) BSA-Miglyol capsules, (B) composite BSA-Miglyol capsules with 2.6% Ludox Cl and (C) with 4.7% Ludox Cl in the shell.

A zero force baseline is observed during the approach before the contact with the sample. Upon further approaching, the cantilever contacts the sample. In the small deformation regime, the indentation increases linearly with applied force when the capsules are compressed (see Figure 9.3). The microcapsules show elastic response in this regime. The initial linear part of the resulting curves is used for the determination of the mechanical properties of the microcapsules. Notable that the distance on the force-deformation curve between the first non-zero point and its abruptly increasing region is sufficiently smaller than the size of the investigated microcapsules. This phenomenon is caused by the non-horizontal tilted orientation of the cantilever and by the fact that the capsules under measurement were compressed not by its terminal part but by its middle part (see Figure 9.1). Although the size of the investigated capsules was essentially larger than this distance with the typical length of 2 to 4 micrometers,

their small deformation by the middle part of the cantilever was accompanied by the contact between its terminal part and the rigid glass surface on which the microcapsules are immobilized leading to the vertical increase of the measured force (see Figure 9.2). Before every measurement with the SFM, microscopic images of the microcapsules were recorded for the determination of their sizes. The BSA-Miglyol microcapsules had an average size of 5.4 ± 1.1 µm and a shell thickness of 10 nm (as determined in 5.2. with SFM and with cryo SEM), while the composite microcapsules with 2.6% Ludox Cl in the shell had an average size of 7.6 ± 1.8 µm. An increase of the NP concentration to 4.7% resulted in a slight decrease of the average composite microcapsules size with 5.6 ± 1.8µm. According to cryo SEM microphotographs shown in Figure 8.2 (chapter 8.2), the silica NPs participating in the shell formation of composite microcapsules demonstrate nearly monolayer structures. Therefore, the shell thickness in all types of composite capsules investigated here were estimated to be of 25 nm.

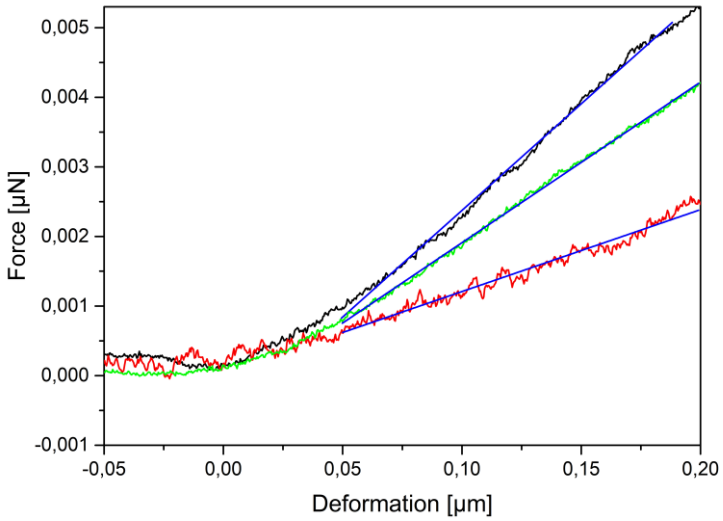

Figure 9.3 Force versus deformation curves of the small deformation regime of (black) BSA-Miglyol capsules, (red) composite BSA-Miglyol capsules with 2.6% Ludox Cl and (green) with 4.7% Ludox Cl in the shell.

The BSA-Miglyol capsules without NPs exhibited a higher initial slope in the small deformation regime of the force-deformation curve than the composite microcapsules. This indicates that the cross-linked microcapsules possess a higher stiffness than capsules without cross-linked BSA molecules in the shell. However, the slopes of the composite microcapsules

show that their mechanical properties can be tailored by varying the concentration of the NPs as the slope increased with increasing Ludox Cl concentration.

To calculate the Young's modulus of the microcapsules, the analytical solution of Reissner[256, 257] can be applied for small deformations of isotropically elastic thin-shell microcapsules under the following conditions: the ratio of shell thickness to radius should be smaller than 1/20 and a point-like load must be exerted at the poles of the capsules.[255] The equation connecting the force and the deformation with the material and the geometric characteristics of the thin-shell microcapsules of a radius *R* and a shell thickness *h* is as follows:

$$E = \frac{\sqrt{3(1-\nu^2)}}{4}\frac{R}{h^2}S \tag{9.1}$$

E is the Young's modulus and *v* the Poisson's ratio, which was assumed as 0.5 due to BSA being an isotropic incompressible elastic material, while *s* is the slope of the initial linear part of the force deformation-curve. The Young's moduli calculated with this equation are shown in Table 9.1.

Table 9.1 Young's modulus of BSA-Miglyol capsules and composite BSA-Miglyol capsules.

Microcapsules	**Young's modulus [112]**
BSA-Miglyol	191 MPa ± 64 MPa
BSA-Miglyol-Ludox Cl (2.6%)	29 MPa ± 7 MPa
BSA-Miglyol-Ludox Cl (4.7%)	38 MPa ± 12 MPa

The BSA-Miglyol capsules exhibited the highest Young's modulus with 191 MPa ± 64 MPa. A comparable system was described by Ye and coworkers, who used the colloidal probe technique in SFM to determine the Young's modulus of pea protein microcapsules.[28] These capsules were also synthesized by sonication and due to the high content of cysteine, the formation is based on the cross-linking mechanism as well. Moreover, the diameter of the pea protein capsules are with 3–5 µm in a similar range as the BSA-Miglyol capsules. Nevertheless, the obtained average Young's modulus is significantly lower with 0.58 to 2.35 MPa. The critical difference between the two systems is the shell thickness, ranging from 60–130 nm in the pea protein capsules. According to equation 9.1, the Young's modulus is inversely

proportional to the square of the shell thickness meaning that the largest shell thickness has the lowest modulus.

Notably, the Young's modulus is slightly higher when the nanoparticle concentration was increased. Nevertheless, the values of Young's modulus for the composite capsules are significantly smaller than one found for protein microcapsules. The strong influence of the shell thickness is also confirmed by values of Young's modulus obtained for the composite BSA-Miglyol capsules with 2.6% and 4.7% Ludox Cl in the shell being 29 MPa ± 7 MPa and 38 MPa ± 12 MPa, respectively. Similar decrease was also observed by Kolesnikova and coworkers.[258] They synthesized polyelectrolyte capsules and embedded ZnO nanoparticles in the shell. The Young's modulus decreased with increasing number of ZnO layers in the capsules as well as the slope of the initial linear part of the force-deformation-curve, which is used for the calculations of the Young's modulus. The capsules without ZnO NPs in the shell with a size of approximately 10 µm and a shell thickness of 32 nm exhibited a Young's modulus of 580 ± 286 MPa. Embedding three or four layers of ZnO NPs led to an increase of the diameters to 13–15 µm and of the shell thickness to 97–104 nm, while the Young's modulus decreased significantly to 18–36 MPa and 25–36 MPa, respectively. The Reissner model used for the calculation of the Young's modulus of these polyelectrolyte capsules takes into account the capsule diameter and shell thickness (see eq. 9.1). An increase of the shell thickness caused by the increasing number of ZnO layers results in a decrease of the Young's modulus. This decrease is also connected with the concentration of the NPs in the capsule shell, significantly affecting the stability of the capsules.[259] Thus, the NPs dominate the shell mechanics above a certain concentration.

Another system comparable to the cross-linked BSA microcapsules was described by De Loubens and coworkers.[260] They examined the mechanical properties of human serum albumin (HSA) microcapsules, which were synthesized by cross-linking of HSA with terephthaloyl chloride in a water-in-oil emulsion. The capsules that were obtained by stirring were considerably larger with a size of 200–600 µm and had a much higher shell thickness of 2 to 20 µm. The SFM measurements were performed using the colloidal probe technique and the calculated Young's modulus varied from 20 kPa to 1 MPa. However, in contrast to the papers considered above, they used the Hertz model[261] for the calculation of the Young's modulus of their capsules. The Young's modulus is related to the applied force F as follows:

$$F = \frac{4}{3} \frac{\tilde{R}^{1/2} \delta^{3/2}}{\frac{(1-\nu_t^2)}{E_t} + \frac{(1-\nu^2)}{E}} \tag{9.2}$$

$$\text{with} \quad \tilde{R} = \left(\frac{1}{R} + \frac{1}{R_t}\right)^{-1}$$

Where E_t is the Young's modulus of the tip with the colloidal probe and E of the capsule, while $\nu_t = \nu = 0.5$ the Poisson ratios of the tip and capsule. R_t and R are the radius of the tip and the capsule, respectively and δ is the indentation.

Both models, Hertz and Reissner, are applicable in the elastic regime, which corresponds to the small deformations. The Reissner model becomes more appropriate as the h/R ratio decreases, while the Hertz model is employed for soft cell-like shells in spherical approximation.[262] Furthermore, in comparison to the Reissner model, the Hertz model takes into account the shape of the tip. Nevertheless, using the Hertz model to investigate the force-deformation curves may result in an underestimation of the rigidity. Eid and coworkers found a discrepancy between the values using the Hertz model and the values obtained with other techniques being up to three orders of magnitude. On the other side, the values obtained using the Reissner model were close to the values obtained by other experimental techniques.[263] The difference in the size between the HSA capsules and the BSA capsules investigated in this work is significant as well as the difference in the shell thickness. In contrast to the Reissner model, the Hertz model does not take into account shell thickness of the capsules. All these parameters caused the lower Young's modulus of the HSA microcapsules in comparison with the BSA microcapsules.

The results of the SFM compression measurements of the BSA and the composite BSA microcapsules are consistent with the Raman measurements described in 8.2. In the shell of the protein capsules the BSA molecules are cross-linked via intermolecular disulfide bonds induced by the ultrasound treatment. The shell of the composite capsules does not consist of cross-linked BSA molecules since the adsorption of BSA on the silica nanoparticles leads to conformational changes in the protein prohibiting the cross-linking. Therefore, the resulting microcapsules represent the droplets of an oil-in-water Pickering emulsion with essentially lower Young's modulus. These measurements show that the cross-linked microcapsules offer higher resistance to the elastic deformation.

10. Conclusion

Within this thesis, two different systems were investigated: protein microcapsules and composite protein-mineral microcapsules. In both systems, the used protein was BSA, while additionally various types of NPs were used as shell material for the composite microcapsules. High intensity ultrasound was applied in similar fashion for the preparation of both types of microcapsules with different oils following the concept proposed by Suslick.[20, 35, 193] However, the formation mechanisms of the protein and the composite microcapsules exhibited differences. Although the capsules of both types are formed using the droplets of an O/W emulsion as template, the BSA microcapsules were based on a protein-stabilized emulsion whereas the composite microcapsules were based on a Pickering emulsion that is stabilized by NPs pre-modified with BSA. In case of the protein microcapsules, the amphiphilic BSA adsorbed at the O/W interface and due to the ultrasonic treatment, the protein molecules were cross-linked via the formation of intermolecular disulfide bonds stabilizing the capsule shell. In case of the composite protein-mineral microcapsules, different NPs including hydroxyapatite, silica and calcium carbonate are attached at the O/W interface due to the surface pre-modification with BSA. However, the BSA molecules in the shell of these composite microcapsules are not cross-linked since the adsorption of BSA on the nanoparticle surface prevents conformations of the protein required for the formation of the intermolecular disulfide bonds. Nevertheless, biocompatible microcapsules were prepared in both cases.

For a better understanding of the impact of the protein in the capsule formation, investigations on the protein dynamics via pendant drop tensiometry have been carried out. It was shown that the rate of the protein diffusion towards the O/W interface depends strongly on the protein concentration. With increasing the protein concentration, the adsorption kinetics of BSA became faster. Additionally, the type of oil influences the adsorption behavior. It was demonstrated that BSA adsorbs faster at the interface with Miglyol or mint oil and slower at the interface with toluene. The highest IFT was obtained with toluene, while the IFT values with Miglyol or mint oil were lower.

Different oils can be used for the preparation of protein microcapsules and composite protein-mineral microcapsules and it has been shown that toluene, Miglyol and mint oil are suitable oils for this purpose. The type of oil as well as the type of NPs have an impact on the capsule formation resulting in different capsule sizes. Different oils have different interfacial energies,

which influences the attachment of the NPs at the interfaces of the oil droplets and their sizes. Different NPs also have a strong influence on the size and shape of the microcapsules as they attach differently at the interface.

In addition, the mechanical properties of the protein microcapsules and the composite protein-mineral microcapsules were examined using SFM compression measurements and the following analysis of these according to the Reissner model. The comparison of the obtain results showed, that the cross-linked protein microcapsules offer higher resistance to elastic deformation than non-cross-linked composite microcapsules, in spite of higher rigidity of nanoparticulate building blocks and enhanced thickness of capsule shell.

The investigations presented in this thesis have been carried out to gain a deeper understanding of the underlying mechanisms of the capsule formations with and without NPs. Other main goal of the thesis at hand was the use of this newly acquired knowledge for the optimization of the capsule preparation and for the enhancement of their versatility by application of different NPs and by surface modification.

11. Summary

This thesis deals with the synthesis of protein and composite protein-mineral microcapsules by the application of high-intensity ultrasound at the oil-water interface. More precisely, the droplets of the oil-in-water emulsion arising due to a strong energy input serve as a microtemplate for the formation of both capsules types. While one system is stabilized by BSA molecules initially working as a surfactant and practically simultaneously as cross-linkable building unit of the capsule shells, the other system is stabilized by different NPs modified with BSA providing them the ability of an irreversible attachment at the oil-water interface (formation of Pickering emulsion) upon the ultrasonic treatment. Starting from the previously reported preparation procedure of protein microcapsules, a comprehensive study of all synthesis stages as well as of resulting capsules were carried out and a plausible explanation of the capsule formation mechanism was proposed. In addition, to gain a better understanding of protein adsorption kinetics on the surface of emulsion droplets, the interfacial tension at the oil-water boundary was studied as a function of time, protein concentration and the chemical nature of the oil.

During the formation of BSA microcapsules, the protein molecules adsorb firstly at the O/W interface and unfold there forming an interfacial network stabilized by hydrophobic interactions and hydrogen bonds between neighboring molecules, which initially stabilizes the emulsion droplets in aqueous media. Simultaneously, the ultrasonic treatment causes the cross-linking of the BSA molecules via the formation of intermolecular disulfide bonds. Thus, cross-linked protein microcapsules exhibit increased stability compared to the droplets of an oil-in-water emulsion prepared by a simple comminution (e.g. vortexing) in a protein solution. The three used oils (toluene, Miglyol and mint oil) have proven to be suitable for the preparation of protein and composite protein-mineral microcapsules.

In this thesis, the experimental evidences of ultrasonically induced cross-linking of the BSA in the shells of protein-based microcapsules are demonstrated. Comparison of the results of SDS-PAGE, DLS and Raman spectroscopy for the BSA in the capsule shells, for the products of their reductive cleavage and for the pristine BSA showed that the BSA molecules in the shells are to an essential extent cross-linked via disulfide bridges between neighboring molecules. Under the assumption that DTT cleaves intra- and intermolecular S–S bonds, the SDS-PAGE additionally revealed the presence of further effects like hydrogen bonds or hydrophobic

interactions stabilizing the protein capsules as well. Therefore, the concept proposed many years ago by Suslick and co-workers is confirmed by experimental evidences for the first time. Moreover, a consistent mechanism for the formation of intermolecular disulfide bonds in capsule shells is proposed that is based on the redistribution of thiol and disulfide groups in BSA under the action of high-energy ultrasound.

During the preparation of the composite microcapsules, the considerable adsorption of BSA on four types of NPs as a necessary prerequisite of capsule formation was confirmed by TGA, zeta potential, EDX and Raman measurements. This adsorption is the result of various interactions between the components, including van der Waals forces, hydrogen bond forces, electrostatic forces and hydrophobic interactions. Successful formation of composite protein-mineral microcapsules loaded with three different oils and shells composed of the aforementioned NPs was supported by cryo SEM images and cryo EDX mapping. Both, the nature of the loaded oil and the type of NPs in the shell, had influence on size and shape of the microcapsules. The examination of the composite capsule with Raman spectroscopy revealed that the BSA molecules adsorbed on the NPs surface in the capsule shell are not cross-linked by intermolecular disulfide bonds. Instead, a Pickering emulsion formation takes place.

The versatility of using composite protein-mineral microcapsules for biomedical application is closely connected to the possibility to widely change their surface chemistry. As a consequence, a surface modification of composite microcapsules through both pre-modification of main components and also the post-modification of the surface of ready composite microcapsules with FITC and APTES was successfully demonstrated.

The mechanical properties of protein and composite protein-mineral microcapsules were compared by using SFM and the Young's moduli were calculated by means of the Reissner model. The results showed that the cross-linked protein microcapsules have higher Young's modulus than the non-cross-linked composite microcapsule meaning that the protein microcapsules are more resistant to elastic deformation. On the other hand, the increase of the NP concentration in the capsule shell lead to an increase of the Young's modulus.

12. Zusammenfassung

Diese Doktorarbeit behandelt die Synthese von Protein- und kompositen Protein-Mineral-Mikrokapseln durch die Anwendung von hochintensivem Ultraschall an der Öl-Wasser-Grenzfläche. Hierbei dienen die Tröpfchen der Öl-in-Wasser-Emulsion, die aufgrund des starken Energieeinsatzes entstehen, als Mikrotemplat für die Bildung von beiden Kapselarten. Während ein System durch BSA-Moleküle stabilisiert wird, die anfänglich als Tensid fungieren und praktisch gleichzeitig als quervernetzbare Bauelemente der Kapselschale, wird das andere System durch verschiedene mit BSA modifizierten Nanopartikeln stabilisiert. Die Modifizierung ermöglicht es den Nanopartikeln bei der Ultraschallbehandlung irreversibel an der Öl-Wasser Grenzfläche zu haften (Bildung einer Pickering Emulsion). Ausgehend von dem zuvor veröffentlichten Herstellungsverfahren von Protein-Mikrokapseln, wurden umfassende Untersuchungen sowohl von allen Synthesestufen als auch von den resultierenden Kapseln durchgeführt und eine plausible Erklärung für den Mechanismus der Kapselbildung wurde vorgestellt. Außerdem wurde die Grenzflächenspannung an der Öl-Wasser-Grenze als Funktion der Zeit, Proteinkonzentration und der chemischen Beschaffenheit des Öls untersucht, um ein besseres Verständnis für die Kinetik der Proteinadsorption zu erhalten.

Während der Bildung der BSA-Mikrokapseln adsorbieren die Proteinmoleküle als Erstes an der O/W-Grenzfläche, entfalten sich dort und bilden ein Netzwerk, das durch hydrophobe Wechselwirkungen und Wasserstoffbrückenbindungen zwischen den benachbarten Molekülen stabilisiert wird und welches anfänglich die Emulsionströpfchen im wässrigen Medium stabilisiert. Gleichzeitig bewirkt die Ultraschallbehandlung die Quervernetzung der BSA-Moleküle über die Bildung von intermolekularen Disulfidbindungen. Dadurch weisen die quervernetzten Protein-Mikrokapseln, verglichen mit den Tröpfchen einer Öl-in-Wasser-Emulsion, die durch einfache Zerkleinerung (z.B. Vortexen) in einer Proteinlösung hergestellt wurde, eine erhöhte Stabilität auf. Die drei verwendeten Öle (Toluol, Miglyol und Minzöl) haben sich für die Herstellung von Protein- und kompositen Protein-Mineral-Mikrokapseln als geeignet erwiesen.

In dieser Doktorarbeit werden die experimentellen Nachweise für die durch Ultraschall induzierte Quervernetzung von BSA in den Schalen der proteinbasierten Mikrokapseln aufgezeigt. Der Vergleich der Ergebnisse von SDS-PAGE, DLS und Raman-Spektroskopie für BSA in den Kapselschalen, für das Produkt ihrer reduktiven Spaltung und für das reine BSA

zeigten, dass die BSA-Moleküle in den Schalen zu einem wesentlichen Teil über Disulfidbrücken zwischen benachbarten Molekülen quervernetzt sind. Unter der Annahme, dass DTT intra- und intermolekulare S–S Bindungen spaltet, wurde durch die SDS-PAGE zusätzlich die Anwesenheit von weiteren Effekten wie Wasserstoffbrückenbindungen oder hydrophoben Wechselwirkungen offenbart, die die Proteinkapseln ebenfalls stabilisieren. Deshalb wurde das Konzept, das vor vielen Jahren von Suslick und seinen Mitarbeitern vorgestellt wurde, zum ersten Mal durch experimentelle Nachweise bestätigt. Außerdem wurde ein konsistenter Mechanismus für die Bildung der intermolekularen Disulfidbindungen in der Kapselschale vorgestellt, der auf der Neuverteilung der Thiol- und Disulfidgruppen in BSA unter der Wirkung von hochenergetischem Ultraschall basiert.

Bei der Herstellung der kompositen Mikrokapseln wurde die Adsorption von BSA an vier Arten von Nanopartikeln als eine notwendige Voraussetzung für die Kapselbildung durch TGA, Zetapotential, EDX und Raman-Messungen bestätigt. Diese Adsorption ist das Resultat von verschiedenen Wechselwirkungen zwischen den Komponenten, darunter van-der-Waals-Kräfte, Wasserstoffbrückenbindungen, elektrostatische Kräfte und hydrophobe Wechselwirkungen. Die erfolgreiche Bildung von kompositen Protein-Mineral-Mikrokapseln, die mit drei verschiedenen Ölen gefüllt wurden und deren Schalen aus den zuvor genannten Nanopartikeln bestehen, wurde durch Kryo-REM-Bilder und Kryo-EDX-Vermessung gestützt. Die Beschaffenheit des Öls und die Art der Nanopartikel in der Schale hatten Einfluss auf die Größe und Form der Mikrokapseln. Die Untersuchung der kompositen Kapseln mit Raman-Spektroskopie zeigte, dass die BSA-Moleküle, die an der Oberfläche der Nanopartikel in der Kapselschale adsorbiert sind, nicht durch intermolekulare Disulfidbindungen quervernetzt sind. Stattdessen findet die Bildung einer Pickering-Emulsion statt.

Die Vielseitigkeit mit der komposite Protein-Mineral-Mikrokapseln für biomedizinische Anwendungen genutzt werden ist eng verbunden mit der Möglichkeit ihre Oberflächenchemie weitgehend zu verändern. Folglich wurde die Oberflächenmodifizierung der kompositen Mikrokapseln durch Vormodifizierung der Hauptbestandteile und auch durch Postmodifizierung der Oberfläche der fertigen kompositen Mikrokapseln mit FITC und APTES erfolgreich demonstriert.

Die mechanischen Eigenschaften der Protein- und kompositen Protein-Mineral-Mikrokapseln wurden durch den Einsatz von SFM verglichen und die Young’s moduli wurden mit Hilfe des Reissner Models berechnet. Die Ergebnisse zeigten, dass die quervernetzten Protein-Mikrokapseln einen höheren Young’s Modulus besitzen als die nicht quervernetzten

kompositen Mikrokapseln. Das bedeutet, dass die Protein-Mikrokapseln widerstandsfähiger gegenüber elastischer Deformation sind. Andererseits führte ein Anstieg der Nanopartikelkonzentration in der Kapselschale zu einem Anstieg des Young's Modulus.

Bibliography

[1] K. D. Hermanson, D. Huemmerich, T. Scheibel and A. R. Bausch, *Adv. Mater.*, 2007, **19**, 1810–1815.

[2] Y. Zhu, W. Tong, C. Gao and H. Möhwald, *J. Mater. Chem.*, 2008, **18**, 1153–1158.

[3] W. Tong and C. Gao, *J. Mater. Chem.*, 2008, **18**, 3799–3812.

[4] A. P. R. Johnston, C. Cortez, A. S. Angelatos and F. Caruso, *Curr. Opin. Colloid Interface Sci.*, 2006, **11**, 203–209.

[5] W. Tong, C. Gao and H. Möhwald, *Colloid Polym. Sci.*, 2008, **286**, 1103–1109.

[6] G. Jutz and A. Böker, *J. Mater. Chem.*, 2010, **20**, 4299–4304.

[7] H. Chen, J. He, H. Tang and C. Yan, *Chem. Mater.*, 2008, **20**, 5894–5900.

[8] H. Maeda, M. Okada, S. Fujii, Y. Nakamura and T. Furuzono, *Langmuir*, 2010, **26**, 13727–13731.

[9] U. Doering, D. Grigoriev, K. Tapio, S. Rosencrantz, R. R. Rosencrantz, I. Bald and A. Böker, *RSC Adv.*, 2021, **11**, 16152–16157.

[10] D. Lee and D. A. Weitz, *Adv. Mater.*, 2008, **20**, 3498–3503.

[11] I. Akartuna, E. Tervoort, A. R. Studart and L. J. Gauckler, *Langmuir*, 2009, **25**, 12419–12424.

[12] S. Gouin, *Trends Food Sci. Technol.*, 2004, **15**, 330–347.

[13] G. Nelson, *Int. J. Pharm.*, 2002, **242**, 55–62.

[14] R. Gref, Y. Minamitake, M. T. Peracchia, V. Trubetskoy, V. Torchilin and R. Langer, *Science*, 1994, **263**, 1600–1603.

[15] R. Akiyama and S. Kobayashi, *Chem. Rev.*, 2009, **109**, 594–642.

[16] Y. Han, M. Fuji, D. Shchukin, H. Möhwald and M. Takahashi, *Cryst. Growth Des.*, 2009, **9**, 3771–3775.

[17] Y. Cai, H. Pan, X. Xu, Q. Hu, L. Li and R. Tang, *Chem. Mater.*, 2007, **19**, 3081–3083.

[18] D. W. Green, S. Mann and R. O. C. Oreffo, *Soft Matter*, 2006, **2**, 732–737.

[19] K. Samborska, S. Boostani, M. Geranpour, H. Hosseini, C. Dima, S. Khoshnoudi-Nia, H. Rostamabadi, S. R. Falsafi, R. Shaddel, S. Akbari-Alavijeh and S. M. Jafari, *Trends Food Sci. Technol.*, 2021, **108**, 297–325.

[20] K. S. Suslick and M. W. Grinstaff, *J. Am. Chem. Soc.*, 1990, **112**, 7807–7809.

[21] S. Avivi, I. Felner, I. Novik and A. Gedanken, *Biochim. Biophys. Acta*, 2001, **1527**, 123–129.

[22] Avivi, Y. Nitzan, R. Dror and A. Gedanken, *J. Am. Chem. Soc.*, 2003, **125**, 15712–15713.

[23] K. S. Suslick and G. J. Price, *Annu. Rev. Mater. Sci.*, 1999, **29**, 295–326.

[24] A. Gedanken, *Chem. - Eur. J.*, 2008, **14**, 3840–3853.

[25] X. Cui, B. Wang, S. Zhong, Z. Li, Y. Han, H. Wang and H. Moehwald, *Colloid Polym. Sci.*, 2013, **291**, 2271–2278.

[26] J. Rae, M. Ashokkumar, O. Eulaerts, C. von Sonntag, J. Reisse and F. Grieser, *Ultrason. Sonochem.*, 2005, **12**, 325–329.

[27] C. Little, M. El-Sharif and M. J. Hepher, *Ultrason. Sonochem.*, 2007, **14**, 375–379.

[28] Q. Ye, M. Biviano, S. Mettu, M. Zhou, R. Dagastine and M. Ashokkumar, *RSC Adv.*, 2016, **6**, 106130–106140.

[29] U. Angel (Shimanovich), D. Matas, S. Michaeli, A. Cavaco-Paulo and A. Gedanken, *Chem. - Eur. J.*, 2010, **16**, 2108–2114.

[30] Y. Han, D. Radziuk, D. Shchukin and H. Moehwald, *Macromol. Rapid Commun.*, 2008, **29**, 1203–1207.

[31] A. Schulz, B. M. Liebeck, D. John, A. Heiss, T. Subkowski and A. Böker, *J. Mater. Chem.*, 2011, **21**, 9731–9736.

[32] S. Avivi and A. Gedanken, *Biochem. J.*, 2002, **366**, 705–707.

[33] R. Silva, H. Ferreira, N. G. Azoia, U. Shimanovich, G. Freddi, A. Gedanken and A. Cavaco-Paulo, *Mol. Pharmaceutics*, 2012, **9**, 3079–3088.

[34] U. Shimanovich, G. J. L. Bernardes, T. P. J. Knowles and A. Cavaco-Paulo, *Chem. Soc. Rev.*, 2014, **43**, 1361–1371.

[35] K. S. Suslick, M. W. Grinstaff, K. J. Kolbeck and M. Wong, *Ultrason. Sonochem.*, 1994, **1**, S65–S68.

[36] M. W. Grinstaff and K. S. Suslick, *Proc. Natl. Acad. Sci. U. S. A.*, 1991, **88**, 7708–7710.

[37] S. S. Behrens, *J. Mater. Chem.*, 2008, **18**, 3788–3798.

[38] I. Yamashita, *J. Mater. Chem.*, 2008, **18**, 3813–3820.

[39] L. Figura and A. A. Teixeira, *Food physics: physical properties-measurement and applications*, Springer, Berlin, 2007.

[40] A. I. Rusanov and V. A. Prokhorov, *Interfacial tensiometry*, Elsevier, Amsterdam, 1996.

[41] P. Atkins and J. de Paula, *Atkins' Physical Chemistry*, Oxford University Press, Oxford, 2006.

[42] L. L. Schramm, *Emulsions, foams, and suspensions: fundamentals and applications*, Wiley-VCH Verlag GmbH & Co. KGaA, Weinheim, 2006.

[43] S. Tcholakova, N. D. Denkov and A. Lips, *Phys. Chem. Chem. Phys.*, 2008, **10**, 1608–1627.

[44] H. Hoffmann and M. Reger, *Adv. Colloid Interface Sci.*, 2014, **205**, 94–104.

[45] S. S. Dukhin, G. Kretzschmar and R. Miller, *Dynamics of adsorption at liquid interfaces: theory, experiment, application*, Elsevier, Amsterdam, 1995.

[46] M. J. Richter, P. van Rijn and A. Böker, in *Bio-Synthetic Hybrid Materials and Bionanoparticles: A Biological Chemical Approach Towards Material Science*, ed. A. Böker and P. van Rijn, The Royal Society of Chemistry, Cambridge, 2015, ch. 6, pp. 123–145.

[47] G. Yampolskaya and D. Platikanov, *Adv. Colloid Interface Sci.*, 2006, **128–130**, 159–183.

[48] V. B. Fainerman, E. H. Lucassen-Reynders and R. Miller, *Adv. Colloid Interface Sci.*, 2003, **106**, 237–259.

[49] C. J. Beverung, C. J. Radke and H. W. Blanch, *Biophys. Chem.*, 1999, **81**, 59–80.

[50] Y. F. Yano, *J. Phys.: Condens. Matter*, 2012, **24**, 503101.

[51] G. Serrien, G. Geeraerts, L. Ghosh and P. Joos, *Colloids Surf.*, 1992, **68**, 219–233.

[52] B. P. Binks and T. S. Horozov, in *Colloidal Particles at Liquid Interfaces*, ed. B. P. Binks and T. S. Horozov, Cambridge University Press, Cambridge, 2006, ch. 1, pp. 1–74.

[53] Y. Chevalier and M.-A. Bolzinger, *Colloids Surf., A*, 2013, **439**, 23–34.

[54] B. P. Binks and S. O. Lumsdon, *Langmuir*, 2000, **16**, 8622–8631.

[55] B. P. Binks, *Curr. Opin. Colloid Interface Sci.*, 2002, **7**, 21–41.

[56] R. Aveyard, B. P. Binks and J. H. Clint, *Adv. Colloid Interface Sci.*, 2003, **100–102**, 503–546.

[57] S. U. Pickering, *J. Chem. Soc., Trans.*, 1907, **91**, 2001–2021.

[58] N. Popp, S. Kutuzov and A. Böker, in *Complex Macromolecular Systems II*, ed. A. H. E. Müller and H.-W. Schmidt, Springer Berlin Heidelberg, Berlin, Heidelberg, 2010, ch. 2, pp. 39–58.

[59] T. N. Hunter, R. J. Pugh, G. V. Franks and G. J. Jameson, *Adv. Colloid Interface Sci.*, 2008, **137**, 57–81.

[60] J. Koolman and K.-H. Röhm, *Taschenatlas der Biochemie*, Georg Thieme Verlag, Stuttgart, 2003.

[61] G. Löffler, *Basiswissen Biochemie: mit Pathobiochemie*, Springer-Verlag, Heidelberg, 2008.

[62] D. L. Nelson and M. M. Cox, *Lehninger Biochemie*, Springer, Heidelberg, 2009.

[63] RCSB Protein Data Bank, https://www.rcsb.org/3d-view/3V03/1, accessed December 2021.

[64] T. E. Creighton, *The encyclopedia of molecular biology. Volume 4*, Wiley, New York, 1999.

[65] T. Peters, in *Advances in Protein Chemistry*, ed. C. B. Anfinsen, J. T. Edsall and F. M. Richards, Academic Press, 1985, ch. 3, pp. 161–245.

[66] V. Uskoković and D. P. Uskoković, *J. Biomed. Mater. Res. Part B Appl. Biomater.*, 2011, **96**, 152–191.

[67] S. V. Dorozhkin, *Biomatter*, 2011, **1**, 121–164.

[68] L. Wang and G. H. Nancollas, *Chem. Rev.*, 2008, **108**, 4628–4669.

[69] M. J. Olszta, X. Cheng, S. S. Jee, R. Kumar, Y.-Y. Kim, M. J. Kaufman, E. P. Douglas and L. B. Gower, *Mater. Sci. Eng. R Rep.*, 2007, **58**, 77–116.

[70] V. P. Orlovskii, V. S. Komlev and S. M. Barinov, *Inorg. Mater.*, 2002, **38**, 973–984.

[71] J. Venugopal, M. P. Prabhakaran, Y. Zhang, S. Low, A. T. Choon and S. Ramakrishna, *Phil. Trans. R. Soc. A.*, 2010, **368**, 2065–2081.

[72] Y. Cai and R. Tang, *J. Mater. Chem.*, 2008, **18**, 3775–3787.

[73] S. Bose and S. Tarafder, *Acta Biomater.*, 2012, **8**, 1401–1421.

[74] Z. Evis and T. J. Webster, *Adv. Appl. Ceram.*, 2011, **110**, 311–321.

[75] A. Corami, S. Mignardi and V. Ferrini, *J. Colloid Interface Sci.*, 2008, **317**, 402–408.

[76] N. Phonthammachai, Z. Ziyi, G. Jun, H. Y. Fan and T. J. Whitea, *Gold Bull.*, 2008, **41**, 42–50.

[77] W. Chen, Z. Huang, Y. Liu and Q. He, *Catal. Commun.*, 2008, **9**, 516–521.

[78] M. I. Domínguez, F. Romero-Sarria, M. A. Centeno and J. A. Odriozola, *Appl. Catal., B*, 2009, **87**, 245–251.

[79] J. L. Xu, K. A. Khor, Z. L. Dong, Y. W. Gu, R. Kumar and P. Cheang, *Mater. Sci. Eng. A*, 2004, **374**, 101–108.

[80] P. Luo and T. G. Nieh, *Mater. Sci. Eng. C*, 1995, **3**, 75–78.

[81] Y. Yang, K.-H. Kim and J. L. Ong, *Biomaterials*, 2005, **26**, 327–337.

[82] S. Xu, J. Long, L. Sim, C. H. Diong and K. Ostrikov, *Plasma Processes Polym.*, 2005, **2**, 373–390.

[83] S. Pramanik, A. K. Agarwal, K. N. Rai and A. Garg, *Ceram. Int.*, 2007, **33**, 419–426.

[84] M. H. Fathi and A. Hanifi, *Mater. Lett.*, 2007, **61**, 3978–3983.

[85] Y. Fang, D. K. Agrawal, D. M. Roy, R. Roy and P. W. Brown, *J. Mater. Res.*, 1992, **7**, 2294–2298.

[86] I. Nikčević, V. Jokanović, M. Mitrić, Z. Nedić, D. Makovec and D. Uskoković, *J. Solid State Chem.*, 2004, **177**, 2565–2574.

[87] K. Teshima, S. Lee, M. Sakurai, Y. Kameno, K. Yubuta, T. Suzuki, T. Shishido, M. Endo and S. Oishi, *Cryst. Growth Des.*, 2009, **9**, 2937–2940.

[88] W.-J. Shih, Y.-F. Chen, M.-C. Wang and M.-H. Hon, *J. Cryst. Growth*, 2004, **270**, 211–218.

[89] K. Zhu, K. Yanagisawa, R. Shimanouchi, A. Onda, K. Kajiyoshi and J. Qiu, *Mater. Res. Bull.*, 2009, **44**, 1392–1396.

[90] X. Li, G. Koller, J. Huang, L. Di Silvio, T. Renton, M. Esat, W. Bonfield and M. Edirisinghe, *J. R. Soc. Interface*, 2010, **7**, 189–197.

[91] S. Sarda, M. Heughebaert and A. Lebugle, *Chem. Mater.*, 1999, **11**, 2722–2727.

[92] Z. Evis, *Ceram. Int.*, 2007, **33**, 987–991.

[93] R. Myers, *The 100 Most Important Chemical Compounds: A Reference Guide*, Greenwood Press, Westport, 2007.

[94] E. Wiberg and N. Wiberg, *Inorganic Chemistry*, Academic Press, Cambridge, 2001.

[95] Y. Zhang, B. Y. W. Hsu, C. Ren, X. Li and J. Wang, *Chem. Soc. Rev.*, 2015, **44**, 315–335.

[96] M. Fricke and D. Volkmer, in *Biomineralization I: Crystallization and Self-Organization Process*, ed. K. Naka, Springer Berlin Heidelberg, Berlin, Heidelberg, 2007, ch. 1, pp. 1–41.

[97] N. A. J. M. Sommerdijk and G. de With, *Chem. Rev.*, 2008, **108**, 4499–4550.

[98] E. N. Maslen, V. A. Streltsov and N. R. Streltsova, *Acta Cryst. B*, 1993, **49**, 636–641.

[99] J. Wang and U. Becker, *Am. Mineral.*, 2009, **94**, 380–386.

[100] H. Meyer, *Z. Kristallogr. Cryst. Mater.*, 1969, **128**, 183–212.

[101] S. R. Kamhi, *Acta Cryst.*, 1963, **16**, 770–772.

[102] A. D. Negro and L. Ungaretti, *Am. Mineral.*, 1971, **56**, 768–772.

[103] J. P. Lorimer and T. J. Mason, *Chem. Soc. Rev.*, 1987, **16**, 239–274.

[104] T. J. Mason and J. P. Lorimer, *Applied sonochemistry: the uses of power ultrasound in chemistry and processing*, Wiley-VCH, Weinheim, 2002.

[105] Y. Wei, Y. Li, N. Zhang, G. Shi and L. Jin, *Ultrason. Sonochem.*, 2010, **17**, 17–20.

[106] N. A. Ross, R. R. MacGregor and R. A. Bartsch, *Tetrahedron*, 2004, **60**, 2035–2041.

[107] N. A. Ross and R. A. Bartsch, *J. Org. Chem.*, 2003, **68**, 360–366.

[108] J. Kost, K. Leong and R. Langer, *Proc. Natl. Acad. Sci. U. S. A.*, 1989, **86**, 7663–7666.

[109] C. L. Geiger, N. E. Ruiz, C. A. Clausen, D. R. Reinhart and J. W. Quinn, *Water Res.*, 2002, **36**, 1342–1350.

[110] R. W. Wood and A. L. Loomis, *Lond. Edinb. Dublin Philos. Mag. J. Sci.*, 1927, **4**, 417–436.

[111] V. Zin, B. G. Pollet and M. Dabalà, *Electrochim. Acta*, 2009, **54**, 7201–7206.

[112] M. Dabala, B. Pollet, V. Zin, E. Campadello and T. J. Mason, *J. Appl. Electrochem.*, 2008, **38**, 395–402.

[113] A. Gedanken, *Ultrason. Sonochem.*, 2004, **11**, 47–55.

[114] D. Radziuk, D. Shchukin and H. Möhwald, *J. Phys. Chem. C*, 2008, **112**, 2462–2468.

[115] A. E. Crawford, *Ultrasonics*, 1963, **1**, 65–69.

[116] D. G. Shchukin and H. Möhwald, *Phys. Chem. Chem. Phys.*, 2006, **8**, 3496–3506.

[117] T. Leighton, *The acoustic bubble*, Academic press, Cambridge, 2012.

[118] L. Rayleigh, *Lond. Edinb. Dublin Philos. Mag. J. Sci.*, 1917, **34**, 94–98.

[119] K. S. Suslick, *Sci. Am.*, 1989, **260**, 80–87.

[120] K. Makino, M. M. Mossoba and P. Riesz, *J. Phys. Chem*, 1983, **87**, 1369–1377.

[121] N. Serpone and P. Colarusso, *Res. Chem. Intermed.*, 1994, **20**, 635–679.

[122] K. S. Suslick and L. A. Crum, in *Encyclopedia of Acoustics*, ed. M. J. Crocker, Wiley-Interscience, New York, 1997, ch. 26, pp. 271–282.

[123] J. Berlan and T. J. Mason, *Ultrasonics*, 1992, **30**, 203–212.

[124] T. Kimura, T. Sakamoto, J.-M. Leveque, H. Sohmiya, M. Fujita, S. Ikeda and T. Ando, *Ultrason. Sonochem.*, 1996, **3**, S157–S161.

[125] W. B. McNamara, Y. T. Didenko and K. S. Suslick, *Nature*, 1999, **401**, 772–775.

[126] L. A. Crum, *J. Acoust. Soc. Am.*, 1980, **68**, 203–211.

[127] J. Lee, S. E. Kentish and M. Ashokkumar, *J. Phys. Chem. B*, 2005, **109**, 5095–5099.

[128] M. S. Plesset, *J. Basic Eng.*, 1970, **92**, 807–813.

[129] V. A. Borissenok, *Phys. Lett. A*, 2008, **372**, 3496–3500.

[130] M. W. A. Kuijpers, D. van Eck, M. F. Kemmere and J. T. F. Keurentjes, *Science*, 2002, **298**, 1969–1971.

[131] R. E. Vandenbroucke, I. Lentacker, J. Demeester, S. C. De Smedt and N. N. Sanders, *J. Control. Release*, 2008, **126**, 265–273.

[132] S. Na, Y. Park, A. Hwang, J. Ha, Y. Kim and J. Khim, *Jpn. J. Appl. Phys.*, 2007, **46**, 4775–4778.

[133] M. A. Borden, D. E. Kruse, C. F. Caskey, Z. Shukui, P. A. Dayton and K. W. Ferrara, *IEEE Trans. Ultrason. Ferroelectr. Freq. Control*, 2005, **52**, 1992–2002.

[134] F. Yang, L. Li, Y. Li, Z. Chen, J. Wu and N. Gu, *Phys. Med. Biol.*, 2008, **53**, 6129–6141.

[135] Y. Liao, Q. Wang, H. Xia, X. Xu, S. M. Baxter, R. V. Slone, S. Wu, G. Swift and D. G. Westmoreland, *J. Polym. Sci. A Polym. Chem.*, 2001, **39**, 3356–3364.

[136] H. Xia, C. Zhang and Q. Wang, *J. Appl. Polym. Sci.*, 2001, **80**, 1130–1139.

[137] K. Arakawa, K. Hagisawa, H. Kusano, S. Yoneyama, A. Kurita, T. Arai, M. Kikuchi, I. Sakata, S.-i. Umenura and F. Ohsuzu, *Circulation*, 2002, **105**, 149–151.

[138] K. Tachibana and S. Tachibana, *Echocardiography*, 2001, **18**, 323–328.

[139] M. R. Hoffmann, I. Hua and R. Höchemer, *Ultrason. Sonochem.*, 1996, **3**, S163–S172.

[140] H. Destaillats, H.-M. Hung and M. R. Hoffmann, *Environ. Sci. Technol.*, 2000, **34**, 311–317.

[141] P. Théron, P. Pichat, C. Petrier and C. Guillard, *Water Sci. Technol.*, 2001, **44**, 263–270.

[142] R. A. Caruso, M. Ashokkumar and F. Grieser, *Colloids Surf., A*, 2000, **169**, 219–225.

[143] K. Barbour, M. Ashokkumar, R. A. Caruso and F. Grieser, *J. Phys. Chem. B*, 1999, **103**, 9231–9236.

[144] Y. Mizukoshi, R. Oshima, Y. Maeda and Y. Nagata, *Langmuir*, 1999, **15**, 2733–2737.

[145] J. Z. Sostaric, R. A. Caruso-Hobson, P. Mulvaney and F. Grieser, *J. Chem. Soc., Faraday Trans.*, 1997, **93**, 1791–1795.

[146] E. B. Flint and K. S. Suslick, *Science*, 1991, **253**, 1397–1399.

[147] G. E. Vazquez and S. J. Putterman, *Phys. Rev. Lett.*, 2000, **85**, 3037–3040.

[148] P. Jarman, *Proc. Phys. Soc.*, 1959, **73**, 628–640.

[149] Y. G. Adewuyi, *Ind. Eng. Chem. Res.*, 2001, **40**, 4681–4715.

[150] Y. T. Didenko, W. B. McNamara and K. S. Suslick, *Phys. Rev. Lett.*, 2000, **84**, 777–780.

[151] D. Peters, *J. Mater. Chem.*, 1996, **6**, 1605–1618.

[152] T. J. Mason, *Practical sonochemistry : user's guide to applications in chemistry and chemical engineering*, Ellis Horwood, London, 1991.

[153] Y.-Y. Yang, T.-S. Chung, X.-L. Bai and W.-K. Chan, *Chem. Eng. Sci.*, 2000, **55**, 2223–2236.

[154] X. Huang and W. J. Brittain, *Macromolecules*, 2001, **34**, 3255–3260.

[155] P. J. Dowding, R. Atkin, B. Vincent and P. Bouillot, *Langmuir*, 2005, **21**, 5278–5284.

[156] A. Maschke, C. Becker, D. Eyrich, J. Kiermaier, T. Blunk and A. Göpferich, *Eur. J. Pharm. Biopharm.*, 2007, **65**, 175–187.

[157] G. Jiang, B. C. Thanoo and P. P. DeLuca, *Pharm. Dev. Technol.*, 2002, **7**, 391–399.

[158] R. Silva, H. Ferreira and A. Cavaco-Paulo, *Biomacromolecules*, 2011, **12**, 3353–3368.

[159] H. Xu, B. W. Zeiger and K. S. Suslick, *Chem. Soc. Rev.*, 2013, **42**, 2555–2567.

[160] D. O. Grigoriev and R. Miller, *Curr. Opin. Colloid Interface Sci.*, 2009, **14**, 48–59.

[161] O. Grinberg, A. Gedanken, C. R. Patra, S. Patra, P. Mukherjee and D. Mukhopadhyay, *Acta Biomater.*, 2009, **5**, 3031–3037.

[162] O. Grinberg, M. Hayun, B. Sredni and A. Gedanken, *Ultrason. Sonochem.*, 2007, **14**, 661–666.

[163] O. P. Tiourina and G. B. Sukhorukov, *Int. J. Pharm.*, 2002, **242**, 155–161.

[164] Z. An, H. Möhwald and J. Li, *Biomacromolecules*, 2006, **7**, 580–585.

[165] D. Mertz, P. Tan, Y. Wang, T. K. Goh, A. Blencowe and F. Caruso, *Adv. Mater.*, 2011, **23**, 5668–5673.

[166] D. Patra, A. Sanyal and V. M. Rotello, *Chem. Asian J.*, 2010, **5**, 2442–2453.

[167] J. Wu and G.-H. Ma, *Small*, 2016, **12**, 4633–4648.

[168] K. L. Thompson, M. Williams and S. P. Armes, *J. Colloid Interface Sci.*, 2015, **447**, 217–228.

[169] F. Caruso, H. Lichtenfeld, M. Giersig and H. Möhwald, *J. Am. Chem. Soc.*, 1998, **120**, 8523–8524.

[170] L. Zhang and A. Eisenberg, *Science*, 1995, **268**, 1728–1731.

[171] J. Song, X. Yang, O. Jacobson, P. Huang, X. Sun, L. Lin, X. Yan, G. Niu, Q. Ma and X. Chen, *Adv. Mater.*, 2015, **27**, 4910–4917.

[172] J. He, X. Huang, Y.-C. Li, Y. Liu, T. Babu, M. A. Aronova, S. Wang, Z. Lu, X. Chen and Z. Nie, *J. Am. Chem. Soc.*, 2013, **135**, 7974–7984.

[173] J. He, P. Zhang, T. Babu, Y. Liu, J. Gong and Z. Nie, *Chem. Commun.*, 2013, **49**, 576–578.

[174] E. M. Slayter and H. S. Slayter, *Light and Electron Microscopy*, Cambridge University Press, Cambridge, 1994.

[175] D. Gerlach, *Das Lichtmikroskop*, Thieme, Stuttgart, 1985.

[176] R. F. Egerton, *Physical Principles of Electron Microscopy*, Springer, Berlin, 2016.

[177] D. Shindo and T. Oikawa, *Analytical Eletron Microscopy for Material Science*, Springer, Tokyo, 2002.

[178] H. Krischer and B. Koppelhuber-Bitschnau, *Röntgenstrukturnalyse und Rietveldmethode*, vieweg, Braunschweig, 1994.

[179] S.-L. Zhang, *Raman Spectroscopy and its Application in Nanostructures*, Wiley, Chichester, 2012.

[180] B. Schrader, *Infrared and Raman Spectroscopy*, VCH, Weinheim, 1995.

[181] R. Bottom, in *Principles and Applications of Thermal Analysis*, ed. P. Gabbott, Blackwell Publishing, Oxford, 1st edn, 2008, ch. 3, pp. 87–118.

[182] Krüss, https://www.kruss-scientific.com/en/know-how/glossary/pendant-drop, accessed November 2021.

[183] J. D. Berry, M. J. Neeson, R. R. Dagastine, D. Y. C. Chan and R. F. Tabor, *J. Colloid Interface Sci.*, 2015, **454**, 226–237.

[184] N. Bagalkot, A. A. Hamouda and O. M. Isdahl, *MethodsX*, 2018, **5**, 676–683.

[185] J. Stetefeld, S. A. McKenna and T. R. Patel, *Biophys. Rev.*, 2016, **8**, 409–427.

[186] I. N. McCave, R. J. Bryant, H. F. Cook and C. A. Coughanowr, *J. Sediment. Res.*, 1986, **56**, 561–564.

[187] Z. Ma, H. G. Merkus, J. G. A. E. de Smet, C. Heffels and B. Scarlett, *Powder Technol.*, 2000, **111**, 66–78.

[188] R. Xu, *Particle characterization: light scattering methods*, Kluwer Academic Publishers, Dordrecht, 2002.

[189] S. Bhattacharjee, *J. Control. Release*, 2016, **235**, 337–351.

[190] Q. Shi and G. Jackowski, in *Gel Electrophoresis of Proteins: A Practical Approach*, ed. B. D. Hames, Oxford University Press, Oxford, 3, 1998, ch. 1, pp. 1–52.

[191] A. Dabrik and P. Laidler, in *Proteomics: Introduction to Methods and Applications*, ed. A. Kraj and J. Silberring, John Wiley and Sons, Inc., Hoboken, 1, 2008, ch. 4.1, pp. 33–42.

[192] L. Zhou, M. Cai, T. Tong and H. Wang, *Sensors*, 2017, **17**, 938.

[193] K. J. Liu, M. W. Grinstaff, J. Jiang, K. S. Suslick, H. M. Swartz and W. Wang, *Biophys. J.*, 1994, **67**, 896-901.

[194] A. H. Demond and A. S. Lindner, *Environ. Sci. Technol.*, 1993, **27**, 2318–2331.

[195] N. Ghouchi Eskandar, S. Simovic and C. A. Prestidge, *Phys. Chem. Chem. Phys.*, 2007, **9**, 6426–6434.

[196] C. Arneodo, A. Baszkin, J. P. Benoit, R. Fellous and C. Thies, *Colloids Surf.*, 1988, **34**, 159–169.

[197] A. Dan, R. Wüstneck, J. Krägel, E. V. Aksenenko, V. B. Fainerman and R. Miller, *Food Hydrocolloids*, 2014, **34**, 193–201.

[198] Y. Zhang, Y. Li, S. Li, H. Zhang and H. Ma, *Molecules*, 2018, **23**, 1–13.

[199] T. Peters and R. C. Feldhoff, *Biochemistry*, 1975, **14**, 3384–3391.

[200] R. C. Feldhoff and T. Peters, *Biochemistry*, 1975, **14**, 4508–4514.

[201] P. Restani, A. Fiocchi, B. Beretta, T. Velonà, M. Giovannini and C. L. Galli, *Lett. Pept. Sci.*, 1997, **4**, 269–273.

[202] P. Restani, T. Velonà, A. Plebani, A. G. Ugazio, C. Poiesi, A. Muraro and C. L. Galli, *Clin. Exp. Allergy*, 1995, **25**, 651–658.

[203] B. T. Kurien and R. H. Scofield, *Methods Mol. Biol.*, 2012, **869**, 471–479.

[204] S. M. Alonso Villela, H. Kraïem, B. Bouhaouala-Zahar, C. Bideaux, C. A. Aceves Lara and L. Fillaudeau, *MicrobiologyOpen*, 2020, **9**, 1–8.

[205] B. Liu, Y. Pang, R. Bouhenni, E. Duah, S. Paruchuri and L. McDonald, *Chem. Commun.*, 2015, **51**, 11060–11063.

[206] L.-J. Lai, F.-L. Huang, P.-H. Cheng and R. Y. Chiou, *Int. J. Clin. Nutr. Diet.*, 2017, **3**, 1–5.

[207] C. Burgard, PhD thesis, University of Saarland, 2009.

[208] Bio-Rad, https://www.bio-rad.com/webroot/web/pdf/lsr/literature/Bulletin_6040.pdf, accessed March 2021.

[209] Malvern Panalytical, https://www.malvernpanalytical.com/en/academia/research-themes/biological-medical-science/index.html, accessed March 2021.

[210] Malvern Panalytical, https://www.malvernpanalytical.com/en/learn/knowledge-center/application-notes/AN120917SEC-LS-DLSQuantificationProteinAggregates, accessed March 2021.

[211] H. P. Erickson, *Biol. Proced. Online*, 2009, **11**, 32–51.

[212] Malvern Panalytical, https://www.malvernpanalytical.com/en/learn/knowledge-center/application-notes/AN101104ZetasizerAPSEliminatesCrossContamination, accessed March 2021.

[213] Malvern Panalytical, https://www.malvernpanalytical.com/en/learn/knowledge-center/application-notes/AN110707ProteinCharacterisationZetasizerMicroV, accessed March 2021.

[214] U. Nobbmann, in *Mesoscale Phenomena in Fluid Systems*, ed. F. Case and P. Alexandridis, American Chemical Society, Washington, 2003, ch. 4, pp. 44–59.

[215] N. N. Brandt, A. Y. Chikishev, A. A. Mankova and I. K. Sakodynskaya, *J. Biomed. Opt.*, 2015, **20**, 1–6.

[216] C.-H. Wang, C.-C. Huang, L.-L. Lin and W. Chen, *J. Raman Spectrosc.*, 2016, **47**, 940–947.

[217] M. Liang, V. Y. T. Chen, H.-L. Chen and W. Chen, *Talanta*, 2006, **69**, 1269–1277.

[218] S. Hirorau, G. Akikatsu and M. Tatsuo, *Chem. Lett.*, 1972, **1**, 83–86.

[219] S. Hiromu, G. Akikatsu and M. Tatsuo, *Bull. Chem. Soc. Jpn.*, 1973, **46**, 3407–3411.

[220] N. N. Brandt, A. Y. Chikishev, A. V. Golovin, V. N. Kruzhilin and A. O. Zalevsky, *Biomed. Spectrosc. Imaging*, 2014, **3**, 287–292.

[221] H. E. Van Wart and H. A. Scheraga, *J. Phys. Chem*, 1976, **80**, 1823–1832.

[222] H. E. Van Wart and H. A. Scheraga, *J. Phys. Chem*, 1976, **80**, 1812–1823.

[223] H. E. Van Wart, F. Cardinaux and H. A. Scheraga, *J. Phys. Chem*, 1976, **80**, 625–630.

[224] N. Biswas, A. J. Waring, F. J. Walther and R. A. Dluhy, *Biochim. Biophys. Acta*, 2007, **1768**, 1070–1082.

[225] J. R. Maher, M. Takahata, H. A. Awad and A. J. Berger, *J. Biomed. Opt.*, 2011, **16**, 1–6.

[226] N. Howell and E. Li-Chan, *Int. J. Food Sci. Technol.*, 1996, **31**, 439–451.

[227] Y. X. Pang and X. Bao, *J. Eur. Ceram. Soc.*, 2003, **23**, 1697–1704.

[228] V. M. Rusu, C.-H. Ng, M. Wilke, B. Tiersch, P. Fratzl and M. G. Peter, *Biomaterials*, 2005, **26**, 5414–5426.

[229] P. Scherrer, *Göttinger Nachrichten Math. Phys.*, 1918, **2**, 98–100.

[230] S. Koutsopoulos, *J. Biomed. Mater. Res.*, 2002, **62**, 600–612.

[231] V. V. Nosenko, A. M. Yaremko, V. M. Dzhagan, I. P. Vorona, Y. A. Romanyuk and I. V. Zatovsky, *J. Raman Spectrosc.*, 2016, **47**, 726–730.

[232] L. M. Rodríguez-Lorenzo, M. Vallet-Regí and J. M. F. Ferreira, *Biomaterials*, 2001, **22**, 1847–1852.

[233] V. Uskoković, S. Ghosh and V. M. Wu, *J. Mater. Chem. B*, 2017, **5**, 6065–6080.

[234] C. M. Botelho, M. A. Lopes, I. R. Gibson, S. M. Best and J. D. Santos, *J. Mater. Sci.: Mater. Med.*, 2002, **13**, 1123–1127.

[235] X. Yao, S. Tan and D. Jiang, *J. Mater. Sci.: Mater. Med.*, 2005, **16**, 161–165.

[236] K. Kandori, S. Sawai, Y. Yamamoto, H. Saito and T. Ishikawa, *Colloids Surf.*, 1992, **68**, 283–289.

[237] M. Lelli, N. Roveri, C. Marzano, J. D. Hoeschele, A. Curci, N. Margiotta, V. Gandin and G. Natile, *Dalton Trans.*, 2016, **45**, 13187–13195.

[238] G. S. Deshmukh, S. U. Pathak, D. R. Peshwe and J. D. Ekhe, *Bull. Mater. Sci.*, 2010, **33**, 277–284.

[239] I. Galan, F. P. Glasser and C. Andrade, *J. Therm. Anal. Calorim.*, 2013, **111**, 1197–1202.

[240] S. Shimabayashi, Y. Tanizawa and K. Ishida, *Chem. Pharm. Bull.*, 1991, **39**, 2183–2188.

[241] D. T. H. Wassell, R. C. Hall and G. Embery, *Biomaterials*, 1995, **16**, 697–702.

[242] J. M. Peula-Garcia, R. Hidaldo-Alvarez and F. J. de las Nieves, *Colloid Polym. Sci.*, 1997, **275**, 198–202.

[243] J. Chen, T. He, W. Wu, D. Cao, J. Yun and C. K. Tan, *Colloids Surf., A*, 2004, **232**, 163–168.

[244] E. Song, D. Kim, B. J. Kim and J. Lim, *Colloids Surf., A*, 2014, **461**, 1–10.

[245] M. Iosin, V. Canpean and S. Astilean, *J. Photochem. Photobiol., A*, 2011, **217**, 395–401.

[246] Q. Li, B. Mihailova, D. Creaser and J. Sterte, *Microporous Mesoporous Mater.*, 2001, **43**, 51–59.

[247] C. E. Giacomelli and W. Norde, *J. Colloid Interface Sci.*, 2001, **233**, 234–240.

[248] W. Norde and J. P. Favier, *Colloids Surf.*, 1992, **64**, 87–93.

[249] S. K. Swain and D. Sarkar, *Appl. Surf. Sci.*, 2013, **286**, 99–103.

[250] N. Barbero, C. Barolo and G. Viscardi, *World J. Chem. Educ.*, 2016, **4**, 80–85.

[251] R. M. Pasternack, S. Rivillon Amy and Y. J. Chabal, *Langmuir*, 2008, **24**, 12963–12971.

[252] R. G. Acres, A. V. Ellis, J. Alvino, C. E. Lenahan, D. A. Khodakov, G. F. Metha and G. G. Andersson, *J. Phys. Chem. C*, 2012, **116**, 6289–6297.

[253] E. T. Vandenberg, L. Bertilsson, B. Liedberg, K. Uvdal, R. Erlandsson, H. Elwing and I. Lundström, *J. Colloid Interface Sci.*, 1991, **147**, 103–118.

[254] C.-H. Chiang, N.-I. Liu and J. L. Koenig, *J. Colloid Interface Sci.*, 1982, **86**, 26–34.

[255] E. Glynos, V. Sboros and V. Koutsos, *Mater. Sci. Eng. B*, 2009, **165**, 231–234.

[256] E. Reissner, *J. Math. Phys.*, 1946, **25**, 80–85.

[257] E. Reissner, *J. Math. Phys.*, 1946, **25**, 279–300.

[258] T. A. Kolesnikova, D. A. Gorin, P. Fernandes, S. Kessel, G. B. Khomutov, A. Fery, D. G. Shchukin and H. Möhwald, *Adv. Funct. Mater.*, 2010, **20**, 1189–1195.

[259] M. F. Bédard, A. Munoz-Javier, R. Mueller, P. del Pino, A. Fery, W. J. Parak, A. G. Skirtach and G. B. Sukhorukov, *Soft Matter*, 2009, **5**, 148–155.

[260] C. de Loubens, J. Deschamps, M. Georgelin, A. Charrier, F. Edwards-Levy and M. Leonetti, *Soft Matter*, 2014, **10**, 4561–4568.

[261] J. A. Greenwood and J. H. Tripp, *J. Appl. Mech.*, 1967, **34**, 153–159.

[262] A. Lytra, V. Sboros, A. Giannakopoulos and N. Pelekasis, *Soft Matter*, 2020, **16**, 4661–4681.

[263] J. Eid, H. Greige-Gerges, L. Monticelli and A. Jraij, *Chem. Phys. Lipids*, 2021, **234**, 105011.

Eidesstattliche Erklärung

Hiermit erkläre ich, dass ich die vorliegende Promotionsarbeit selbstständig verfasst habe. Sollte ich innerhalb dieser Arbeit den Wortlaut, die Abbildungen oder den Inhalt eines anderen Werkes benutzt haben, wurden diese Stellen unter Angabe der Quellen von mir kenntlich gemacht. Des Weiteren versichere ich, dass diese Arbeit an keiner anderen Hochschule eingereicht worden ist.

Potsdam, 22. März 2022 _____

Ulrike Doering